Characterization of black corrosion in reinforced concrete structures: analyses of field samples from southern Sweden

Jenny Halling

Dissertations in Geology at Lund University,
Master's thesis, no 554
(45 hp/ECTS credits)

Department of Geology
Lund University
2019

Characterization of black corrosion in reinforced concrete structures: analyses of field samples from southern Sweden

Master's thesis
Jenny Halling

Department of Geology
Lund University
2019

Preface

This master thesis is written in collaboration with the Department of Geology at Lund University and Research Institutes of Sweden – the Concrete Institute (RISE CBI), as a project to increase the knowledge in the field of study. This work states the end of two educational years of master's program in bedrock geology. This course of 45 ECTS credits is given at the Department of Geology as part of the Faculty of Natural Sciences at Lund University, Sweden.

Nomenclature

Abbreviations

BI	Beam intensity
BSE	Backscatter electron image
CBI	Swedish cement and concrete research institute (Cement- och betonginstitutet)
CTV	Chloride threshold value:
EDS	Energy-dispersive spectroscopy
GR	Green rust
GPR	Ground penetrating radar
MIC	Microbial influenced corrosion
RISE	Research Institutes of Sweden
RPM	Rounds per minute
SD	Single domain
SEM	Scanning electron microscopy
SKB	Swedish nuclear management (Svensk Kärnbränslehantering AB)
XRD	X-ray powder diffraction

Terminology

Acoustic inspections	A method for controlling the stiffness of a concrete wall. By hammering the wall a boom sound can emerge, which can give clues about potential cavities in the concrete.
Binding capacity	The ability of the material to bind ions when the ion concentration is changed.
Boom sounds	The sound of resonance in the concrete when it contains air pockets or has a loose concrete cover.
Capillary suction	Occurs in dried or partly dried concrete when water is infiltrated in pore system through the surface tension and capillary forces. This is a common mechanisms in tidal or splash zones.
Critical chloride level	The total chloride content relative to the weight of the cement that is required for de passivation of the steel.
Dielectric constant	The ratio of permittivity of a material (e.g. Portland cement) in relation to permittivity of vacuum. This can also be described as the relationship between a materials' and vacuums' carrying capacities of electric current.
Epitaxial growth	Refers to one crystalline phase that grows upon another. Epitaxy is the deposition of a crystalline overlay on a crystalline substrate.
Iron bar	Reinforcement bar.
Liesegang patterns	Rings, bands or spheres that develops under specific physical-chemical conditions in natural and artificial disequilibrium systems. This likely occurs through spontaneous periodic precipitation, generally diffusion controlled, of soluble phases in a saturated porous media (e.g. cement and sandstones).
Migration transport	In concrete this refers to the transport of ions operating under an electrical field.
Portland cement	The most common type of cement used in building materials today.
Pozzolan	An additive material to mainly Portland cement. It can have a broad range of composite ions, both naturally occurring and artificial. These are commonly siliceous and/or aluminous products of volcanic origin. Today a large quantity is industrial by-products such as fly ash and silica fume.
Rebar	Reinforcement bar.
w/c ratio	The proportion of weight of water and weight of cement in a concrete mixture.

Table of Contents

Cover Picture: Drill core (Sample 4) with a corroded reinforcement bar and rust stains that are penetrating the concrete. Black rus is seen around the reindorcement and in the margin of the rust stains. *Photo:* Fredrich, B.

Characterization of black corrosion in reinforced concrete structures: analyses of field samples from southern Sweden

JENNY HALLING

Halling, J., 2019: Characterization of black corrosion in reinforced concrete structures: analyses of field samples from southern Sweden. *Dissertations in Geology at Lund University*, No. 554, 73 pp. 45 hp (45 ECTS credits).

Abstract: In this study, the phenomenon of black corrosion is characterized by both literature studies on corrosion processes and corrosion products, and by analyzing field samples from saline subaqueous concrete structures in southern Sweden. Anaerobic corrosion of reinforcement in water-saturated concrete is an extensive but yet relatively unnoticed problem. This phenomenon can lead to serious damages that, if undetected, weaken the load-bearing capacity of the concrete structure. Black rust has been correlated with the anaerobic corrosion process and is one of the corrosion products formed during this process. When studying the concrete samples, mainly red rust was found in the superficial layer (i.e. millimeters in depth) as a result of the increased oxygen supply. Black rust was more frequently observed with increasing depth in the concrete. The black rust is usually distributed in cracks and cavities and tends to show an internal cyclic pattern with alternating ferrous and ferric iron. Both black rust and potentially a chloride variety of green rust ($GR(Cl^-)$) have been observed in connection with the reinforcement bar. The field samples that have been examined using polarized optical microscopy and scanning electron microscopy (SEM) do also show signs of degradation of the surrounding cement paste. Leaching of cementitious elements (Ca, Al and Si) is a recurring phenomenon in the concrete cover, around the reinforcing iron, and around cavities where corrosion products have been detected. Ettringite, portlandite and gypsum, were observed in cracks and cavities in the concrete and have probably formed as a result of the leaching. Precipitations of corrosion products, called nodules, on the concrete walls indicate an outward transport of the dissolved iron ions that diffuse into the pore water of the concrete. These deposits mainly constitutes of black rust products with an outer crust of red rust which act as a protective casing for the inner layers of corrosion products. This, in turn, favors the anaerobic corrosion process which can continue until the reinforcing iron is completely eroded.

Keywords: Black rust, anaerobic corrosion, reinforced concrete, corrosion products, green rust, microbial corrosion.

Supervisor(s): Charlotte Möller (LU), Birgit Fredrich (RISE CBI), and Jan Erik Lindqvist (RISE CBI).

Subject: Bedrock Geology

Jenny Halling, Department of Geology, Lund University, Sölvegatan 12, SE-223 62 Lund, Sweden. E-mail: jenny.halling@gmail.com

Karaktärisering av anaerob korrosion och svartrost i armerade betongkonstruktioner: analyser av fältprover från södra Sverige

JENNY HALLING

Halling, J., 2019: Characterization of black corrosion in reinforced concrete structures: analyses of field samples from southern Sweden. *Examensarbeten i geologi vid Lunds universitet*, Nr. 554, 73 sid. 45 hp.

Sammanfattning: I den här studien karakteriseras fenomenet anaerob korrosion utifrån både litteraturstudier om korrosionsprocesser och korrosionsprodukter samt genom undersökning av fältprover från betongkonstruktioner i salthaltiga undervattensmiljöer i södra Sverige. Anaerob korrosion av armering i vattenmättad betong är ett omfattande men hittills relativt ouppmärksammat problem. Detta fenomen kan leda till allvarliga skador som försämrar betongkonstruktionens bärighet om dessa skador förblir oupptäckta. Svartrost har korrelerats med den anaeroba korrosionsprocessen och utgör en av de korrosionsprodukter som bildas under processen. Vid undersökning av cementproverna observerades främst rödrost som ett resultat av den ökade syretillgången, i de översta millimetrarna av täckskiktet. Svartrost var mer frekvent förekommande med ökande djup i betongproverna. De svarta korrosionsprodukterna är fördelade i sprickor och hålrum i betongen samt tenderar att visa ett internt cykliskt mönster med alternerande tvåvärt och trevärt järn. Både svartrost och potentiellt en kloridvariant av grönrost (GR(Cl^-)) har observerats i anslutning till armeringsjärnet. De fältprover som har undersökts med hjälp av polariserad optisk mikroskopering och svepelektronmikroskoperning (SEM) visar även på nedbrytning av den omgivande cementpastan. Urlakning av grundämnena Ca, Al och Si är ett tydligt återkommande fenomen i betongens täckskikt, runt armeringsjärnet och i de hålrum där korrosionsprodukter återfinns. Ettringit, portlandit och gips har observerats i sprickor och hålrum i betongen och troligtvis bildats till följd av urlakningen. Utfällningar av korrosionsprodukter, kallade noduler, på betongväggarna tyder på en utåtgående transport av de lösta järnjoner som diffunderar i betongens porvatten. Dessa utfällningar består främst av svartrost med en yttre skorpa av rödrost, vilken verkar som ett skyddande hölje för de inre skikten av korrosionsprodukter. Detta gynnar i sin tur den anaeroba korrosionsprocessen som kan fortgå tills armeringsjärnet är helt urholkat.

Nyckelord: Svartrost, anaerob korrosion, armerad betong, korrosionsprodukter, grönrost, mikrobiell korrosion.

Handledare: Charlotte Möller (LU), Birgit Fredrich (RISE CBI) och Jan Erik Lindqvist (RISE CBI).

Ämnesinriktning: Berggrundsgeologi

Jenny Halling, Geologiska institutionen, Lunds Universitet, Sölvegatan 12, 223 62 Lund, Sverige. E-post: jenny.halling@gmail.com

1 Introduction

Advancing building technologies require building materials of higher standards to meet the steadily increasing demand of growing societies. Today, concrete is one of the most commonly used building materials and it is known for creating durable constructions. However, the durability usually relies on reinforcement bars that are embedded in the concrete structure. Thus, the service lifetime of a concrete structure is often determined by the condition of its structural skeleton.

Corrosion of reinforcement bars has been an issue for decades since it is one of the most common causes of deterioration. Normally, the corrosion products around the bars are expansive and cause cracking and spalling of the concrete. This kind of damage is well documented, and clearly noticeable by visual and acoustic inspections. Furthermore, in recent years a new type of damage due to corrosion has been identified, the so called black rust. This compound is related to low oxygen environments, and primarily found in underwater structures. The damage is difficult to detect as it cannot be visually seen and due to its low acoustic response. According to previous studies (Jacobsson 2016), some investigated underwater objects had as much as 50-100 % area reduction in some parts of its reinforcement; the concrete had been softened by the corrosion products which greatly reduced the structural bearing capacity. Therefore it is important, both from a safety and economical perspective, to gain an understanding of the damaging processes behind corrosion in low oxygen environments to avoid catastrophic consequences.

1.1 Aim and objectives

This study aims to characterize the phenomenon named black corrosion within reinforced concrete, and the joint mineralogical and structural changes in adjacent concrete. It will contribute to the understanding about the corrosive nature of black rust. This aim is achieved by the following objectives:

- Literature review to gain more knowledge about the field of study.
- Description of damage in the cement paste and corrosion products, based on investigations using optical microscopy, scanning electron microscopy (SEM) and microanalysis (energy-dispersive X-ray analysis, EDS) of concrete samples.
- Contribute to a chemical description of the process “black corrosion”.

1.2 Project limitations

This project does not involve the development of field methods or field assessments. It does neither include structural assessment, such as carrying capacity or service life predictions, of the concrete structures from which the samples are taken. The samples used in this study are collected from various concrete structures in the south of Sweden and are provided by RISE CBI. Detailed information such as exact sampling location will not be provided in this work due to privacy policies.

A demarcating aspect to consider is that some of the corrosion products in the samples may be unstable. Since the material is taken out of a reduced environment, there is a risk of oxidation and a change in mineral properties.

2 Corrosion in concrete

The following chapter will introduce the reader to the corrosion process of reinforced concrete related to oxygenated environments. A historical presentation of concrete as a building material is given in section 2.1. Section 2.2 continues with a literature study of the general corrosion processes of iron embedded in concrete. Furthermore, anaerobic corrosion and microbial related corrosion is treated in sections 2.3 and 2.4 respectively.

2.1 Concrete - a manmade material

The history of concrete as a building material can be traced back to several hundred years before our modern era. Even today, people can witness some impressive concrete structures such as the Pantheon in Rome, Italy, that have been standing for almost two millennia (Burström 2007). Jackson et al. (2017) have examined remnants of ancient concrete structures that are still standing along the Italian shoreline. These marine structures have been identified to be composed of a material called Pozzolan. It is a mixture of volcanic ash, tuff, pumice, limestone and seawater (Burström 2007; Lea & Hewlett 2008; Jackson et al. 2017). The seemingly successful construction method was in some extent forgotten from the fall of the Roman Empire, to be rediscovered in the medieval times (Burström 2007). However, centuries passed before the quality of concrete began to be comparable to the Roman building material. During the mid-19th century, the innovation of the steel reinforcement allowed the concrete to be utilized in a wider range for larger constructions (Lea & Hewlett 2008).

Today, concrete is a widely used material within the construction industry. Briefly described, the heterogeneous material is made of cement paste (i.e. cement mixed with water); ballast (i.e. sand, gravel and rock aggregates); and additives (e.g. fly ash and silica fume) which add certain properties to the material. Ballast represents the largest volume fraction, between 65 and 70 %, and are bound together by the cement paste. By varying the proportions of the cement constituents, a range of concrete types can be produced (Burström 2007). The most commonly used type of cement paste is the Portland cement. The general composition of this cement type is seen in Table 2.1. It mainly consists of burned calcium carbonate (calcium silicate, Al-oxide, Fe-oxide and other oxides). Furthermore, the quality of modern cement paste is regulated by international and national standards with respect to either composition or performance-related properties (Lea & Hewlett 2008). New additives are frequently tested to serve the demanding purposes of the concrete structures, largely due to the fact that older structures sometimes show signs of deterioration earlier than predicted. The deterioration can often be explained by incorrect estimates of future structural stress during the structural planning. This led to faulty dimensioning of

materials (Ljungkrantz et al. 1997).

Concrete is very durable against compressional stress, although weaker against tensile stress. The reinforcement compensate for that weakness as the metal has greater resistance to bending forces (Gestsdóttir & Guðmundsson 2012). However, the reinforcement itself may involve a weakness in the construction if it is affected by corrosion. One of the most common reasons for end of service life of reinforced concrete structures, is corrosion propagation (i.e. ongoing corrosion). This can result in spallation of the concrete cover, or unexpected area reduction of the reinforcement bar (Tuutti 1982; Fagerlund 1992; Jackson et al. 2017). Depending on prevailing conditions in the surrounding environment, different types of corrosion can develop and damage the concrete.

2.2 General corrosion in reinforced concrete

Reinforcement in concrete is normally protected by the high content of soluble calcium, sodium and potassium oxides. In the presence of water, these oxides form highly alkaline hydroxides. The alkaline condition within the concrete (pH 12.5 - 13.5) protects the reinforcement from corroding by forming a passive layer around the steel (e.g. Tuutti 1982; Broomfield 2007). The alkalinity is also dependent on the water cement ratio (w/c ratio) within the concrete. This tells about the proportion of water and cement in the concrete. A lower w/c ratio is equivalent to a smaller amount of pore water in the pore system. This also yields an increased amount of the alkaline oxides since the cement content is higher. That can be favorable in terms of preventing corrosion (Fagerlund 1992). If the alkalinity within the concrete is altered by neutralizing chemical reactions, either caused by chloride ingress or carbonation, the passive layer decays with the rate of the reaction (Tuutti 1982). The carbonation processes and the chloride ingress are further explained in Subsections 2.2.1 and 2.2.2 respectively.

Corrosion is an electrochemical process (e.g. Broomfield 2007; Fatemi et al. 2011; Boubitsas 2015). Reactions at the concrete-steel interface takes place when differences in electrochemical potential are generated within the affected iron bars. This electric potential further generates an ionic and electronic movement (Fig. 2.1; Broomfield 2007; Alonso & Sanchez 2009). The potential differences shown by Equations (2.1) and (2.2) are the anodic and cathodic processes respectively. When the passive layer is weakened, the less alkaline pore water starts to dissolve the steel. This leads to an anodic reaction where electrons (e^-) are released. To compensate for the electrical charge created within that part of the steel, a cathodic reaction arises somewhere else at the steel surface. This reaction (Equation (2.2)) consumes electrons to form hydroxyl ions (OH^-) due to the presence of water and oxygen. The hydroxyl ions strengthen the passive layer locally around the cathode because of its high alkalinity. Hence, it will counteract the corrosion process near the cathode area. However, as long as water and oxygen is available, the corrosion of the iron bar continues and corrosion products accumulate at the anode (Broomfield 2007).

The anodic reaction (donor):

$$Fe \rightarrow Fe^{2+} + 2e^- \quad (2.1)$$

The cathodic reaction (acceptor):

$$2e^- + H_2O + \tfrac{1}{2}\,O_2 \rightarrow 2OH^- \quad (2.2)$$

Regardless of which process that initiates the corrosion (i.e. a carbonation process or chlorides), the chemical reactions proceed in the same manner and can be described by Equations (2.3-2.5) (Fagerlund 1992; Broomfield 2007). When the dissolved iron (Fe^{2+}) around the cathode reacts with the hydroxyl (OH^-) from the cathode, a ferrous hydroxide is formed (Equation (2.3)). These further react with oxygen and water to produce a ferric hydroxide (Equation (2.4)). Continuous exposure to water eventually oxidize the trivalent iron hydroxide and a hydrated ferric oxide is formed (Equation (2.5)). This corrosion product is often called red rust and is commonly formed where the oxygen supply is sufficient (Broomfield 2007).

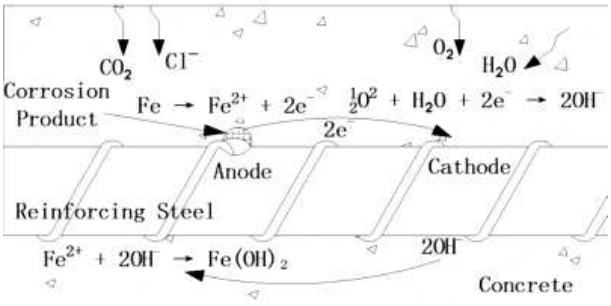

Fig. 2.1. The corrosion process generates an ionic movement where cathodic and anodic reactions operate. *Source:* Wiki Commons (2018).

Table 2.1. An example of a typical analysis of oxides in Portland cement is shown below. The oxides occur as chemical compounds called clinker minerals. The interval represent allowed composition ranges within the cement mixture. *Source*: Ljungkrantz et al. (1997).

Oxide	CaO	SiO_2	Al_2O_3	Fe_2O_3	MgO	SO_3	K_2O	Na_2O
Typical analysis %	63	20	4	2	3	3	0.1	0.3
Compositional Interval %	60-70	17-25	2-8	0-6	0-4	1-4	0.2-1.5	0.2-1.5

Normal red rust/Ferrous hydroxide:

$$Fe^{2+} + 2OH^- \rightarrow Fe(OH)_2 \quad (2.3)$$

Ferric hydroxide:

$$4Fe(OH)_2 + O_2 + 2H_2O \rightarrow 4Fe(OH)_3 \quad (2.4)$$

Hydrated ferric oxide:

$$2Fe(OH)_3 \rightarrow Fe_2O_3 \cdot H_2O + 2H_2O \quad (2.5)$$

2.2.1 Carbonation induced corrosion

Carbonation is the process that occurs when carbon dioxide (CO_2) infiltrates the concrete structure as a gas or liquid. The gas most easily diffuses through the open and air filled pore system while the small water filled pores have a restricting effect (Fig. 2.2). The movement and presence of carbon dioxide in the water filled pore system, entails a range of chemical reactions within the concrete (Equations (2.6-2.9); Tuutti 1982; Broomfield 2007; Lea & Hewlett 2008). Some of the most important factors that determine the carbonation rate are: the amount of CaO in the cement paste; the CO_2 content of surrounding matter; concrete density; relative humidity in the concrete cover; cover thickness; concrete permeability (Fagerlund 1992; Zhou et al. 2015). Penetration of carbon dioxide is often measurable in terms of distance from the concrete surface. When examining the affected concrete structures, the effect of carbonation can be noticed as a distinguishable front which often is called the carbonation front (Fagerlund 1992).

In concrete, the carbon dioxide reacts with the pore water to form carbonic acid (H_2CO_3; Equation (2.6)) as an effect due to depletion of hydroxyl ions. This process neutralizes the pH to become lower than nine (Fagerlund 1992; Broomfield 2007; Zhou et al. 2015). Another reaction between carbonic acid and dissolved calcium hydroxide ($Ca(OH)_2$), from the concrete, is shown by Equation (2.7). It produces calcium carbonate ($CaCO_3$) and water (Broomfield 2007). The solubility of calcium hydroxide is limited by the high hydroxyl concentration in the concrete pore solution. Only small amounts of the calcium are dissolved due to the presence of the more soluble alkali elements sodium (Na) and potassium (K). Carbonates incorporating sodium hydroxide (NaOH) and potassium hydroxide (KOH) increase the solubility of calcium hydroxide as carbon dioxide infiltrates the concrete. Consequently, a diffusion process arises. NaOH, KOH and $Ca(OH)_2$ diffuse towards the carbonation front while CO_2 infiltrate the concrete (Tuutti 1982).

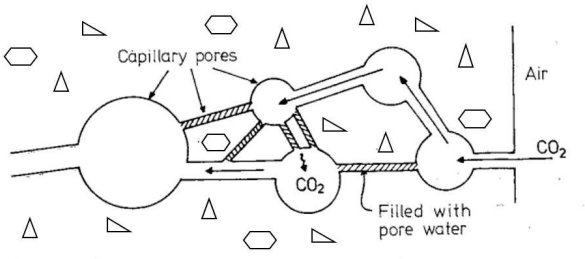

Fig. 2.2. Schematic sketch showing the diffusion of gases such as carbon dioxide through an open, and partly water filled, pore system in concrete. The carbon dioxide reacts with the water and form carbonic acid, which lowers the pH in the concrete. This initiates a carbonation process. *Source:* Tuutti (1982).

Concurrent leaching of alkali elements and depletion of hydroxyl ions results in a lowering of the pH as the concentration of hydrogen ions increases. The changing environment increase concrete porosity and hence favors further infiltration of carbon dioxide, oxygen and water. This stimulates the corrosion process to establish when the passive layer breaks down and the carbonation front reaches the embedded steel (Tuutti 1982; Fagerlund 1992; Burström 2007). Equations (2.6) and (2.7) demonstrate the process within concrete pore solution (Broomfield 2007; Lea & Hewlett 2008). However, the carbonation process proceeds as long as there is water and dissolved calcium hydroxide in the pore system (Broomfield 2007; Zhou et al. 2015). Equation (2.8) shows that the formation of the more soluble calcium hydrogen carbonate ($Ca(HCO_3)_2$ is reversible. The product will be $Ca(HCO_3)_2$ for as long as it can stay in solution and free CO_2 is available. If that is not the case, $CaCO_3$ and H_2CO_3 will precipitate instead and $Ca(HCO_3)_2$ is consumed. If the production of $Ca(HCO_3)_2$ is stabilized, it can further react with $Ca(OH)_2$, which double the production of $CaCO_3$ (Equation (2.9); Lea & Hewlett 2008).

$$CO_{2(g)} + H_2O_{(l)} \rightarrow H_2CO_3 \quad (2.6)$$

$$H_2CO_3 + Ca(OH)_2 \rightarrow CaCO_3 + 2H_2O \quad (2.7)$$

$$H_2CO_3 + CaCO_3 \leftrightarrow Ca(HCO_3)_2 \quad (2.8)$$

$$Ca(HCO_3)_2 + Ca(OH)_2 \rightarrow 2CaCO_3 + 2H_2O \quad (2.9)$$

2.2.2 Chloride induced corrosion

Corrosion initiated by chloride or similar anions (e.g. sulfide and bromide) is often related to structures exposed to seawater or deicing salts (Fagerlund 1992; Zhou et al. 2015). This type of corrosion is one of the most common causes for deterioration of structures (Angst et al. 2009). Until the 80's, it was not unusual that calcium chloride ($CaCl_2$) was used in the concrete mixture to accelerate the hardening process (Tuutti 1982; Jacobsson 2016). However, this component has been found to create a more severe corrosive environment in the concrete mixture than what is found in mixtures with normal salt of sodium chloride (NaCl; Angst et al. 2009; Zhou et al. 2015). The soluble chloride complexes are mobile within the pore water where they interact with other elements from the cement paste (Boubitsas 2015).

Chloride transport within the concrete is one of several mechanisms that control the rate and depth of penetration by chlorides. The transport of ions is principally an effect of concentration gradients in which concrete porosity and permeability play an important role. The capillary pores are controlling most of the chloride transport within the concrete by a function called capillary suction. This is a common case for dry or partly wet concretes where ions in solution easily get adsorbed. This type of transport is common in concrete structures prone to wet and dry cycles such as in tidal zones and splash zones. Regarding structures in submerged and water saturated conditions, diffusion is

the main transport function of chlorides. The ions are spread through a random motion pattern (i.e. random walk) through the pore water. Another transport mechanism is called migration transport. In contrast to diffusion, migration transport operates under the influence of an electrical field (Silva 2013). Such electrical potentials are created as a result of different diffusion rates of the ions. As a response, chlorides that pursuit electrical neutrality, interact with ions from the concrete. However this mechanism play a minor part of the chloride transport (Boubitsas 2015).

Many factors affect the chloride ingress rate and the critical chloride level. Two of the most important factors that regulate the interaction between the ions, are the chloride concentration of the surrounding environment, and the concrete composition (Ljungkrantz et al. 1997; Boubitsas 2015). The ambient environmental conditions provide the source of available chloride ions and can affect the concrete to be more or less susceptible to chloride ingress. For example, concrete in a splash zone that is subjected to wet and dry cycles has proved to be more vulnerable than concrete in the dry zone (Silva 2013; Zhou et al. 2015). In such an environment, concrete with low permeability and a suitable cover thickness is of high importance to inhibit chlorides to penetrate the concrete-steel interface (Lea & Hewlett 2008). Furthermore, the concrete composition is an important contributing factor to chloride ingress rate and penetration depth. It affects the binding capacity which in turn is influenced by other factors such as chloride concentration, hydroxyl concentration, and temperature. Freely moving chloride ions are captured by hydrated products in the concrete. It results in a lowering of the chloride ingress rate (Boubitsas 2015). That same effect has also been observed in concrete mixtures were additives have been used. Additives, like silica fume and furnace slag, increase the electrical resistivity and hence inhibit the chloride ingress rate (Zhou et al. 2015). However, despite these additives have been proven to reduce the penetration depth (Lea & Hewlett 2008), the effect varies with type and amount of substance (Alonso & Sanchez 2009).

Unlike the carbonation process, chloride ions are gradually penetrating the concrete without any defined front. Chloride ions also have the ability to penetrate the protective oxide film that surrounds the iron bars. Exposure time and chloride concentration at the steel-concrete boundary is decisive for the corrosion to occur. When the concentration of dissolved chloride ions exceeds a site specific critical value, it is known as the chloride threshold value (CTV; Fagerlund 1992; Ljungkrantz et al. 1997; Boubitsas 2015). The expression for the chloride threshold value varies within the literature. The most accurate formulations are described as follows: the percentage of total chloride content; percentage of free chloride by weight of binder in concrete; concentration ratio of chloride and hydroxyl ions $[Cl^-]/[OH^-]$ (Alonso & Sanchez 2009; Angst et al. 2009). The latter can be considered as the most constructive alternative as it concerns the status or ability of the passive layers in the concrete (Alonso & Sanchez 2009).

The corrosion is initiated when the concentration ratios of chloride and hydroxyl ions pass the critical value, as long as there is a sufficient amount of water and oxygen molecules. When the chlorides reach the embedded steel, Equations (2.10-2.13) take place at the concrete-steel interface (Zhou et al. 2015). These reactions are localized to certain areas of the steel surface where there could be some inclusion of sulfide or other impurities in the steel. Furthermore, the inhomogeneity give rise to electrochemical differences and weaknesses in the protective oxide layer. The potential differences attract the chloride ions to that area and induce a change in the ion balance (Broomfield 2007).

After the critical threshold value is reached, this generates an acid attack on the iron which goes into solution (Equation (2.1)). A pit or crevice is formed, and hence the mechanism is called pitting or crevice corrosion (Fig. 2.3; McCafferty 2010; Zhou et al. 2015). The end product can vary related to the surrounding environment. A common end product in aerated corrosive environments is ferrous hydroxide, $Fe(OH)_2$ (Equation (2.12)). This can however be further oxidized to ferric oxide trihydrate (Equation (2.13); Silva 2013).

$$Fe^{2+} + 2Cl^- \rightarrow FeCl_2 \quad (2.10)$$

$$O_2 + 2H_2O + 4e^- \rightarrow 4OH^- \quad (2.11)$$

$$Fe^{2+} + 2OH^- \rightarrow Fe(OH)_2 \quad (2.12)$$

$$2Fe(OH)_2 + \tfrac{1}{2}O_2 + H_2O \rightarrow 2Fe(OH)_3 \rightarrow Fe_2O_3 \cdot 3H_2O \quad (2.13)$$

2.3 Corrosion in anaerobic environments

Anaerobic corrosion in concrete is a rarely reported subject in literature compared with the more common aerobic corrosion of steel (King 2008; O'Donovan et al. 2013). A critical review by King (2008) presents studies of corrosion processes in anaerobic conditions, predominantly made by the nuclear waste management industry (e.g. SKB in Sweden). The aim of those studies was to test the endurance of canister storage of spent nuclear fuel in deep bedrock environments. The corrosiveness of carbon steel canisters enclosed in bentonite was evaluated; the bentonite increased in volume in contact with water and created a compact barrier around the canisters. As a result, reducing conditions where oxygen was unavailable around the canisters were created. The review shows that there was a risk that the canisters experienced anaerobic corrosion; the corrosion products varied in composition depending on prevailing conditions of the surroundings. Natural analogies to the anaerobic corrosion process have been considered to be archaeological artifacts the in studies presented in the same review. These have been exposed to anaerobic conditions over several millennia, which has resulted in black and brown colored corrosion products. The typical brown rust was found in the outer rust layers, while black rust were consistently found in the inner layers of the corrosion buildup. A similar structure of the corrosion products was found from the canister tests (King 2008).

In concrete, the anaerobic corrosion process mostly occurs when the anode in the corrosion cell is depleted in oxygen. Because of buildup of corrosion products

around the anode, the oxygen supply is restricted (Broomfield 2007; King 2008). This makes the dissolved iron stay in solution (Equation (2.1)). The cathodic reaction (Equation (2.14)) reduce the available water molecules to hydrogen and hydroxyl ions (King 2008). When the anode and cathode are separated from each other (i.e. macro cell) within the corrosion cell, the cathode is unable to provide oxygen for the anode. This creates a barrier between these two reaction sites, which can be compared to the process of pitting corrosion (Fig. 2.3) where corrosion products prevent oxygen from entering the pit (Broomfield 2007).

The general corrosion product is created by Equation (2.15). However, this may vary with composition of the pore solution in the concrete. It is possible that other products are created if the environmental conditions varies. As seen in Equation (2.16), and alternatively in Equation (2.17), $Fe(OH)_2$ is transformed to magnetite (Fe_3O_4; King 2008; O'Donovan et al. 2013).

$$H_2O + e^- \rightarrow \tfrac{1}{2}H_2 + OH^- \quad (2.14)$$

$$Fe + 2H_2O \rightarrow Fe(OH)_2 + H_2 \quad (2.15)$$

$$3Fe(OH)_2 \rightarrow Fe_3O_4 + 2H_2O + H_2 \quad (2.16)$$

$$3Fe + 4H_2O \rightarrow Fe_3O_4 + 4H_2 \quad (2.17)$$

There are some constructional relationships that have been detected that associates with anaerobic corrosion of reinforced concrete and its corrosion products. Examples of such constructional relationships are: the presence of concrete protective membranes; concrete waterproofing systems; build-up of the corrosion products; coating on the reinforcement bars; submerged concrete structures (Broomfield 2007; O'Donovan et al. 2013). The submerged concrete is the most relevant for this study because the majority of the investigated objects, in this study, originates from locations with such conditions. Another cause for the oxygen depleted conditions, similar to the examples above, is related to microbial activity and the formation of biofilms. Formation of biofilms on a steel surfaces or concrete walls can prevent oxygen transport between anode and cathode (Duan et al. 2008). More about microbial activity related to corrosion can be read in Section 2.4.

2.4 Corrosion enhanced by microbial activity

Microorganisms and geomicrobiological processes is believed to play an important role in the development of the Earth's history. Such a process is biomineralization (i.e. a process where living organisms produce minerals) of magnetite and other metallogenic minerals. This process have been proved to be more common in corrosion related environments than previously known (Miot et al. 2014). The phenomenon is often called microbial influenced corrosion (MIC). There are some groups of microorganisms that have great influence on the corrosion of steel in both terrestrial and marine environment (Usher et al. 2014). These are primarily Sulfide Reducing Bacteria (SRB; Refait et al. 2006; Rémazeilles et al. 2009; Refait et al. 2011; Usher et al. 2014; Walsh 2015), Dissimilatory Iron Reducing Bacteria (DIRB; Ona-Nguema et al. 2002a; Refait et al. 2006; Zegeye et al. 2011) and some types of Archaea (Duan et al. 2008; Usher et al. 2014). These groups are lithotrophic organisms that can obtain energy directly from minerals. By having the ability to ionize for example FeO to Fe^{2+} in an anaerobic environment, they are consuming electrons from the metal. From this aspect, microorganisms are in some cases a contributing factor for corrosion of steel in a

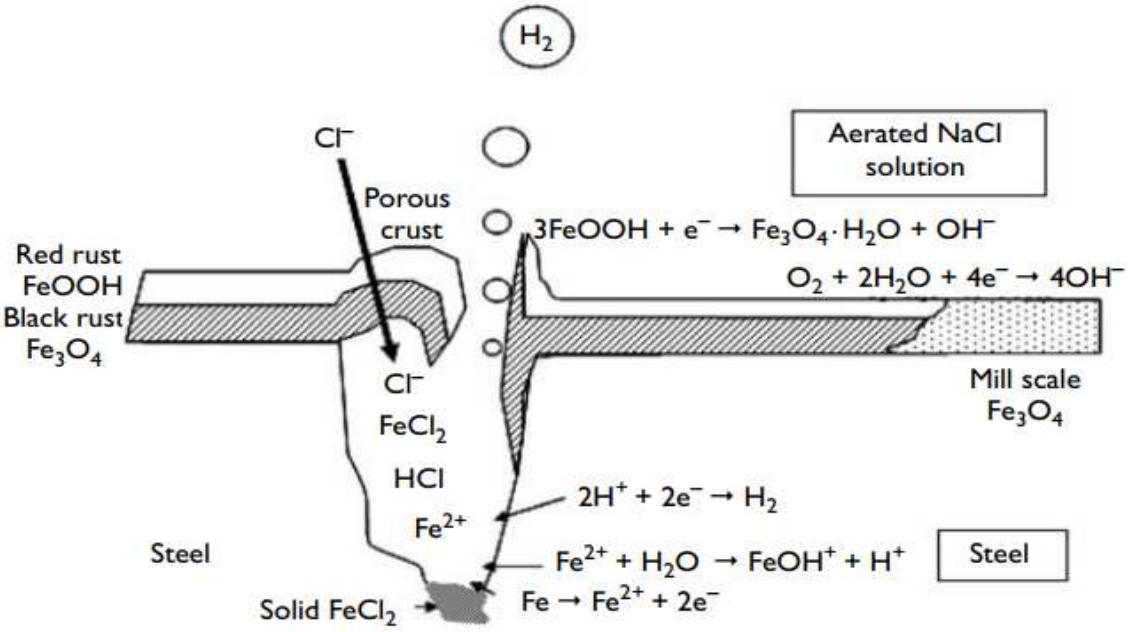

Fig. 2.3. Pit corrosion in reinforcement is often initiated by an elevated chloride concentration. Corrosion products are eventually covering the pit, in which an anoxic condition is created as oxygen is prevented from entering the pit. Black rust is seen as a corrosion layer closest to the steel. Red rust is formed in the outer layer where there is more oxygen. *Source:* Broomfield (2007).

reducing environment (Usher et al. 2014).

Experiments of steel immersed in seawater-like solutions show that microorganisms sometimes are involved in the corrosion of steel in these environments. The corrosion products are mainly magnetite and other iron oxides (Refait et al. 2006; 2011). Swietlik et al. (2012) have concluded that such corrosion also can lead to the formation of green rusts (Section 5.2). Additionally, green rusts have a certain structure that favor the colonization of SRB. This have been observed in marine corrosion processes (Refait et al. 2006).

3 Field localities and sampling environment

The field localities from which samples are taken for this study will only be briefly described in this section. These localities are three separate concrete buildings constructed by various reasons in different parts of southern Sweden. However, there are some common factors which made these structures likely sampling localities of black corrosion products: 1) their concrete is experiencing reducing conditions where the amount of available oxygen is limited, 2) the concrete is more or less water saturated most of the time which contributes to the deoxygenated environment, 3) chlorides are available in the concrete pore water from external sources. This have likely contributed to corrosion initiation, 4) all of these concrete structures have been in service for at least 40 years.

The oldest of the structures is from the 1940s. This construction contain seawater, from The Sound (Swedish Öresund), which is always in contact with the concrete walls except during inspection (i.e. when the chamber is emptied). The concrete floor was covered with a thick layer (several decimeters) of marine sediment and organic material while the walls were covered with about a centimeter thick biofilm. A second seawater related locality is a structure built between the late 1960s and the early 1970s, making this the youngest of the three localities. The concrete here is connected to the Baltic Sea which makes this to a brackish water environment. Lastly, the third locality is a water treatment plant built during the early 1960s. Unlike the other localities this construction has only been in contact with freshwater. However, this sample was extracted from a concrete wall within a flocculation basin where iron chloride ($FeCl_3$) is used as a flocculation agent. The chloride-rich environment may be one reason for the increased corrosiveness in this case.

4 Methodology

This chapter treats each step during the preparatory work (Section 4.1) and describe the analytical approach (Section 4.2) as well as processing of the analysis data (Section 4.3). Simultaneously, relevant and reliable literature was reviewed in order to gain more understanding within the field of corrosion science. The sources are mainly consisting of scientific journal articles, dissertations, books and governmental or institutional reports. Some of the books, dissertations and reports are in Swedish, the remaining literature are in English.

4.1 Preparatory work

Preparatory work covers the fundamental steps prior to the analyses optical microscopy, secondary electron microscopy (SEM) and X-ray diffraction (XRD). The field work and sampling of data are detailed in Subsection 3.1.1. A short description of the ground penetrating radar (GPR) equipment is included. The subsequent sections contain information regarding storage of the collected samples (Subsection 3.1.2), and how the samples were prepared prior to analysis (Subsections 3.1.3 – 3.1.5).

4.1.1 Field work

The first samples were taken from an underground chamber that contained sea water from The Sound. Visual and acoustic inspections of the chamber walls were performed in order to get an overview. For the acoustic inspection, the concrete structure was hit by a hammer. The fresh concrete sounds solid under the hammer, whereas deviant hollow sounds, called boom sounds, reflect damaged concrete. Where an area of interest was detected, a handheld GPR (StructureScanTM Mini XT; GSSI, Geophysical Survey Systems, Inc.) was used to get a view of the condition of the reinforcement a few decimeters within the concrete. This was accomplished by running the instrument over a predetermined grid placed over the area of interest.

The ground penetrating radar is a geophysical equipment that transmits electromagnetic energy into the material of interest. When the energy waves encounter a material with different properties, e.g. reinforcement in concrete, some of the energy is reflected to a receiver in the instrument. The time it takes is measured by the radar. The depth and travel time of the energy mostly depends upon the electrical conductivity and the dielectric constant of the material. If the electrical conductivity is high, such as in reinforcement bars and water saturated materials (e.g. wet concrete), the energy is absorbed more easily and will only travel short distances. The contrary applies to low conductivity materials, such as sand, dry concrete or wood. The dielectric constant can be used to determine the travel time of the energy. Inspection of embedded reinforcement is possible because the reinforcement appears as bright reflections. This is due to its high conductivity and high dielectric constant in contrast to that of concrete (GSSI 2017).

Photo documentation was made continuously. Samples of precipitated rust nodules were collected in plastic bags. Before the bags were sealed, most air was squeezed out by hand. Three drill cores were drilled in the sidewalls using a diamond drill that was fixed to the concrete wall by a stand and preloaded bolts. The tool was placed above nodules of rust that potentially could be corroded reinforcement bars. The collected drill cores were brought back to RISE CBI in plastic or glass containers.

4.1.2 Preservation of samples

The samples are expected to containing certain corrosion products (i.e. black rust, green rust) that are

known to be reactive and sensitive to changes in environmental conditions (Miot et al. 2014). Contact with oxygen could alter the chemical structure of these products. However, the samples are likely to contain corrosion products of red rust as well, which are more stable. Therefore, the fresh samples collected in field (i.e. drill cores and precipitated iron nodules) were kept in moisturized plastic bags with low oxygen content, and some in water filled jars. Based on the assumption that reactions proceed slower in cooler temperatures, the samples were stored in a refrigerator around 5ºC.

4.1.3 Preparation of samples for optical microscopy

Drill cores or parts of samples were sent, by CBI, to laboratories in Germany and Sweden to make thin sections. The samples were impregnated in epoxy resin with epodye (fluorescent dye), which is usually applied to concrete samples. Each thin section was estimated to a thickness of about 30 micrometers. Under cross-polarized light, quartz crystals had a yellow to orange color, which implied that the thin section was slightly thicker at some places than the standard dimension 25-30 micrometers.

4.1.4 Preparation of samples for SEM

Initially, the drill cores were cut in half parallel to their length, using a diamond coated saw blade. This gave more clarity of how the reinforcement was structured within the core. From this perspective, the core was sliced in approximately 0.5-1 cm thick slices. The slices had to be scaled down to around 9 cm^2 in order to fit the carbon coater and the SEM instrument. Water was used as coolant for the saw.

The samples have to be dry before being analyzed in the SEM. A method for rapidly drying the samples was tested on the first sample. This sample was submerged in acetone ($(CH_3)_2CO$) during 15 minutes. This was intended to drive out the water still left in the pores within the concrete, without altering the specimen. When the sample was brought up in the air the acetone evaporated. However, this test was not successful seeing that the rebar oxidized much faster with acetone. Instead the samples were dried in room temperature wrapped in tissue paper.

Some of the samples were brittle with cracks along the iron bars and had to be handled carefully not to fall apart after sawing. A thin coating of epoxy glue was applied to the surface around the sample in order to make the pieces hold together and protect the sample from oxidation. Five parts Araldite DBF (glue) and one part REN HY 956 (hardener) were carefully mixed to create the epoxy resin. The epoxy resin was then placed in an oven for about 10 minutes before it was applied. The sample had to dry in an oven, with a temperature slightly higher than room temperature (about 30ºC), for 20 to 30 minutes to evaporate excess moisture captured in pores. It took another 24 hours in the oven before the epoxy resin had hardened.

Polishing of the samples was performed at Lund University using a Struers Roto Pol-25 with rotating discs at 250 RPM. Different steps of polishing were performed with resin bonded diamond discs (MD-Piano). Initially, a grinding plate with a surface finish corresponding to SiC-Paper grit 220 was used for the ground work, thereafter plates with a corresponding finish of 500, 1200, 2000, and 4000. The sample slices were polished on the one side to be analyzed in SEM. It was important not to apply too much pressure during the polishing process to avoid breaking the samples or enhancing a possible crack-pattern initiated by the rusting process.

Lastly, a carbon coating of circa 20 nm was applied to the samples before analysis. This process was time consuming as concrete samples are more porous than most standard bedrock samples. Also, the samples were thicker and had a larger area than samples normally used when performing SEM. Thus, the vacuum pump required several hours to empty the chamber of the Auto Carbon Coater (Van Loenen instruments) as well as the sample-chamber of the SEM.

4.2 Analytical approach

Analyses of seamples were carried out by using the methodologies described below. Optical microscopy is treated in Subsection 3.2.1 and is a complementary method to SEM and XRD, described in Subsections 3.2.2 and 3.2.3 respectively. Fundamental technical descriptions of these methodologies are found in the theoretical background (Subsections 2.5.1 – 2.5.3).

4.2.1 Optical Microscopy

Overviews of the thin sections were portrayed in both plain polarized and cross polarized light with a camera (i.e. Nikon D7000), a light table, and a polarizing filter. Optical microscopy was performed using a polarized Leica microscope, and photomicrographs taken using a camera (Lecia DFC550) mounted to the same microscope. The main focus was to document the mineralogical changes of the cement paste, the mineralogical characteristics of the corrosion products, and the structural relation between the reinforcement, corrosion product, and cement paste. This was performed by using plain polarized light (ppl), crossed polarized light (xpl), darkfield reflected light illumination (DF), and polarized reflected light microscopy.

In concrete samples, it is important to note which side of the thin section that represents the outer wall of the concrete structure (i.e. the surface that has been in contact with air or water). The surface of the concrete, which has been exposed to the surrounding environment of the structure, is expected to be affected by degrading processes. The composition of the concrete was determined by describing the existing rock aggregates, their associating minerals, and the sand. The sand consists of all the finer particles found in the cement paste, and was examined in respect of textural and mineralogical maturity. Also, porosity and degree of compaction of the cement paste were inspected. These properties together with other cavities (e.g. cracks and air voids) were examined using UV-light. The higher the intensity of the fluorescent light in an area of the sample, the higher the porosity. The porosity has in some extent been altered by the carbonation process within the concrete.

Crack analysis was also performed. Cracks are always paving their paths through the weakest parts in

the concrete. Cracks along the ballast particles and plastic cracks with a non-distinctive appearance in the cement paste are formed before the hardening of the concrete. Cracks which pass through the ballast particles form after the cement curing. The cracks were measured in length, width and orientation relative to the surface. The samples were also investigated for phases (i.e. precipitated minerals) other than air within the cracks and spherical voids in the cement paste.

4.2.2 Scanning Electron Microscopy

The instrument used for scanning electron microscopy (SEM) was a Tescan Mira3 at the Department of Geology, Lund University. Analytical conditions were adjusted to 15.0 kV with high beam intensity (BI) of 20 and a working distance (WD) around 10 mm. The BSE monitor was primarily employed. Energy-dispersive spectroscopy (EDS) analyses were processed using AZtec software by Oxford Instruments.

Spot analyses were made in chosen microdomains. For each such site, approximately 20-30 spectra were positioned over a range of 5-6 rows and 4-6 columns. The function Point & ID was used to create this network, see Fig. 4.1 for an example. The starting site was chosen closest to the surface of the sample. Additional sites were analyzed with respect to distance to the corrosion-affected rebar; the color change of the cement paste was documented with increasing depth from the surface towards the iron bar. Both the cement paste close to the rebar and a few centimeters further away were analyzed for comparison purposes. Different sites of interest were chosen for monitoring of compositional changes of the cement-paste, and the magnitude of alternation was noted. Aggregate particles were avoided to a large extent during the analysis. However some had to be removed afterwards from the dataset. Additional point analyses were made of the iron bar and its surrounding corrosion products. The data from all measurements were normalized to 100% and have been obtained in wt. % element.

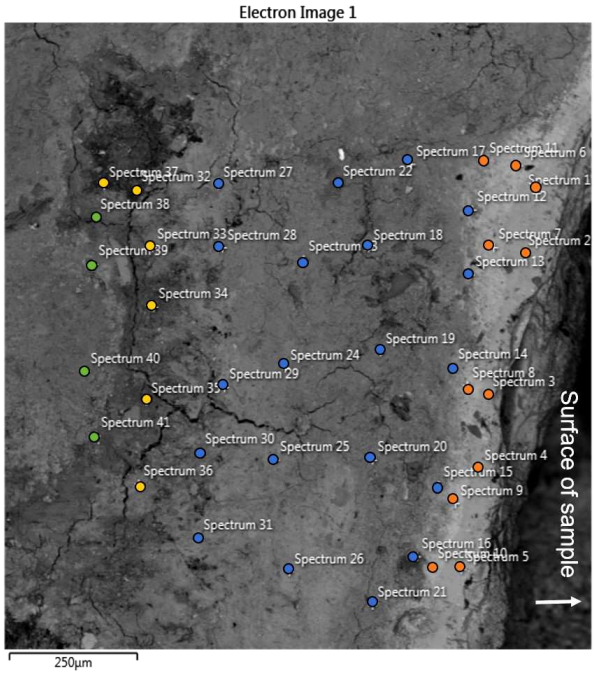

Fig. 4.1. An example of how the analysis points were placed in the BSE image. The points were marked out in relation to the direction of the surface of the sample slice. The different colors of the points represent zones of different composition.

4.3 Data Processing

Information obtained from the optical microscopy in terms of notes and microphotographs were used as base information for the analytical sessions. The microscopy gave a favorable overview of the samples which were also analyzed with SEM. Output data of the SEM analyses are treated below. Here a methodology for the data processing is presented.

The output data from the SEM/EDS had to be processed before further analyses could be made. A table from each site was exported from the Oxford software as Microsoft Excel Open XML Format Spread sheet (.xlsx) files. Also, BSE images of the investigated microdomains were saved. The values for a specific spectrum in the table spread sheet were correlated with a specific point in the BSE image. Hence it was possible to compare the elemental weight percentages between spectrums within a site, between sites, and between the different zones. The backscatter images and the spot analyses data was categorized into more generalized regions of elemental composition. An area that showed approximately the same average composition are here referred to as a zone and include two or more spectrum from the spot analysis (Fig. 4.1). The zones are mainly based on the elemental abundances of Fe, S, Cl, Ca, Al and Si for each spectrum in the analysis. The element composition was correlated with the shade around spectrum points in the BSE image. Visually, the BSE image is composed of dark and bright pixels, where dark pixels represent elements with lower atomic weight than bright pixels (Egerton 2008). The generalization was necessary since concrete is a very inhomogeneous and fine-grained material. Additionally, the mean values and standard deviations were computed within each zone. These were then plotted in graphs for visualization.

5 Literature study of green and black rust

This chapter deals with the most relevant literature related mainly to black rust. While studying the literature found on black rust, it became clear that the character of this corrosion product would be difficult to describe without understanding its origin. Green rusts have been found to play an important role in the formation of black corrosion products as well as specific microorganisms. The role of microorganisms will not be further elaborated in this study.

5.1 Black rust

Limited literature of the black corrosion process is available among research articles regarding corrosion science. Simultaneously, announcements of black corrosion products are reported from the construction sector in relation to concrete damages (Jacobsson 2016). Corroded steel bars have been examined in

combination with demolition of obsolete concrete buildings where black rust was found (Broomfield 2007; Fatemi et al. 2011; O'Donovan et al. 2013; Jacobsson 2016). Discoveries of black colored corrosion products have also been reported on archeological artefacts in sea sediment (Smart & Adams 2006; King 2008). One common factor of these scenarios is an anaerobic environment. Black corrosion products have also shown to be related to bioreduction and biomineralization (Ona-Nguema et al. 2002a; Miot et al. 2014).

The black rust is described in reports by Fatemi et al. (2011) and O'Donovan et al. (2013) as a spongy and grease-like product with black or green color. According to Broomfield (2007), Wong et al. (2010) and O'Donovan et al. (2013) the coloration of the rust is derived from the liquid produced during corrosion breakout and its contact with oxygen. Furthermore, the black product is rather unstable and transforms easily in contact with oxygen to the more common ferric oxide, the red rust variety (O'Donovan et al. 2013).

5.1.1 Chemistry and structure

The chemistry of black rust seems to be controversial in the literature. No description or characterization of black rust as a corrosion product has been encountered during this literature study. In some literature, black rust is referred to as a black precipitate or a black oxide with no defined crystal structure (O'Donovan et al. 2013; Miot et al. 2014; Usher et al. 2014). A hypothesis by O'Donovan et al. (2013) states that the black corrosion product is an oxide with both ferric and ferrous iron. It is also believed to be chemically close to magnetite. However, it is considered to be without any defined crystal structure, hence amorphous. While studying the oxidation process of green rust influenced by a bacterial culture Miot et al. (2014) identified two phases within a black precipitate during XRD analysis; single domain magnetite (Fe_3O_4) and lepidocrocite (γ-FeOOH). Further analysis with Mössbauer spectroscopy (TMS) gave a relative quantification of 90 percent non-stoichiometric magnetite (with a Fe^{2+}/Fe^{3+} ratio of 0.4) and 10 percent lepidocrocite. In the presence of limited oxygen lepidocrocite is reduced to magnetite according to Equation (5.1) (Vera et al. 2009).

$$8FeOOH_{(s)} + Fe^{2+}{}_{(aq)} + 2e^- \rightarrow 3Fe_3O_{4(s)} + 4H_2O_{(l)} \quad (5.1)$$

5.1.2 Relation to concrete

Black corrosion products have primarily been documented from reinforced concrete structures in water saturated or submerged conditions with high availability of chlorides (Fatemi et al. 2011; O'Donovan et al. 2013; Pei et al. 2017). In some cases these black corrosion products replaced the iron rebars partially or totally (Fatemi et al. 2011; O'Donovan et al. 2013). Observations from Pei et al. (2017) state that black corrosion generally follows the outline of the iron rebar, but in some cases the black rust was only formed on one side.

In many cases layered corrosion products have been observed on the steel surface. Raman spectroscopy reveals that these layers are mixtures of oxides and oxyhydroxides. The latter is generally encountered further out in the rust complex while oxides like magnetite (Fe_3O_4) and maghemite (γ-Fe_2O_3), a Fe^{2+} deficient variety of magnetite, appear closest to the iron bar (Fig. 5.1; L'Hostis et al. 2009; Duffó et al. 2012). The layered corrosion products are in many cases resembling liesegang patterns which are signs of disequilibrium. These patterns are often ring-shaped and layered structures that can develop in porous media such as concrete and mortars as well as sedimentary rocks (Rodriguez-Navarro et al. 2002).

As earlier mentioned (Section 2.3) the iron is dissolved during oxygen poor conditions (Equation (2.1)) and is transported through the open pore system in the concrete and accumulates in cavities. Sometimes the

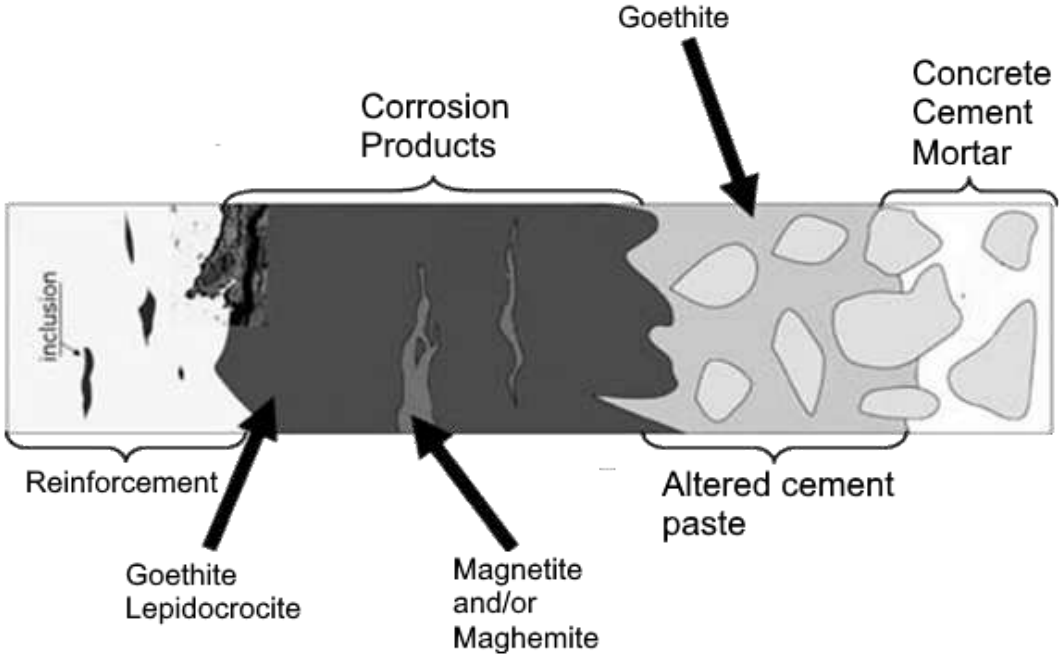

Fig. 5.1. Corrosion layers between the reinforcement and the concrete. *Source:* modified from L'Hostis et al. (2009).

iron solution is transported to the concrete surface where it reacts with oxygen. Nodule like precipitates or stains can be observed at the concrete wall where the iron solution has been able to leak out (Tuutti 1982; Fagerlund 1992; Jacobsson 2016). However, if the concrete contains damaged waterproofing membranes it is possible that the iron solution is prevented from reaching the concrete surface. Therefore, the surface could lack any signs of rust (Broomfield 2007). The nodules or rust stains may be regarded as an indication of a corrosion attack involving black rust. After exposure to oxygenated conditions the black product transforms to red rust within minutes or hours (Fatemi et al. 2011; O'Donovan et al. 2013).

Apart from red rust the black corrosion product has shown to be less expansive and hence exerts less internal stress within the surrounding material. This is partly due to the effect of its high solubility in water and the lack of a crystal structure. As a result of the characteristics described, no visual cracks will appear in the concrete cover and the corrosion process stays unnoticed (Tuutti 1982; Fagerlund 1992; Jacobsson 2016). The corrosion process can lead to internal section loss of the reinforcement which is a dangerous phenomenon if it remains unnoticed (Fatemi et al. 2011). Even if a small volume change occur during the black corrosion process, it is only up to twice the volume of the unaltered steel compared to the red rust which can expand up to ten times (Fig. 5.2; Tuutti 1982; Broomfield 2007; Fatemi et al. 2011).

5.2 Green rust

In the search for descriptions about black rust and anaerobic corrosion, literature on green rust were dominating the results. The corrosion products of green rust seem to be a well-studied subject compared to black rust. More literature is available, and the field of research appears more focused on the green rust components than black rust. In most of the green rust works, black corrosion products are mentioned, but sparsely discussed. Bernal et al. (1959) presents a structural inter-relationship between oxides and hydroxides of iron with focus on the least stable rust types (e.g. green rusts). By dehydration and oxidation, green rusts eventually transform to the oxyhydroxides goethite (α-FeOOH), akaganetite (β-FeOOH), and lepidocrocite (γ-FeOOH) or magnetite (Fe_3O_4).

5.2.1 Green rust in literature

In natural environments green rusts have been described as corrosion products of steel. These products are primarily occurring in slightly alkaline to neutral pH in aqueous medium. Commonly carbonate green rust is obtained from a carbonated medium such as carbonated concrete, while in seawater or seawater like solutions, the sulphate green rust variety is more often observed (Refait et al. 2006).

Green rusts are commonly formed by anaerobic corrosion of iron (McGill et al. 1976; Badan et al. 1991), and are possibly influenced by electrochemical and microbial activity (Refait et al. 2006; Duan et al. 2008; Refait et al. 2011). Most of the research around green rust is done from laboratory experiments such as in seawater-like solutions and corrosion cells with electrical fields (Duan et al. 2008; Miot et al. 2014). The high reactivity of green rusts with the atmosphere makes it difficult to examine the product from field-based studies in its natural environment. Such studies would require special sample treatment and well-planned surveys (Świetlik et al. 2012; Silva 2013).

5.2.2 Chemistry and structure

Green rusts (GRs) are described as Fe(II-III) hydroxy-salts with a layered build-up structure. The stacking pattern, referred to as layered double hydroxides (LDH), is representative for the crystal structure of green rusts forming ferrous hydroxide-like layers. These layers consist of positively charged Fe(II-III)-layers with negatively charged interlayers of anions (commonly Cl^-, CO_3^{2-} or SO_4^{2-} and water molecules (Génin et al. 2006; Refait et al. 2006; Świetlik et al. 2012; Yin et al. 2017). The crystal structure of green rust resembles of a "house of cards structure", where the empty spaces may be colonized by microorgan-

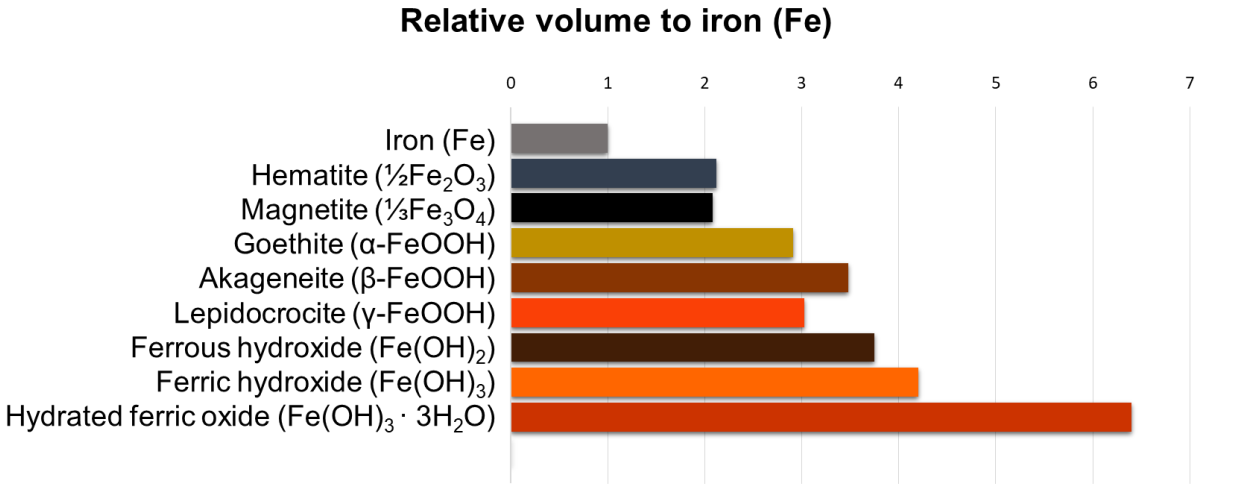

Fig. 5.2. This diagram shows the volume of different corrosion products relative to elementary iron. Hydrated ferric oxide show the largest volume increase, over three times compared to magnetite and hematite. It is mainly this volume increase that causes the concrete to crack and spall during corrosion. *Source:* modified from Broomfield (2007).

isms, particularly sulfate reducing bacteria (SRB; (Refait et al. 2011).

It is known from experiments that oxidation of green rusts result in different compositions of common rust. These are the oxyhydroxides α-, β-, γ-FeOOH (also known as goethite, akageneite, lepidocrocite) and the oxide magnetite (Fe_3O_4). Which phase will form depends on the surrounding pH value, temperature, oxygen flow, concentration of dissolved Fe(II) and general composition of the electrolyte used in the experiment. In this case a concrete-simulating electrolyte was used (Refait et al. 2006). Furthermore, the transformation from GR to magnetite usually occurs at a low redox potential where dissolved Fe(II) is released to the surroundings. On the other hand GR oxidation is complete at high redox potential, which is generating Fe(III)-oxyhydroxides instead. Still, the dissolved Fe(II) can react further (through successive reduction) and transform the ferric oxyhydroxides to magnetite (Miot et al. 2014). A similar relationship was earlier presented by Bernal et al. (1959) where they described the inter-relationships between the oxides and hydroxides of iron. Another relationship have been showed by McGill et al. (1976). Through SEM and XRD they identified epitaxial growth of magnetite on the opposite side of green rust crystals. Furthermore, Guilbaud et al. (2013) have demonstrated a more complex formation mechanism of green rusts, the so called Ostwald-ripening mechanism. This involve recurrent cycles of ions that goes into solution and then are readsorbed on the green rust crystals. Metastable green rust has also shown to be transformed into a more stable phase of iron oxide – magnetite (Zegeye et al. 2012; Guilbaud et al. 2013). In summary, it is possible to draw conclusions about the relationship between green rust hydroxides and magnetite (black oxide), mainly through oxidation and dehydration.

6 Analytical Results

In this chapter the results from the practical analyses are presented. A short description of the field localities is presented together with a description of the black rust in its natural environment. In the following sections, descriptions of the samples are presented with a selection of the compiled results and findings from the polarized optical microscope and the scanning electron microscope. Here are the most interesting microdomains generally situated close to the concrete surface and, in the adhesion zone between the reinforcement and the altered cement paste. A micro-domain a few cm away from the altered areas has been additionally measured in order to obtain a reference for the cement paste. The relationship between Al/Ca and Si/Ca describes the health state of the cement paste. A fresh cement paste has a ratio of circa 0.35 for Si/Ca and circa 0.08 for Al/Ca while typical altered cement paste values are higher, which means that the cement paste is richer in Si and Al. The Ca-content is usually decreasing during alteration due to leakage. Additionally, increased values of Fe, S, Cl and Na can be found in some data sets. These elements, especially Fe, were further compared to the Si/Ca ratio to discover possible trends in the data sets. The complete data set of the analyses can be found in the Appendix.

The analyses from the scanning electron microscope are generalized and divided into different zones as described in Section 4.3. These are characterized by the backscatter image and the chemical analyses from each microdomain to separate iron-rich parts, cement paste, corrosion product, and other areas from each other. In the tables and diagrams the same color code is used for each zone.

6.1 Description of black rust in field

The samples available for this study show signs of black rust due to an anaerobic corrosion process in the concrete constructions examined. These are three water-related or submerged constructions where the concrete is water saturated most of the time, and more or less subjected to chloride rich environment. One drill core (Sample 3) is taken form a water treatment plant with freshwater environment. However, this core was extracted from the flocculation basin where iron chloride ($FeCl_3$) was used as a flocculation agent. The concrete walls in this construction are from the early 1960s. Therefore, it cannot be ruled out that other types of flocculants (e.g. sulfate-based) also have been used during the past decades. The other drill cores are from environments with saline brackish water related to The Sound (Swedish Öresund; Samples 1 and 2) and the Baltic Sea (Sample 4). The core sampled in connection to the Baltic Sea is from a construction built between the late 1960s to the early 1970s. The concrete building connected to The Sound is the oldest of the three localities and is from the 1940s.

Black rust in reinforced concrete structures is difficult to discover by visual methods since its occurrence is often hidden within the concrete. The only outer signs during an inspection are potential rust nodules which precipitated on the concrete surface, see Fig. 6.1. Usually, the precipitates have been observed at the concrete surface wall as a gritty spongy product, porous enough to cut it with a knife. The outer parts are often red or orange to yellow from oxidized corrosion products while the interior is black.

Black rust is observed as a porous and fragile substance in both field localities and collected concrete samples. The black substance is found close to the reinforcement either directly connected to the steel or in adjacent cavities. Where the black rust has replaced the iron, the texture is completely changed from a solid metal to a dark muddy soft material (Fig. 6.2). This product has low resistance to abrasion and is easy to break. When the material is exposed to an aeriated environment (the atmosphere) the color change from dark/black to red. The red rust color is dominating the concrete wall, even though it can have a black core/interior. Some of the nodules collected for this study had a hard, black crust and a porous and sometimes layered interior where black and red rust were alternating. Nodules seen in the field localities and on core samples were porous and fragile. The porous parts of the nodules were mostly red rust colored but could contain black layers. Yellow rust stains were observed at the concrete walls around the black rust. In Fig. 6.3 the nodules have been scraped off the wall which expose the black rust surrounded by red and yellow corrosion products. The rust nodules were sit-

Fig. 6.1. Rust nodules covered with mainly red rust at a concrete wall in the field locality of The Sound. Generally these had a diameter of three to five centimeters. These are slightly covered by the surrounding biofilm.

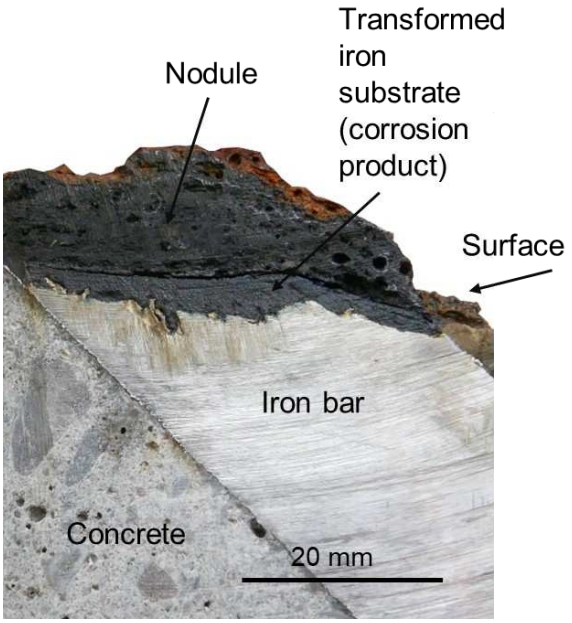

Fig. 6.2. A cross section from one of the samples from The Sound. The reinforcement is corroded in the upper part and is covered by a rust nodule. The sharp line between the nodule and corrosion product indicate to where the previous rebar reached.

ting on the concrete wall and created a pronounced topography which made them relatively easy to discover. Damage to the concrete itself was observed behind the nodule, where the cement paste had become softened and porous.

6.2 Description of samples

Descriptions of the samples examined is presented below. First a general description of the hand specimen (i.e. the drill cores) is presented, followed by a more detailed petrographic description of a thin section or a slice of the core sample. Characteristics of the corrosion related damages in the concrete as well as the reinforcement is described in the paragraph "Deterioration of cement paste and reinforcement". The specific black rust characteristics that is found within the samples is described in "Black rust characteristics". The result from the SEM analyses are elucidated in the "SEM analysis" paragraph for each sample piece that were analyzed with this method. A selection of representative microdomains are presented here, the others are listed in the Appendix.

6.2.1 Sample 1

General description of hand specimen: The hand specimen of Sample 1 (Fig. 6.4) is a piece of a concrete core, drilled out from a culvert in a seawater chamber connected to The Sound. When looking at the cross section of the core a reinforcement bar is crossing the right corner. On top of the sample, a nodule of black and red corrosion products is covering the reinforcement. In the thin section, small sand particles are visible within the nodule. The upper most part of the reinforcement, up to 5 mm, has been affected by the corrosion process and has left a dark soft muddy substance – black rust.

Thin section 1 (TS 1)

Petrographic description: The grain size is not fairly represented by the thin section (Fig. 6.5), only the finer grain fractions are visible (up to 5 mm). Larger rock aggregates (5-30 mm) are seen in the hand specimen. These have an angular to sub-angular shape and a granitic composition. The sand fraction has a grain size of circa 0.1-2 mm. Sand grains have a moderate texturally and mineralogical matureness. Sub-angular to subrounded grains mostly comprised of polycrystalline and cryptocrystalline quartz and altered feldspars (Fig. 6.6). Sand particles are also observed within the nodule. The sand grains have a denser distribution close to

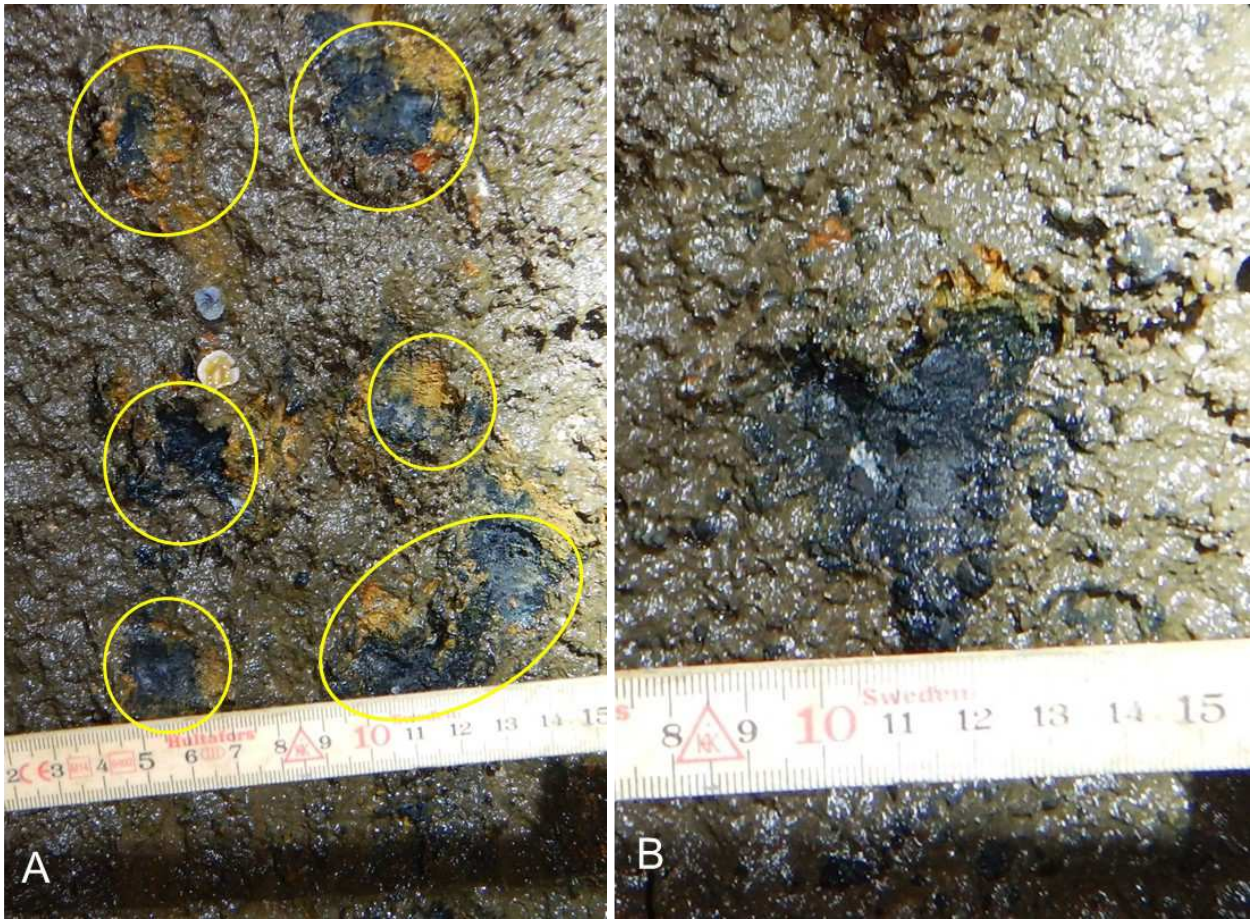

Fig. 6.3. The black spots on the concrete wall shows the interior of the nodules, which have been removed. The areas of these spots can be represented by the section area of the corroded rebar. This is how black rust looks like behind the layer of red rust. The surrounding brown/grey material is the biofilm covering the concrete wall. **A.** Several black spots within a relatively small area. **B.** A closer view of the black interior of a nodule.

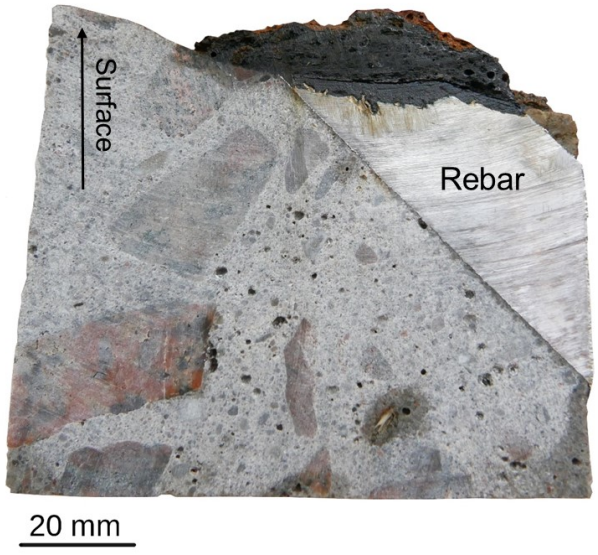

Fig. 6.4. The cross section of the drill core of Sample 1.

the rebar (Fig. 6.7) but thins out towards the surface (Fig. 6.8). The nodule covers the surface to a depth of 15 mm in the sample. Pores are evenly distributed in the concrete and are about the same size beneath the reinforcement. Some of the voids seem to be caused by the preparation process. The air voids in the discolored nodule are of an elongated horizontal shape seen in TS 1.

Deterioration of cement paste and reinforcement: The nodule is mostly comprised of corrosion products that initially were black in color but turned to red after a few hours. Deterioration of the reinforcement is also visible especially through the darkfield reflected illumination microscopy (Figs. 6.9 and 6.10). The reinforcement is totally degraded in the uppermost 5 mm, where black corrosion products have formed. In the microphotograph of Fig. 6.9 a pit has formed in the iron surface. Beneath the reinforcement the cement paste is unaltered except for the area within a cm from the rebar where signs of carbonation can be seen (Fig. 6.10). The lower concrete-rebar boundary in Fig. 6.10 is less affected by the degrading processes compared to the upper boundary seen in Fig. 6.7. This thin section is also showing different sets of cracks. An example is clearly seen in Fig. 6.9 where the corrosion products are offset related to the pit. An empty crack runs parallel to a wider epoxy resin filled crack.

Black rust characteristics: In this sample the corrosion products are concentrated above the reinforcement bar. The reinforcement lost its adhesion with the surrounding cement paste in the upper 3-5 mm and constitutes

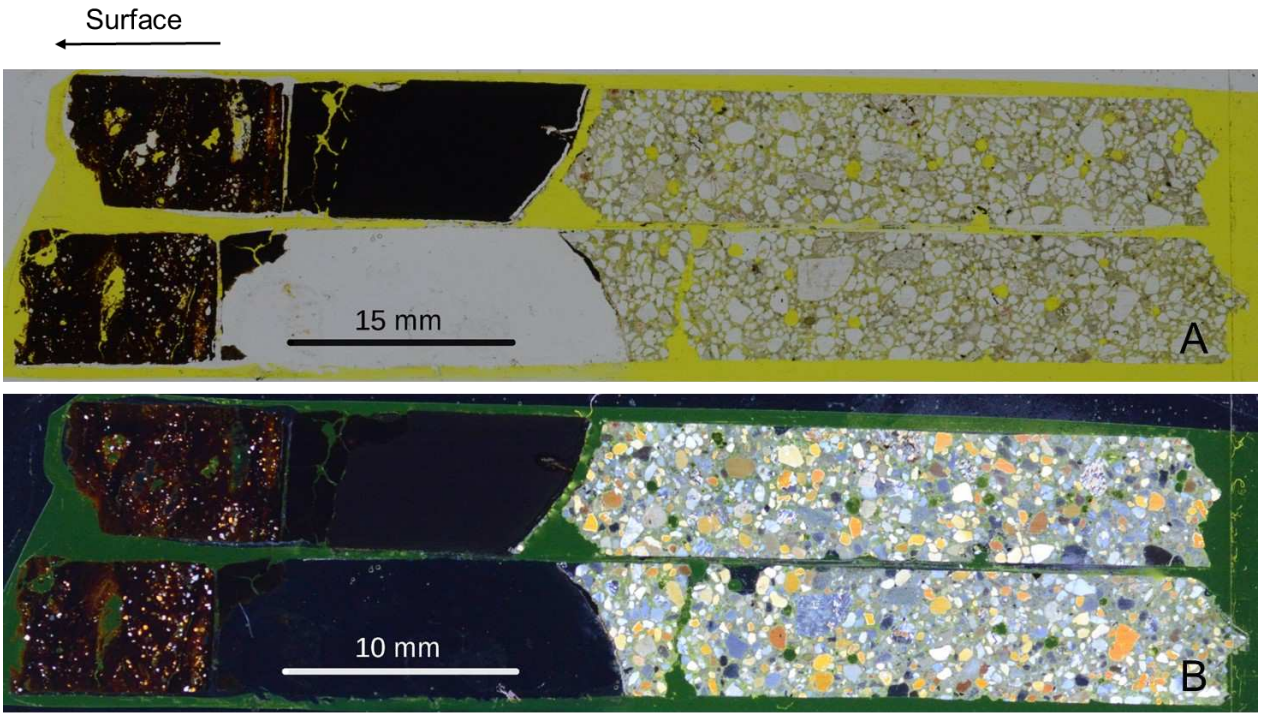

Fig. 6.5. An overview of Thin section 1, in both **A.** normal and **B.** polarized light. The left edge is the surface of the sample.

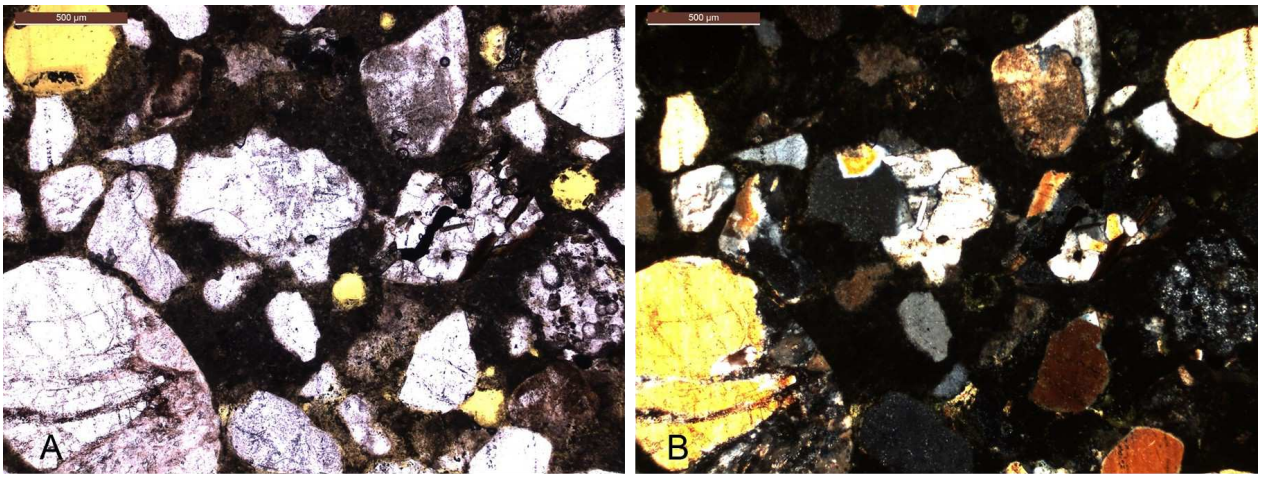

Fig. 6.6. Photomicrograph of the cement paste in Thin section 1. The concrete contains sub-angular to sub-rounded grains, mostly comprised of polycrystalline and cryptocrystalline quartz and altered feldspars. The scale bar in the upper left corner is 500 µm. **A.** Plain polarized light. **B.** Crossed polarized light.

now of a dark soft and porous material with a mud-like texture. Within the nodule, bands of black rust products are observed between the oxidized red rust layers. This is well illustrated by the dark field microphotographs in Figs. 6.7 and 6.8. The black rust is most clearly visible from the darkfield photomicrographs where it is discerned with the black to dark blue color and metallic luster. The red rust is exhibiting a rusty brown to moss-green color with the darkfield method.

SEM analysis of Slice 1.1

The cement paste at the surface is completely altered by chemistry. Only the concrete texture is still left with ballast particles in the fine-grained mass (Fig. 6.11). The cement paste building elements Ca, Si, Al are leached out, and are close to the detection limit in the EDS analysis. Most of the weight percent in the analysis is distributed on Fe, O and S, which speaks for a completely transformed cement paste in that microdomain. It is also clear with the scattered cement paste ratios of Si/Ca and Al/Ca shown in Fig. 6.12. Deeper within the sample the cement paste shows rather normal values, resembling an unaltered cement paste (Figs. 6.13 and 6.14). However the cement paste - rebar boundary is rather sharp and show little signs of alteration in the microdomain of Site 7 (Fig. 6.15).

Areas that appear like dark grey spots and form topographic patches or traces on the reinforcement are observed in several microdomains, among Sites 7, 10 and 12. The same pattern is also seen in other microdomins in the examined sample (e.g. Slice 1.2, Site 8). These corrosion products seem to have formed after

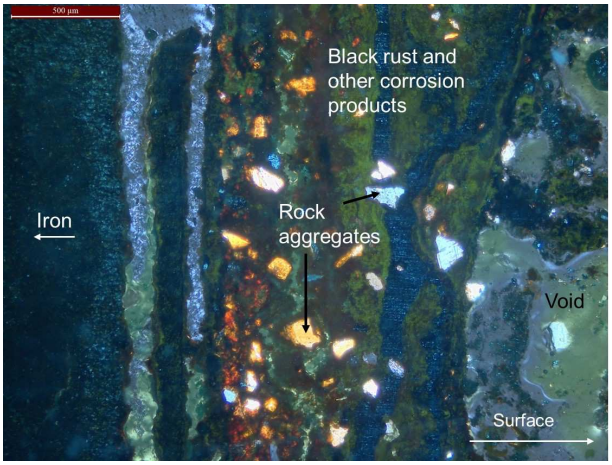

Fig. 6.7. This photomicrograph is taken in xpl with the darkfield mode enabled. A part of the corroded reinforcement (iron) is visible on the left side. The surface direction of this photo is to the right edge. Different corrosion products are displayed in the central which is interpreted as the transformed cement paste. *In situ* rock aggregates are the only product left of the concrete material. The scale bar in the upper left corner is 500 µm.

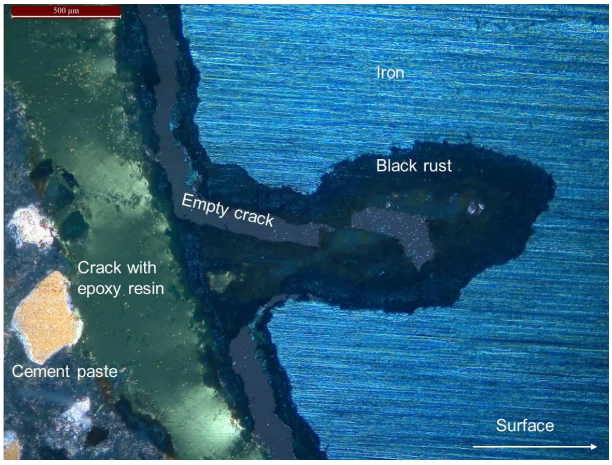

Fig. 6.9. A pit in the back of the reinforcement bar (iron) seen from the surface side (arrow). The pit is filled with corrosion products interpreted as black rust. An empty adhesion crack has recently formed in the corrosion products between the iron bar and the epoxy resin. This photomicrograph is taken in xpl with the darkfield mode enabled. The scale bar in the upper left corner is 500 µm.

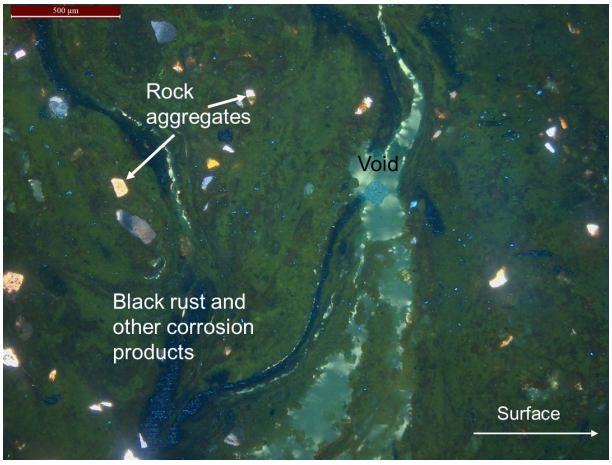

Fig. 6.8. Photomicrograph is taken in xpl with the darkfield mode enabled. This microdomain is situated a few millimeters further towards the surface (arrow pointing the right direction) of this sample, compared to Fig. 6.7. Black rust is seen in thinner bands within another corrosion product. *In situ* rock aggregates are left from the concrete material. The scale bar in the upper left corner is 500 µm.

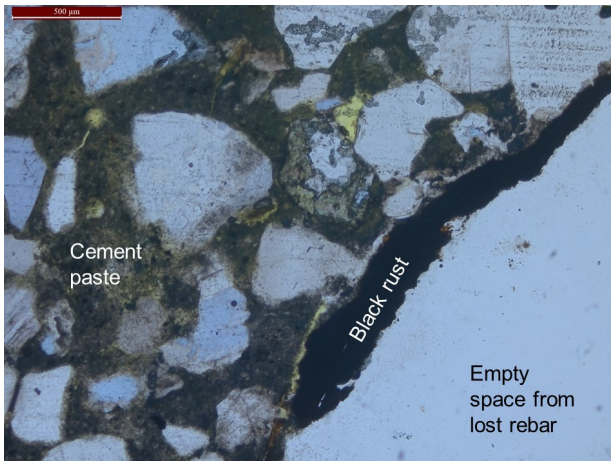

Fig. 6.10. The lower adhesion zone have small amounts of corrosion products compared to the upper rebar-concrete boundary. The line here is rather sharp without complete transformation of the cement paste. The piece of the reinforcement in this part of the thin section has vanished. The photomicrograph is in ppl and the scale bar in the upper left corner is 500 µm.

the preparation of the sample since they occur on the polished iron surface. The dark areas at the reinforcement show elevated values of chloride (Cl). Slightly over 22 wt. % has been detected in some spots, see Table A8. The microdomain of Site 10 contains mostly iron and chloride in the topographic areas (Zone 2) which may indicate the presence of Fe(II)-(III) hydroxy-chloride, green rust (GR(Cl^-)) as described in Subsection 5.2.2. These corrosion products are layered and do also show crack pattern that seem related to dehydration (Fig. 6.16).

A comparison of Si/Ca - Al/Ca ratio between microdomains from the surface to the middle of the sample show that the condition of the cement paste is varying a lot. The near surface cement paste in this slice show more deterioration compared to the deeper cement. Fig. 6.17 show that the cement paste ratio distribution is more scattered in the near surface zones (Site 1) compared to the deeper zones, for example Site 7 and the cement paste in Site 9.

Looking at specific elements compared with the Si/Ca ratio in the cement paste, different sites can reveal trends in the corrosion process and deterioration of the cement paste. Chlorides for example, are more commonly detected deeper within the sample compared to the surface areas (Fig. 6.18A) and the sulfur elements are more represented in the surface cement (Fig. 6.18B). The iron distribution is represented in the near surface cement and at the rebar site showing where the corrosion products are situated (Fig. 6.18C).

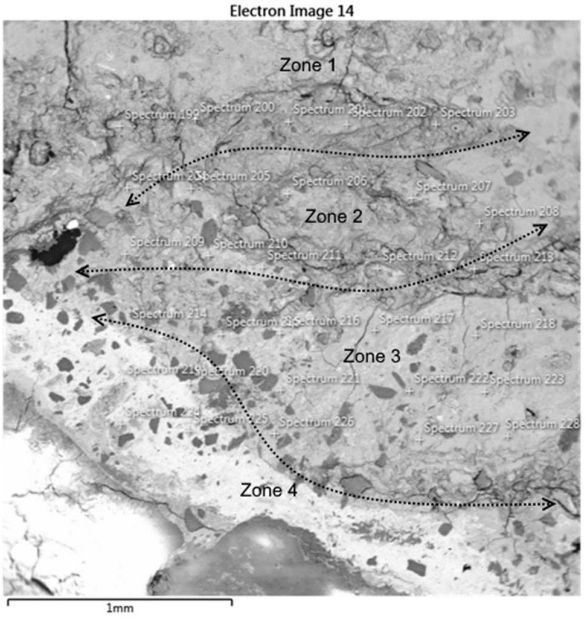

Fig. 6.11. BSE image of Slice 1.1 from Sample 1. The dotted lines is illustrating the division between the different zones based on the point analyses. The lighter area (Zone 4) is richer in iron compared to Zones 1, 2, and 3.

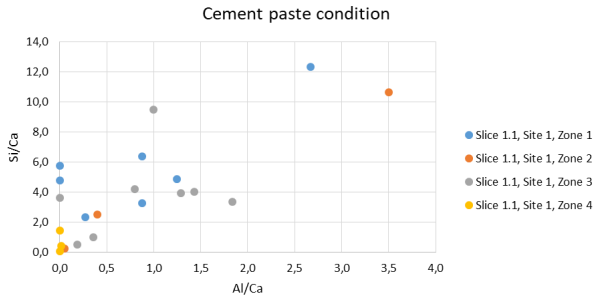

Fig. 6.12. The cement paste condition is determined by the Si/Ca and Al/Ca ratios in the cement paste. The values in this graph show that Site 1 in Slice 1.1 has an altered cement paste where the cement building elements are reduced. These values are exceeding normal Si/Ca and Al/Ca ratios (0.35 and 0.08 respectively) by several times.

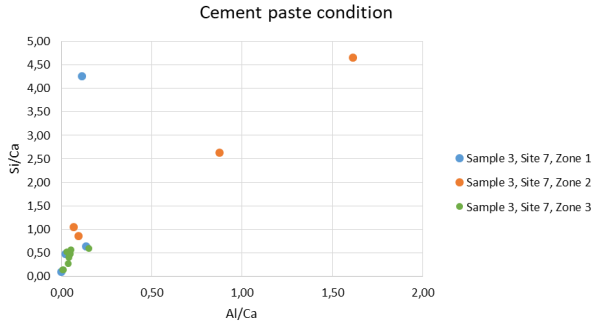

Fig. 6.13. Cement paste that of Site 7 (Zone 3, green dots) show minor alteration even if it is closely situated to the corroding iron.

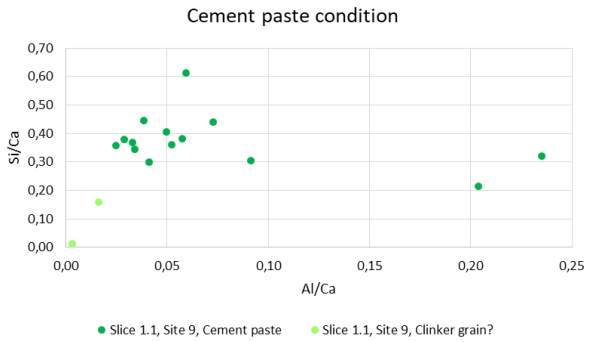

Fig. 6.14. The cement paste in Site 9 is rather unaltered. This microdomain is situated a few millimeters further away from the reinforcement.

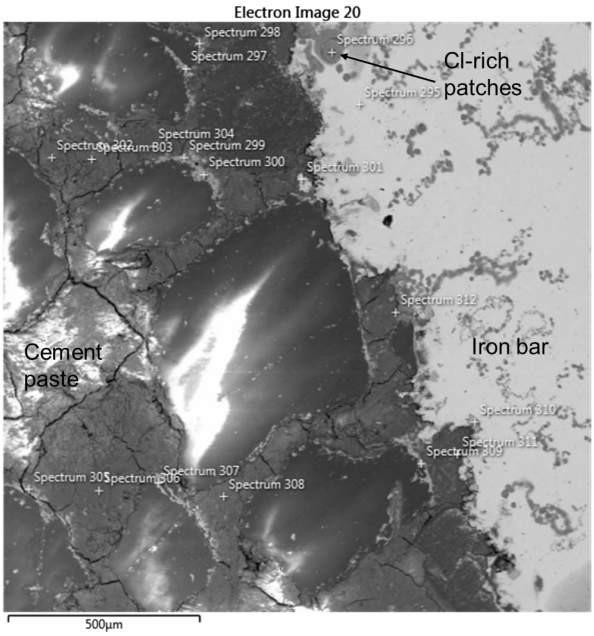

Fig. 6.15. The adhesion zone in this microdomain (Site 7) is rather sharp and show little signs of alteration in the cement paste. Corrosion is acting on the reinforcement leaving dark grey chloride-rich traces on the iron.

SEM analysis of Slice 1.2

Petrographic description: From Sample 1, a second piece of the core (Slice 1.2) was analyzed in the scanning electron microscope. Also, in this piece of the sample, the grain size distribution is uneven. From the cross section in Fig. 6.4 it is seen that larger ballast particles are found on the left side in the picture, while smaller ballast particles are situated closer to the reinforcement. The ballast particles have an angular to sub-angular shape and a granitic composition. The sand fraction has a grain size of ca 0.1-2 mm. Sand grains have a moderate texturally and mineralogical matureness. Sub-angular to sub-rounded grains are mostly comprised of polycrystalline and cryptocrystalline quartz and altered feldspar. The nodule covers the surface to a depth of 15 mm in the sample. The nodule has a horizontally layered texture defined by elongated pores and black corrosion products. In the cement

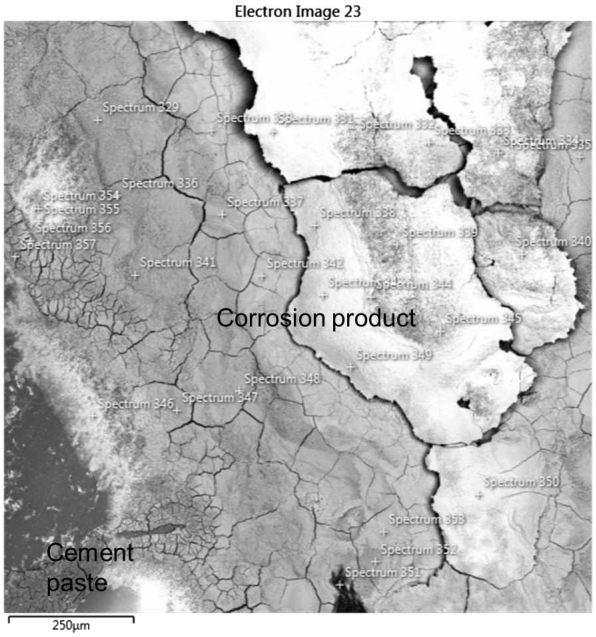

Fig. 6.16. Site 10 in Slice 1.1 has flakey and chloride rich corrosion products that is sitting on the rebar.

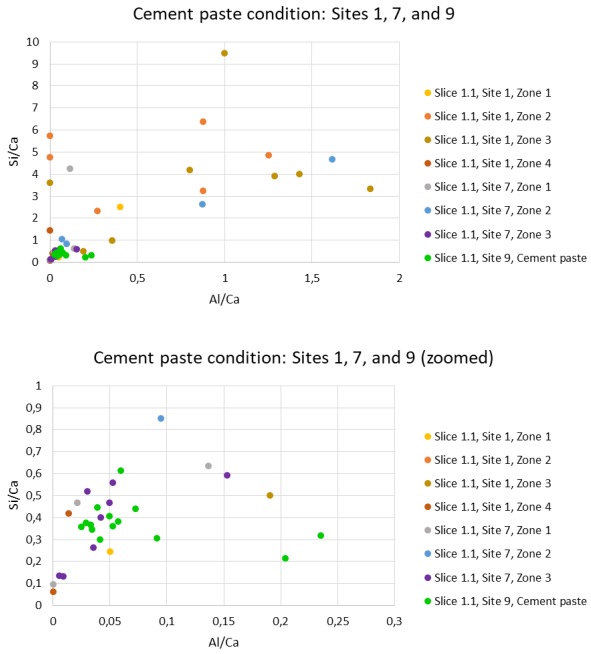

Fig. 6.17. Cement paste ratio (Si/Ca vs. Al/Ca) distribution in the near surface zones (Site 1) compared to the deeper zones, for example Site 7 (Zone 3) and the cement paste in Site 9. The scattered ratios in the upper zones indicates a changed chemical composition. Different scales are shown on the axes of the upper and lower graph.

paste pores are rounded and evenly distributed and are about the same size.

Deterioration of cement paste and reinforcement: The EDS analysis show that the surface cement paste has an altered composition compared to fresh cement paste. An overall comparison of the cement paste in

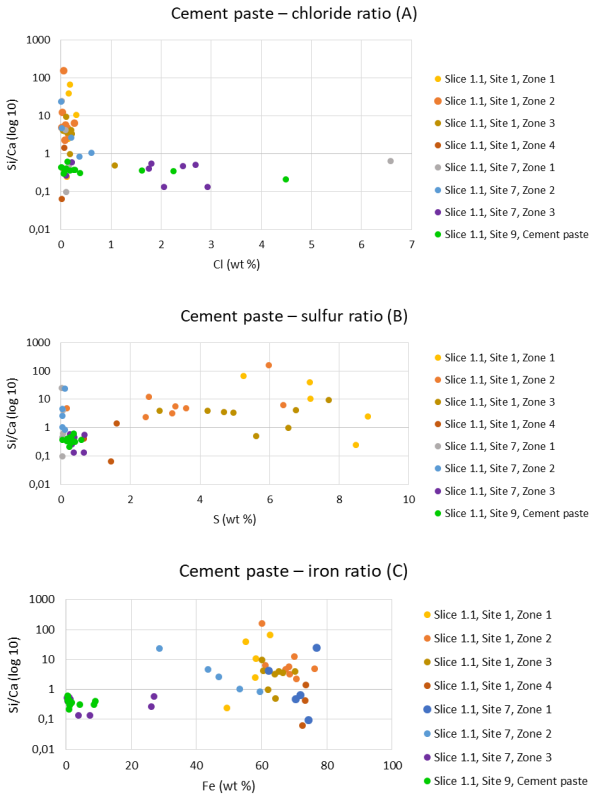

Fig. 6.18. Cement paste ratio (Si/Ca) in Slice 1.1 compared to abundant elements (wt. %) from the EDS analysis. **A.** Si/Ca vs. Chloride in shallower (Site 1, Zones 1-4) compared to deeper parts (Site 7, Zones 1-3, and site 9). **B.** Si/Ca vs. Sulfur in shallower (Site 1, Zones 1-4) compared to deeper parts (Site 7, Zones 1-3, and site 9). **C.** Si/Ca vs. Iron in shallower (Site 1, Zones 1-4) compared to deeper parts (Site 7, Zones 1 -3, and site 9).

variable depths from the surface concrete show differentiated Si/Ca – Al/Ca ratios. It is visualized in Fig. 6.19A, where the shallower zones of Site 3 show offset ratios compared to the deeper Sites (number 8 and 13) in the unaltered cement paste. Deterioration of the cement minerals are further seen in the misplaced Si/Ca – Al/Ca values of Site 3 (Fig. 6.19B). A very high sulfur content is also registered in the less iron rich parts. This trend is seen especially where the cement paste looks more porous and cracked (e.g. in Site 3, Zone 4; Fig. 6.20A-B and Fig. A15). The iron content is also very high in the altered cement paste material close to the surface. Corrosion products with a high weight percentage of iron and sulfur have replaced the cement elements in the concrete. This is illustrated by the backscatter image of Site 6 (Fig. 6.21A) where ballast particles are left as relict or *in situ* structures in the altered cement paste. The elemental maps of this microdomain (Fig. 6.21B) illustrate the elemental distribution of iron, calcium, magnesium, sulfur, chloride and sodium. Sulfur is enriched in the cracked part, while iron is more prevalent in the center area.

Thin empty cracks are observed in most of the microdomains in this sample slice, both within cement paste and corrosion products. The crack pattern is characteristic for dehydration cracks. The reinforce-

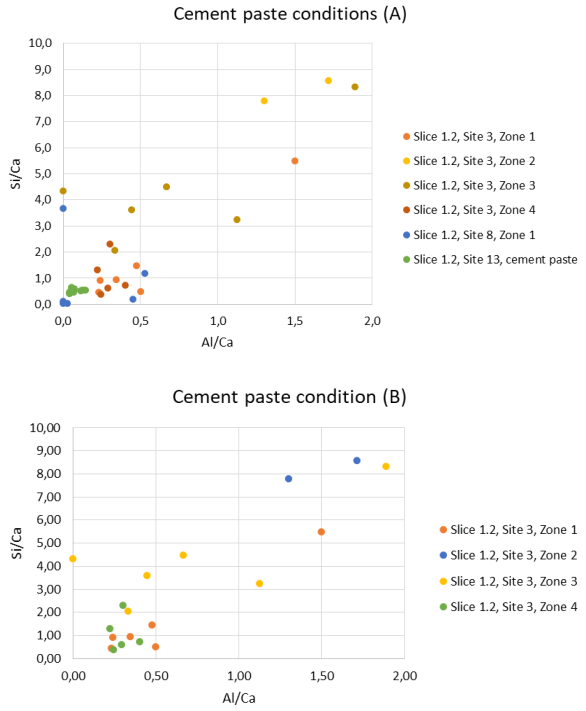

Fig. 6.19. **A.** Cement paste condition of shallower (Site 3) and deeper (Site 8 and 13) sites of slice 1.2 is shown in this graph. **B.** A closer view of the conditions of site 3.

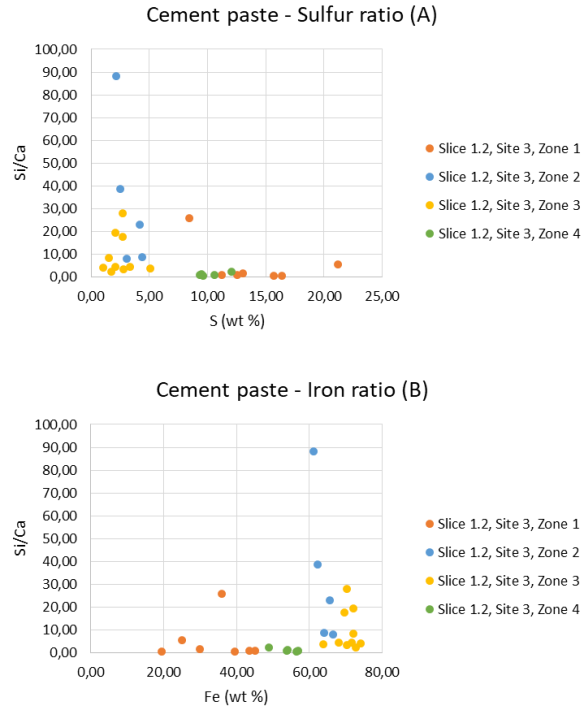

Fig. 6.20. Site 3 in Slice 1.2 is showing elevated amounts of sulfur and iron within the cement paste. **A.** Zones 1 and 4 show higher sulfur content compared to Zones 2 and 3. More cracks and a darker shade of the BSE image is seen in the sulfur rich zones. **B.** Zones 2-3 are richer in iron which express a lighter shade in the BSE image. The BSE image is found in the Appendix (Fig. A15).

ment is surrounded by chloride rich corrosion products which looks like altered cement paste. Even more chloride rich mounds or topographic patches are observed at the steel surface, like the ones observed in Slice 1.1. These are medium grey in the backscatter image compared to the unaltered iron surface which appear white to light grey (Fig. 6.22).

Black rust characteristics: The black rust corrosion products are characterized by high iron content and in some sites by additional chlorides and sulfur content. These compounds are often infiltrated in the altered cement paste and have replaced the ordinary cement paste minerals. Where calcium, silica and aluminum are replaced the cement paste is discolored by the corrosion products which show a brighter shade in the backscatter image. The corrosion products are often banded or layered with altered cement paste in between like seen in Fig. 6.21A.

6.2.2 Sample 2

General description hand specimen: This concrete drill core was sampled in the same locality as Sample 1. However the concrete configuration of Sample 2 differs. Sample 2 has a fine grained cement topping with an approximate thickness of about 40 mm. This cement topping forms a distinct border to the original concrete and has a different cement paste color, which is slightly more light grey in comparison. The corroded iron in this core is an expansion bolt. The bolt runs through the cement topping and into the concrete where it is anchored. Inside the bolt black rust with a crust of red rust is visible. Figs. 6.23A, B, are both slices from the center of this core sample. They have been cut to manageable pieces for use in the SEM analysis. A rust nodule was sitting on the surface of this core but were separated to be closer studied in a light microscope. The nodule was initially black but changed to red rather quickly after sampling (Fig. 24).

Sample Slice 2.1

Petrographic description: The fine grained cement topping is primarily comprised of sand particles and cement paste. Its composition differs from the concrete. The concrete has coarse rock aggregates of felsic granitic composition with a size of 10 – 20 mm and an angular shape. The sand particles are sub-angular to sub-rounded with a moderate chemical matureness; mostly quartz or quartz-rich grains and some fragments of granitic composition. A high content of silica was observed in the SEM in many of the sand particles.

Deterioration of cement paste and reinforcement: The topping of this core sample is clearly altered by carbonation. The carbonation front is distributed in the upper 10-15 mm from the surface and follow the bolt downwards in a concave shape. Further down the carbonation is laterally spread in the adhesion zone between the concrete and the cement topping. This is seen in Fig. 6.25, where the brighter area in the cement paste is situated. In the concrete below the topping only restricted carbonation is observed, especially

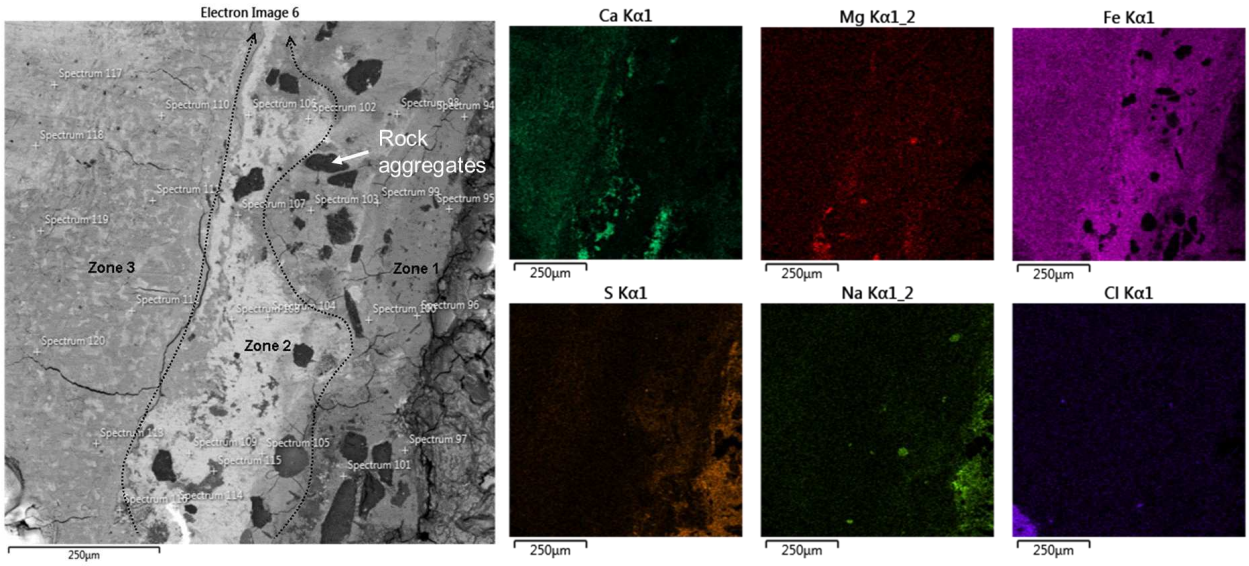

Fig. 6.21. Site 6 is here displayed in two ways: **A.** BSE image of the microdomain, and **B.** element maps of the most prevalent elements detected. Iron is generally distributed, but seems to be slightly more concentrated in Zone 2. Calcium is mainly occurring in Zone 2-3, and sulfur is more concentrated in Zone 3.

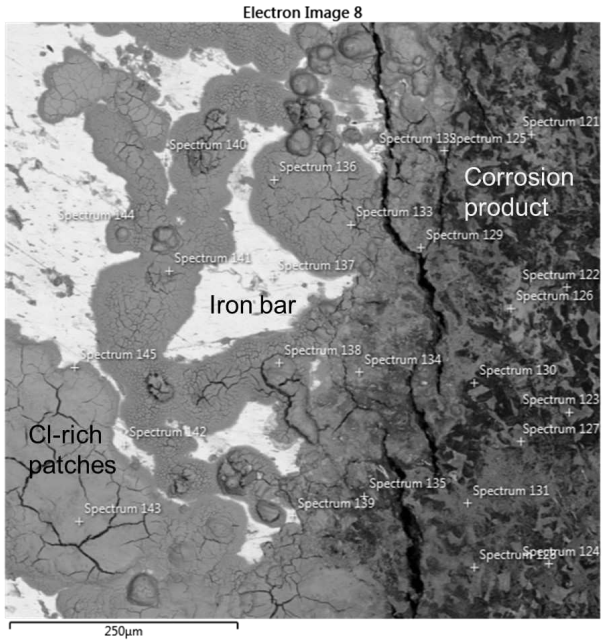

Fig. 6.22. BSE image of Site 8, Slice 1.2 is showing corrosion products in a dotted pattern. These are high in chlorides and formed on the iron surface after sample preparation. On the right side some corrosion product has infiltrated the cement paste.

close to the bolt. The visible cracks in Fig. 6.25 are related to the preparation of the sample and its drying process. Characteristic dehydration or expansion cracks were observed in the SEM between sand particles (Fig. 6.26).

Black rust characteristics: The corrosion products have accumulated at the surface, inside and outside of the bolt (Fig. 6.25). In the adhesion zone between the bolt and the cement paste an area of corrosion products has developed (Zone 2; Fig. 6.27). The contact is rather sharp between the cement paste and the corrosion product. The latter looks to be a part of the former reinforcement. The corroded area has the layering nature of black rust. It is possible to discern some layering in the corrosion product with alternating darker and lighter grey tones from the backscatter image. This is also seen in another microdomain (Fig. 6.28) closer to the surface of the sample piece. Within the cement paste area, corrosion products are appearing in the shape of liesegang patterns. These are circular and light grey layers in the cement paste with more iron content than the medium grey phases seen in the backscatter image.

SEM analysis of Slice 2.1

The area shown in the backscatter image of Fig. 6.27 gives a representative view of the adhesion zone between the bolt and the concrete some centimeters deep into the sample. The EDS analysis show a high iron content and a low weight percentage of calcium and silica within the corroded area. The cement paste (Zone 3) on the left side in the backscatter image (Fig. 6.27) show some rather normal to slightly altered Si/Ca and Al/Ca ratios (Fig. 6.29). Zone 1 and 2 represent the iron and corrosion product respectively (Fig. 6.27); it is not strange that these zones show dislocated ratios in Fig. 6.29. In microdomains closer to the surface, it is seen that a lot of iron have infiltrated the cement paste structure (Figs. 6.26 and 6.28). These microdomains seem more to be affected by the corrosion process compared to microdomains deeper in the concrete.

6.2.3 Sample 3

General description of hand specimen: The hand specimen from Sample 3 (Fig. 6.30A-C) is a concrete drill core from a flocculation basin in a water treatment plant. The surface of the concrete wall is the top of this drill core. Red rust covers the whole surface area but have accumulated mostly in the center and building up the rust nodule (Fig. 6.30A). A part of the corroded

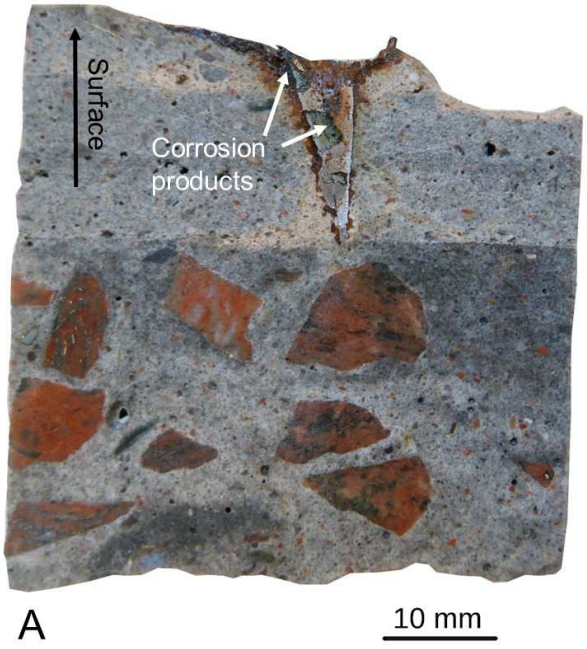

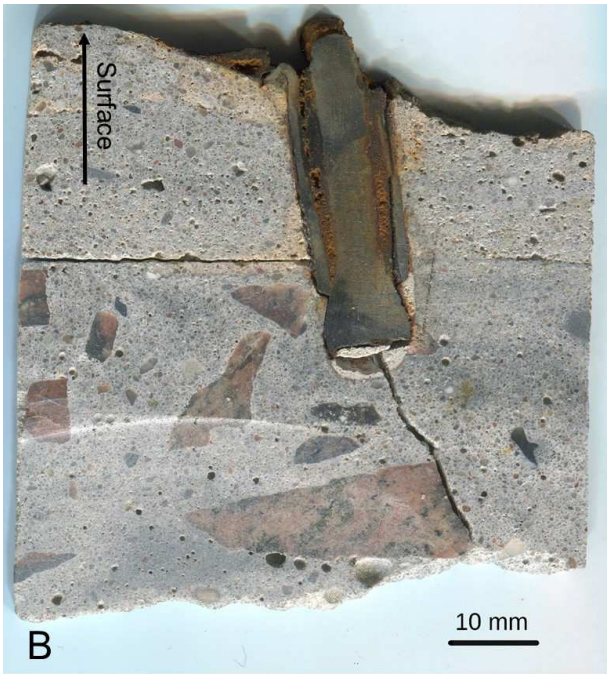

Fig. 6.23. The central core pieces of Sample 2. These have no reinforcement, but a bolt that has corroded. **A.** The iron bolt has newly formed corrosion products which are red or dark green to black. **B.** The black corrosion products within the bolt have started to transform to red rust.

reinforcement is visible on the side of the core, and the concrete around show rust stains (Fig. 6.30B). The reinforcement cross section is completely covered with black rust (Fig. 6.30C). This is a sign of complete degradation, which is also seen in Thin section 3.

Thin section 3 (TS 3)

Petrographic description: An overview of thin section 3 is seen in Fig. 6.31. In the upper part of the thin section, between the surface and the reinforcement, there

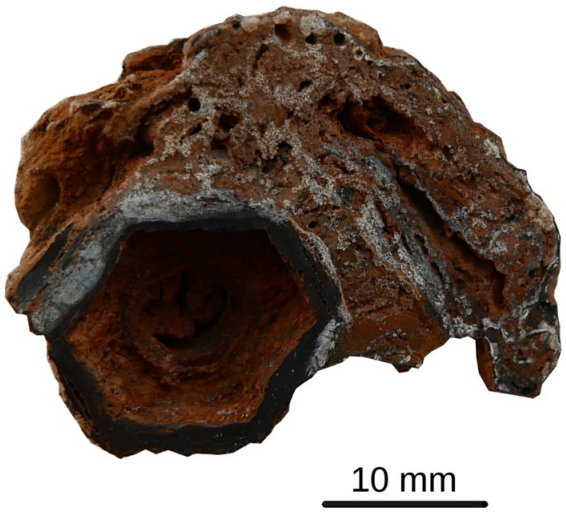

Fig. 6.24. A rust nodule from Sample 2. This one have been sitting on top of the bolt with a screw-nut, from which the hexagonal shape still can be seen. Generally it is a porous part of the corrosion products, however this contain rigid layers of black rust within the red rust matrix.

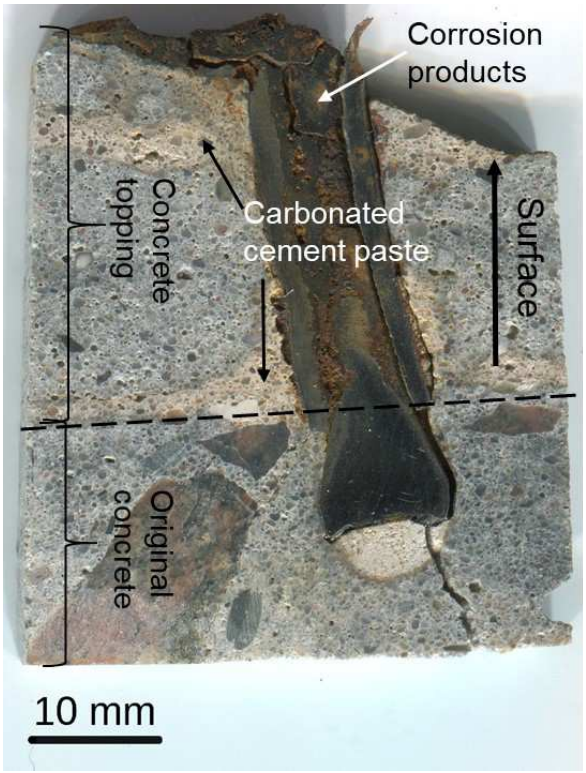

Fig. 6.25. Corrosion products are visible in the iron bolt. These were initially black, but have by this time started to oxidize to red rust. The cement paste in the concrete topping is carbonated along the surface, bolt and adhesion zone to the original concrete.

is a fine grained cement/mortar mending. The mending is discolored by red corrosion products at the uppermost part. Only remnants of the reinforcement are visible slightly above and to the right of the core center. The sample contain several fractions of ballast aggregates. One coarse fraction with angular to sub-angular

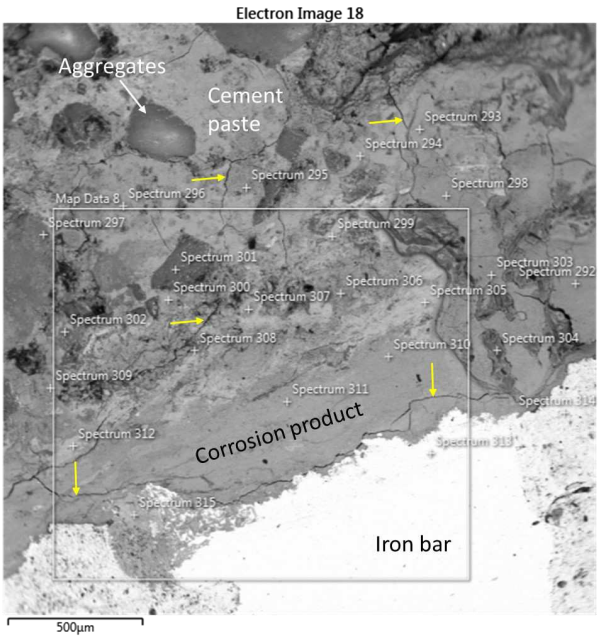

Fig. 6.26. Micro cracks are marked out with yellow arrows. In between the cement paste and the iron there is a zone of corrosion products.

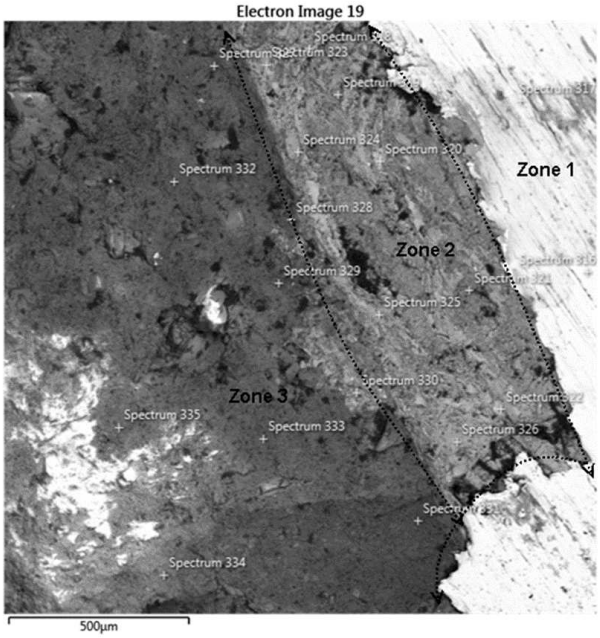

Fig. 6.27. A zone with corrosion products (Zone 2) in between the iron (Zone 1) and cement paste (Zone 3) has rather distinct borders. It seems to be a layered structure in Zone 2, which are likely to be a mixture of interlayered corrosion products.

aggregates (10-30 mm) of fine grained granitic gneiss and aggregates of dolerite with circa 40-50% mafic minerals (green amphibole, biotite and opaque phases). The medium fraction (5-10 mm) have a similar composition as the larger aggregates and cryptocrystalline quartz (flint) is also observed. Sand particles (1-3 mm) are mainly dominated by monocrystalline or polycrystalline quartz, feldspar and single grains of biotite. The porosity of the concrete is enhanced by the

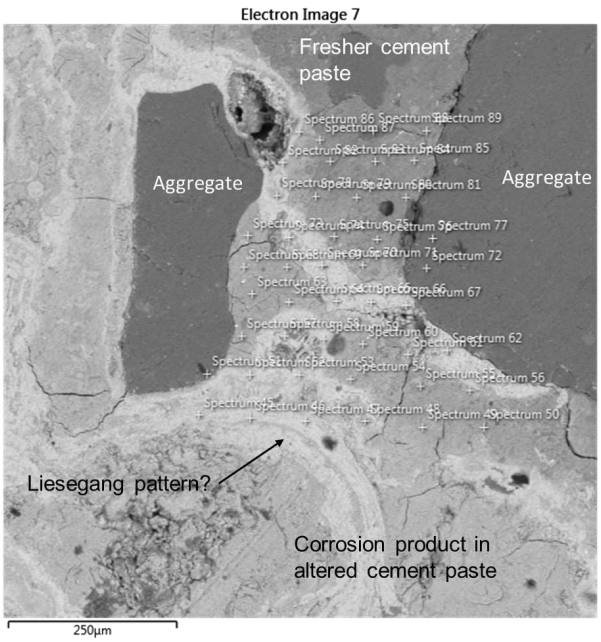

Fig. 6.28. The banded or layered structure that these corrosion products show are resembling of liesegang patterns. The lighter layers are slightly richer in iron compared to the areas in between.

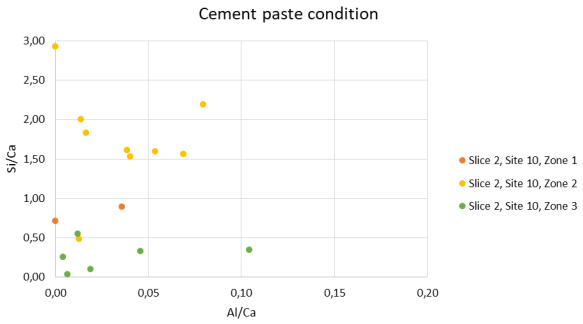

Fig. 6.29. Zone 3 in Site 10, Slice 2.1 show rather normal Si/Ca vs. Al/Ca ratios. Zones 1-2 are other phases (iron and corrosion products respectively) and are thus showing dislocated ratios.

fluorescent dye in the epoxy resin. The porous areas appear yellow and the denser areas appear dark green in UV-light.

Deterioration of cement paste and reinforcement: The cement paste is altered, especially at the surface and around the corroded reinforcement where discoloration and a higher porosity is distinctive. No defined carbonation front is observed; instead the carbonation follows cracks and pore connections that contain corrosion products. This is most clearly seen as light beige spots in the polarized photo of TS 3 (Fig. 6.31B). Cracks vary in length and can be traced several mm to cm from the surface into the sample towards the reinforcement. Most of the cracks are located between the grain boundaries of aggregates, but also adhesion cracks around the aggregates are common. Generally, the cracks are around 50-100 µm wide. Thinner microcracks were identified in the SEM. Close to the surface

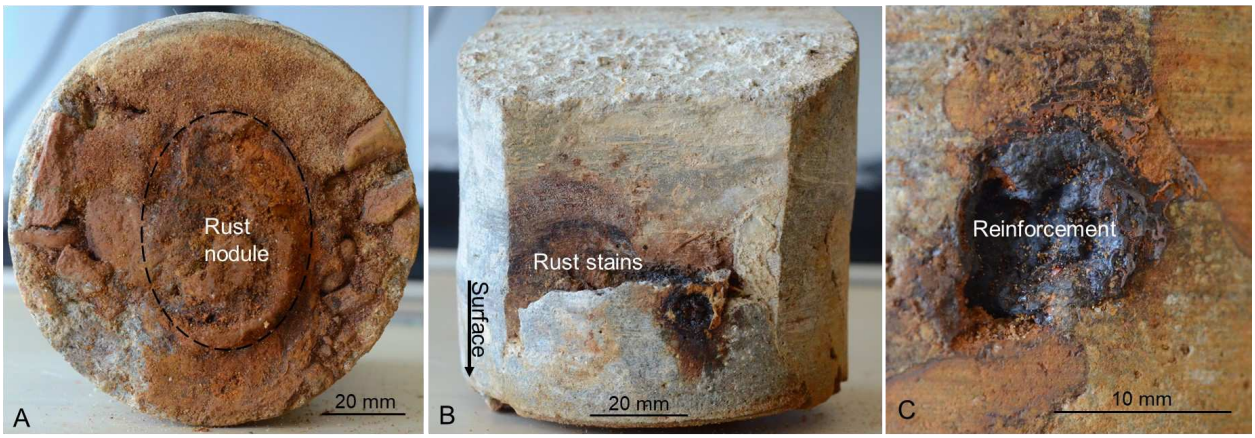

Fig. 6.30. The hand specimen of Sample 3 show several signs of deterioration of both cement paste and reinforcement. **A.** The surface of the concrete wall is represented by the top of this drill core. A rust nodule is covering the surface with red rust. **B.** Rust stains are seen around the reinforcement and at the side of the drill core. **C.** The reinforcement is totally covered with black rust. *Photos:* Fredrich, B.

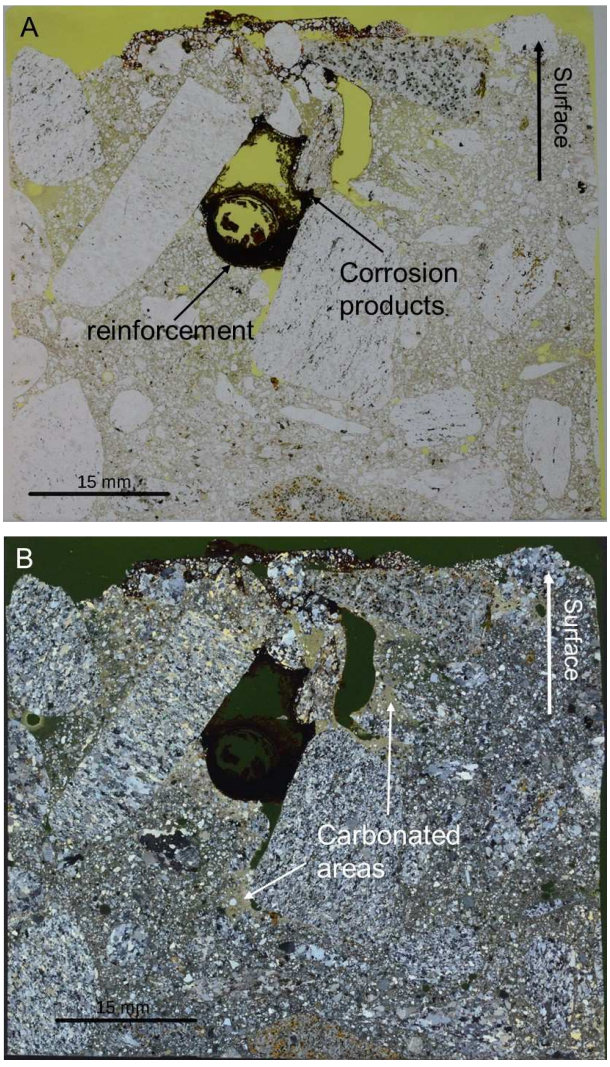

Fig. 6.31. Thin section 3 is shown in **A.** normal light where corrosion products are easily distinguished from the concrete, and **B.** polarized light, in which alteration of the cement paste (carbonation in this case) is easier to detect.

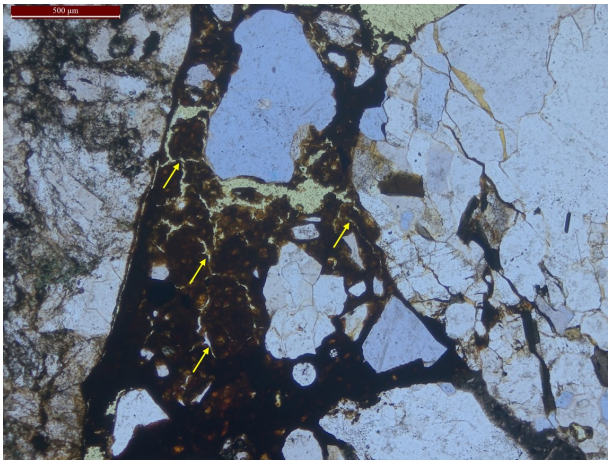

Fig. 6.32. Micro-cracks (yellow arrows) within the corrosion product is here a sign of dehydration or expansion. The scale bar in the upper left corner is 500 µm.

the cracks seem to be related to dehydration. This crack pattern can be seen within the corrosion product in Fig. 6.32. The cracks are often empty or contain crystals of ettringite ($Ca_6Al_2(SO_4)_3(OH)_{12} \cdot 26H_2O$) or portlandite ($Ca(OH)_2$). In Fig. 6.33 the cracks go through the ballast particles and are filled with both black and red corrosion products. Some air voids are filled with ettringite and portlandite.

Black rust characteristics: Corrosion products identified in the thin section are opaque. Black or red-brown rust colors are observed and more easily distinguished in reflective light. The black rust can be distinguished from the red rust as it appears dark grey/black instead of brown/red/yellowish (Fig. 6.33). These differences were most easily seen using the dark field method. The black rust commonly occupies voids and cracks as a non-crystalline mass that can have a layered and ring-like structure with interlayered red rust (Figs. 6.34A-B). Black corrosion products are infiltrated in the cement paste which have altered the cement paste color (Fig. 6.35). Ring shaped or banded black structures within the red rust colored cement paste are primarily observed close to the surface and around the reinforce-

ment. These structures have a similar appearance to liesegang rings seen in previous samples. This is primarily seen in the scanning electron microscope. In voids that are partly empty, as in Fig. 6.36, thin and elongated crystalline needles are observed. These are most commonly observed close to the reinforcement.

Sample Slice 3.1

This slice is a part from Sample 3 and is a remainder from the thin section production (Fig. 6.37). The core piece is impregnated with a yellow epoxy resin that has infiltrated the open pore system and is surrounding the core piece. Between the surface and the reinforcement there is a fine grained cement/mortar mending. The mending has a lighter grey shade than the original concrete and is discolored by red corrosion products at the uppermost centimeter. The epoxy resin is sometimes appearing green in contrast to the mortar, as seen close to the surface of the slice. Only remnants of the reinforcement are visible, see Fig. 6.37. The central area, around the reinforcement, has a darker shade due to the carbon coating.

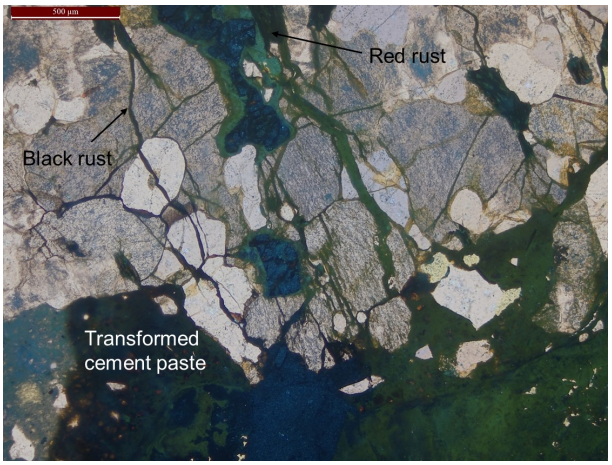

Fig. 6.33. Black rust within cracks that cross ballast particles. Red rust is mainly seen in the transformed cement paste. The scale bar is 500 µm.

SEM analysis of Slice 3.1

The surface cement paste of Slice 3.1 is not a part of the original concrete but a repair mortar. It has a rather normal chemical composition with respect to the aluminum/calcium and silica/calcium ratios seen in Fig. 6.38. However, the magnesium content is slightly higher than normal. The cement paste in the deeper parts of the sample contain even higher amounts of magnesium, up to almost 20 wt. % in some spots (Table A26). These spots are observed in the cement paste of Site 13. This site has a rather altered composition of cement paste compared to a fresh paste and it shows a network of fine cracks that are smaller than 10 µm (Fig. 6.39).

In the areas around the reinforcement the cement paste has an altered chemistry and almost all cement minerals are broken down. Cement building elements (commonly Ca, Al, and Si) are only found in minor proportions in the EDS analysis. Only a small quantity of these compounds is left in the altered cement paste. It is illustrated by the relationship between the silica/calcium ratio and iron in Fig. 6.40. Instead there are mostly iron compounds and chloride rich regions that are replacing the cement building elements. The element maps in Fig. 6.41 are showing the element distribution in Site 8, where corrosion products are infiltrated in the cement paste. The ballast particles are left as relicts in the transformed cement paste, just like in Fig. 21A. The Si/Ca – Al/Ca ratios for this site reveal the degree of alteration in the transformed cement paste (Fig. 6.40).

The liesegang-like structures in the iron rich corrosion products are seen in several microdomains. Fig. 6.42A-B are examples of how the iron-rich structures looks like in this sample. Darker and lighter layers are alternating in the backscatter images. A slightly higher iron content is registered in the lighter layers (about 0.5-3 wt. % higher in average).

6.2.4 Sample 4

General description of hand specimen: The hand specimen of this sample is one half of a concrete drill core. It has not been polished after the sawing process like

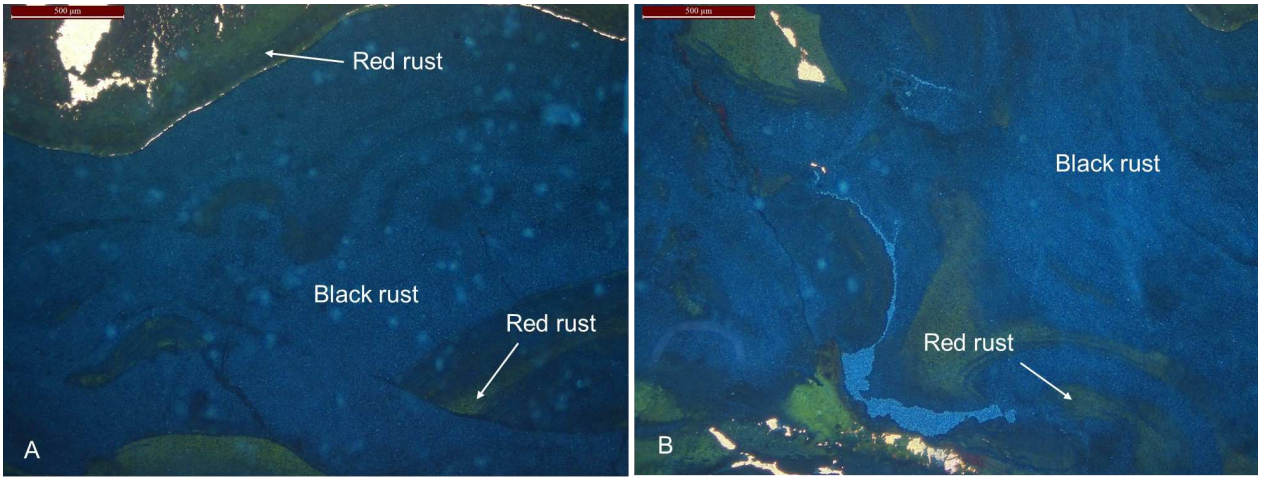

Fig. 6.34. Photomicrographs (ppl, darkfield mode) of the layered corrosion products of black rust in the transformed reinforcement. **A.** and **B.** both show corrosion products with a banded appearance where black and red rust are interlayered with red rust. Scale 500 µm.

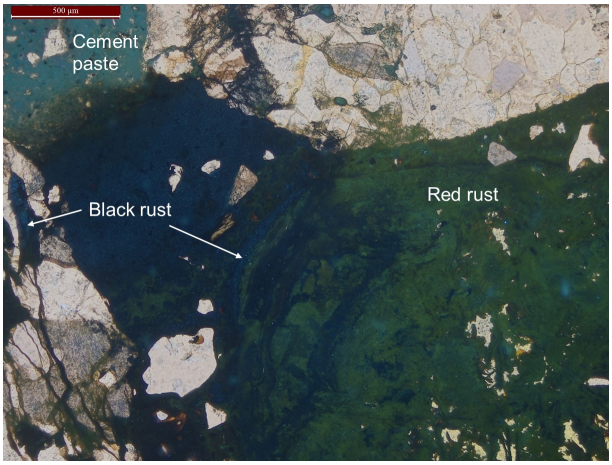

Fig. 6.35. The cement paste between two rock aggregates are more or less completely transformed to black and red rust. Scale 500 µm.

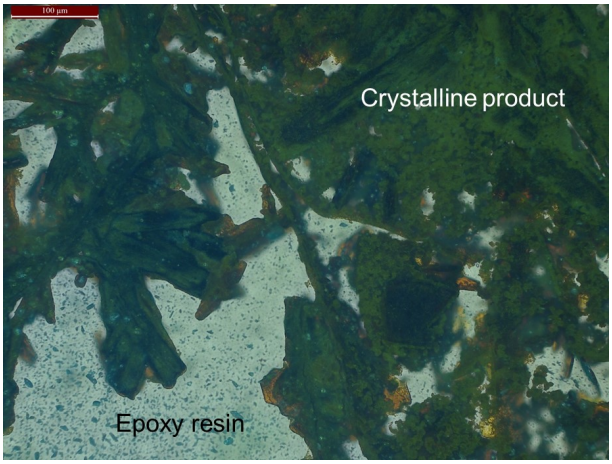

Fig. 6.36. Elongated crystalline products have grown within the hollow reinforcement bar. The darkfield mode in ppl is displaying these products as semi-transparent (brown crystals). Scale 100 µm.

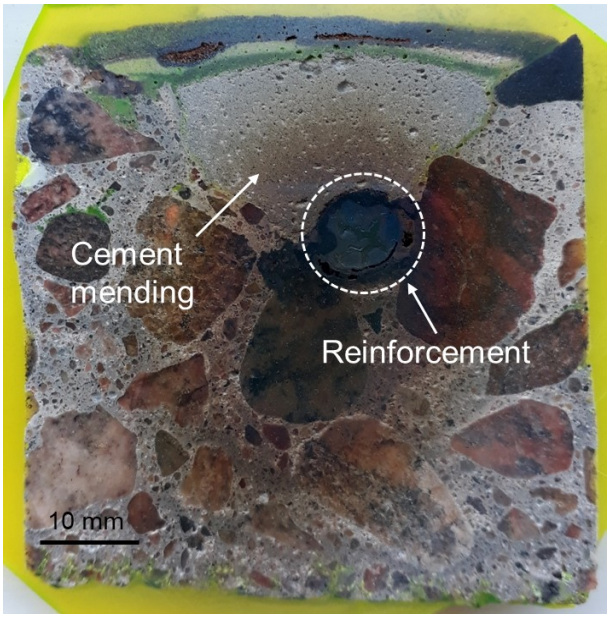

Fig. 6.37. An overview of Slice 3 that was analysed in the scanning elecrton microscope.

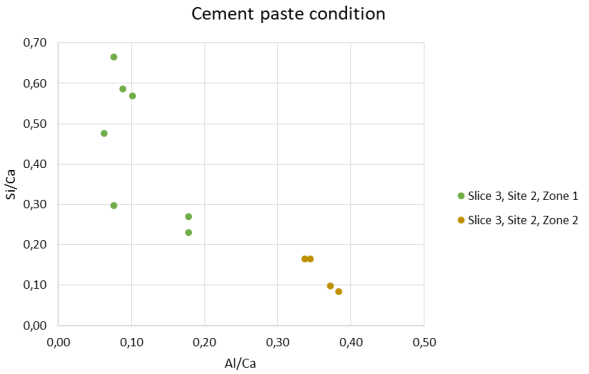

Fig. 6.38. Cement paste condition of Site 2 in Sample 3. The cement paste in the mending show rather unaltered Si/Ca – Al/Ca ratios.

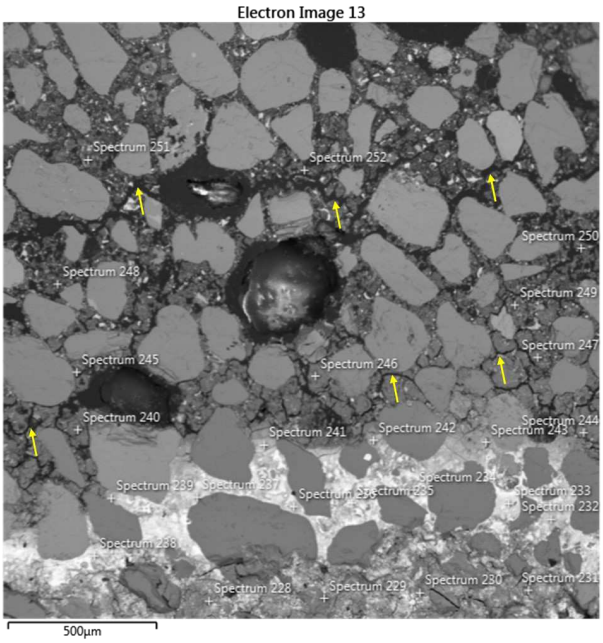

Fig. 6.39. A network of thin and dark epoxy filled cracks are pointed out with yellow arrows. The light band in the lower part of the BSE image is high in iron.

the other cores, which means it is the least processed core. In the cross section (Fig. 6.43A) the first 0 – 10 mms are covered by a discolored rusty layer in the cement paste. On the curved side (Fig. 6.43B), the rust colored cement paste carves deeper into the core than seen on the cross section. The discolored region is surrounding at least one larger cavity in the cement. A view from the top in Fig. 6.43C, show that the surface of the concrete wall is slightly eroded; the cement paste has vanished and only the ballast grains are left in the upper 0-5 mms. The concrete cover above the reinforcement is about 50 mm thick. Both black and red rust products are visible at the reinforcement cross section and the back side.

Thin section 4 (TS 4)

Petrographic description: An overview of the thin section is seen in Fig. 6.44A-B, in both normal transmitting light and in polarized light. Coarse aggregates are angular, and the particle size is between 10-30 mm.

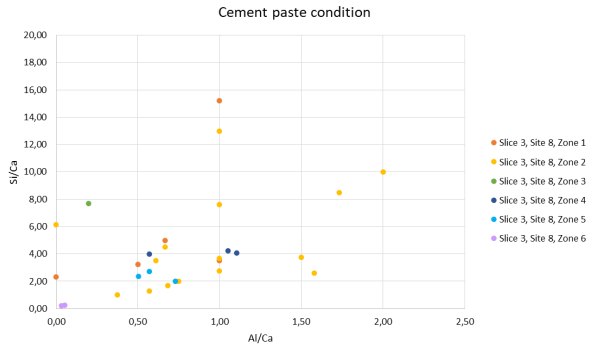

Fig. 6.40. Most of the Si/Ca vs. Al/Ca ratio values in Site 8 are very high, which indicate that the cement building elements are gone from the structure.

These are mainly dolerite with mafic mineralogy (30-50% green amphibole and biotite) and with a gneissic texture. The feldspar grains look altered and show seritization. A particle of red weathered gneiss is also observed in this grain-size fraction. Felsic granitic to tonalitic gneiss aggregates dominate the smaller fractions (circa 3-10 mm) together with angular to sub-angular sand fragments (0.5-2 mm), which mainly comprise monocrystalline or polycrystalline quartz, feldspar and biotite. The air distribution in this sample is not ideal. Air voids are aggregated irregularly within the sample. The porosity varies within the sample and is higher close to the surface and around the rebar where the cement paste looks carbonated.

Deterioration of cement paste and reinforcement: The cement paste is highly altered at the surface. Discoloration from the corrosion products is visible within a depth of 0-7 mm from the surface (Fig. 6.44). Signs of carbonation are clearly visible within circa 15 mm from the surface and in patches down to the reinforcement. Around the reinforcement the carbonation appears in a circa 10 mm thick halo (Fig. 6.44B). Carbonated and discolored cement paste are also observed along cracks and air voids that contain corrosion products. Most of these cracks are connected to the concrete surface. Narrow surface cracks that look like dehydration cracks are located between rock aggregates or voids (Fig. 6.45A-B). Longer and more continuous cracks up to several centimeters can be observed deeper in the sample. Some of these can be traced from the reinforcement, along rock aggregates and towards the surface. Thinner cracks, 50-100 µm in width, are located between empty or filled voids. There are several sets of cracks in this sample that are of different magnitude and containing various elements. Some of the empty cracks may be related to the preparation. Fibrous ettringite (Fig. 6.46A-B) and crystalline portlandite (calcium hydroxide; Fig. 6.48A-B) are commonly observed as a filler in the voids and cracks. Corrosion products can also be found within the cracks, especially around the reinforcement and in near surface cracks. These corrosion products are commonly black or red and show a layered habit. Wide and open cracks are generally only filled with epoxy resin or are empty.

The reinforcement is clearly affected by the corrosive environment in the sample. Depressions at the iron surface have been filled with black corrosion products (Figs. 6.48A-B). The adjacent cement paste has been discolored and bulges of red corrosion products, covered by a crust of black rust, penetrate into the surrounding cement paste (Figs. 6.48B-C).

Black rust characteristics: The corrosion products are mainly distributed around the reinforcement and at the surface. Within the near surface cement paste there is mostly red rust observed. Close to the rebar black rust is typically found in pits at the surface of the rebar and at the surface of red rust corrosion mounds. The black corrosion products appear to form a crust layer over these mounds (Figs. 6.48B-C). Closer to the surface black rust is present in voids and cracks. In spacious cracks or voids, like in Fig. 6.49, the black to dark grey corrosion product is sitting in contact with the cement paste. The black product shows rounded mounds towards the center of the void (Fig. 6.49) where upon brown to red crystalline needles are sitting. These needles are very similar to the ones observed in Sample 3 (Fig. 6.36).

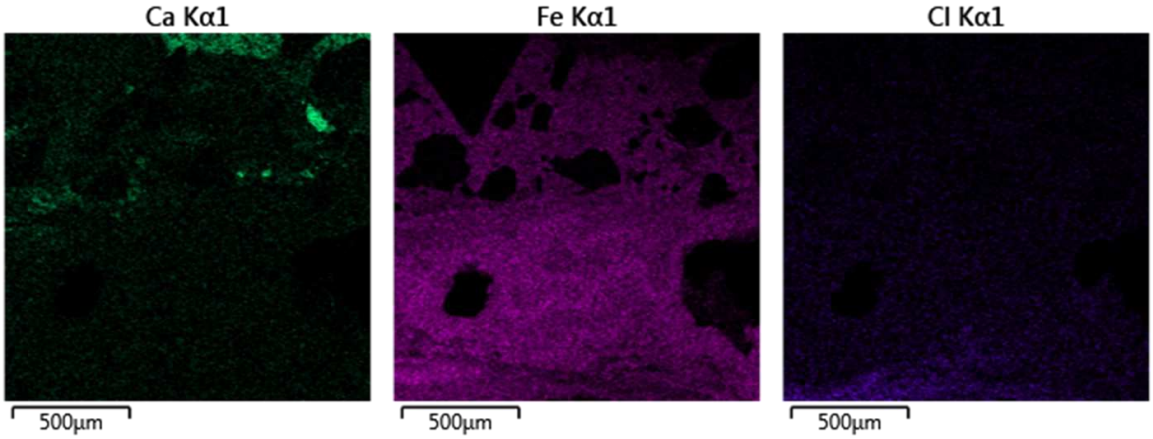

Fig. 6.41. Element maps of Site 8 is showing the lack of calcium and the dominance of iron within this microdomain. Some amounts of chloride is also present in the lower regeon of the microdomain.

7 Discussion

This chapter contains four sections. Results from the literature review, and the SEM and optical microscopy are discussed and compared in Sections 7.1 and 7.2. The subsequent section (7.3) provides an evaluation of how the presently used methodology (Chapter 4) have affected the analyses results. It also provides suggestions of methodological improvements. Finally, Section 7.4 stresses the need of future studies within the field of black corrosion and its resulting products.

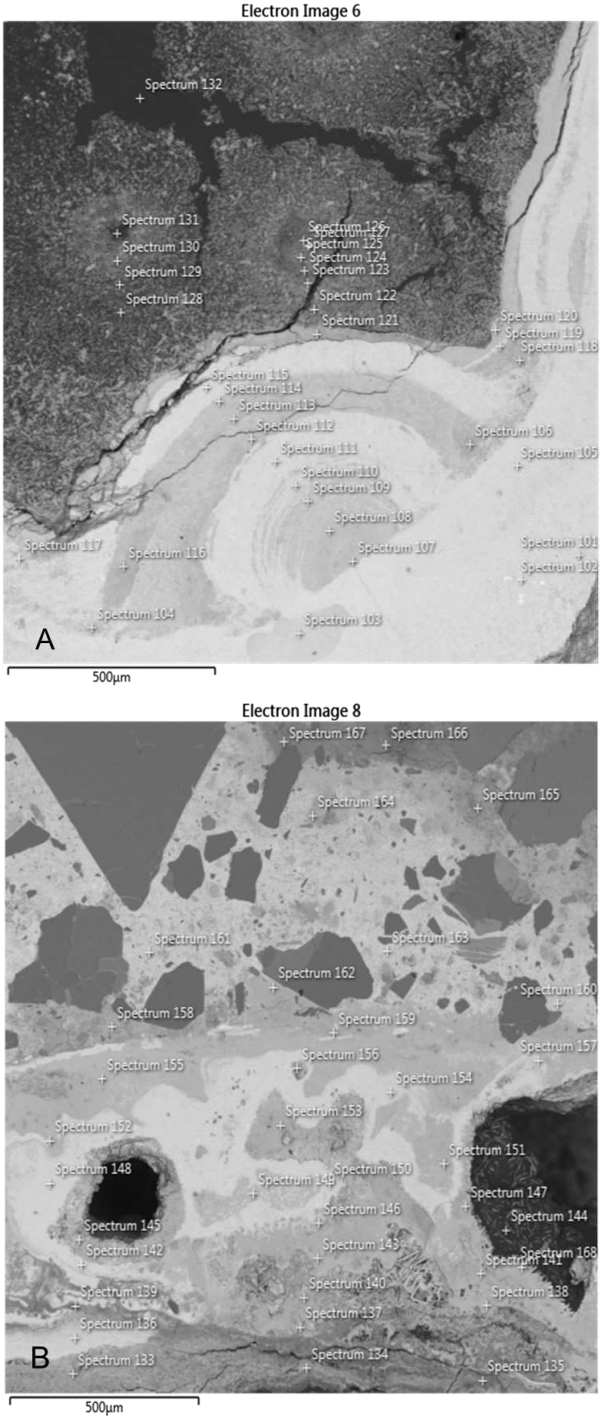

Fig. 6.42. The BSE images of **A.** Site 6, and **B.** Site 8 are showing iron-rich structures. A slightly higher iron content is registered in the lighter layers.

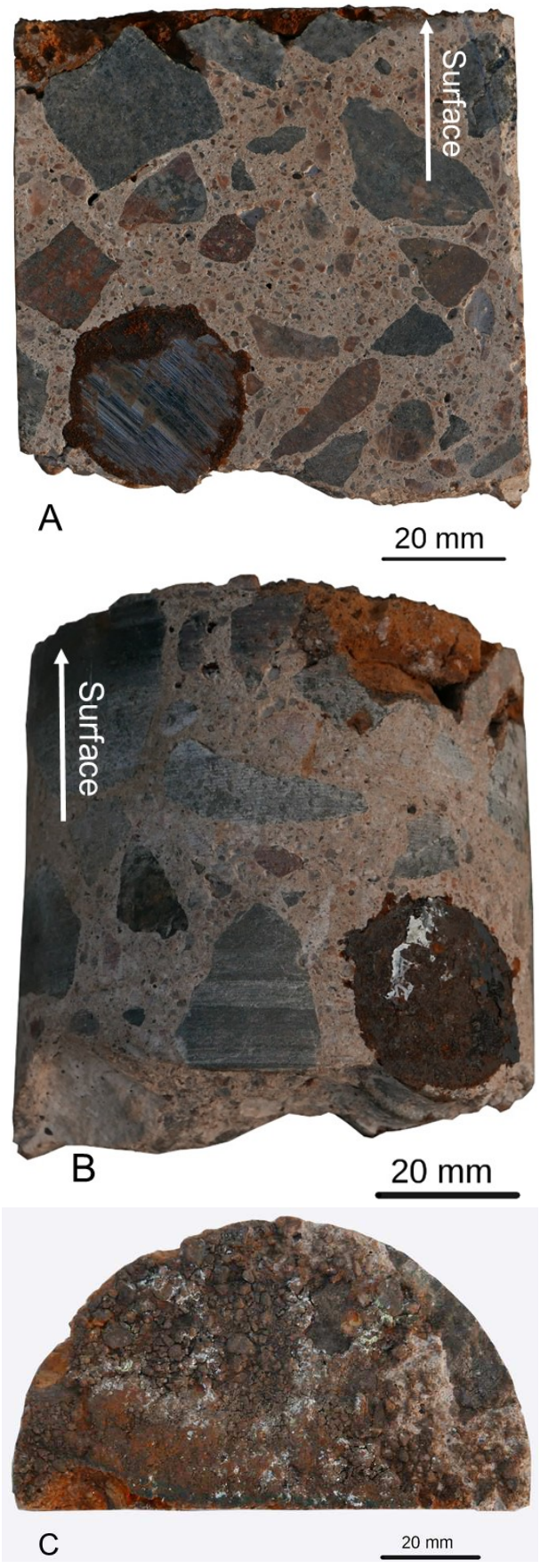

Fig. 6.43. The hand specimen/drill core of Sample 4 seen from. **A.** cross sectional view, **B.** the curved outer side, and **C.** the surface (i.e. outer concrete wall).

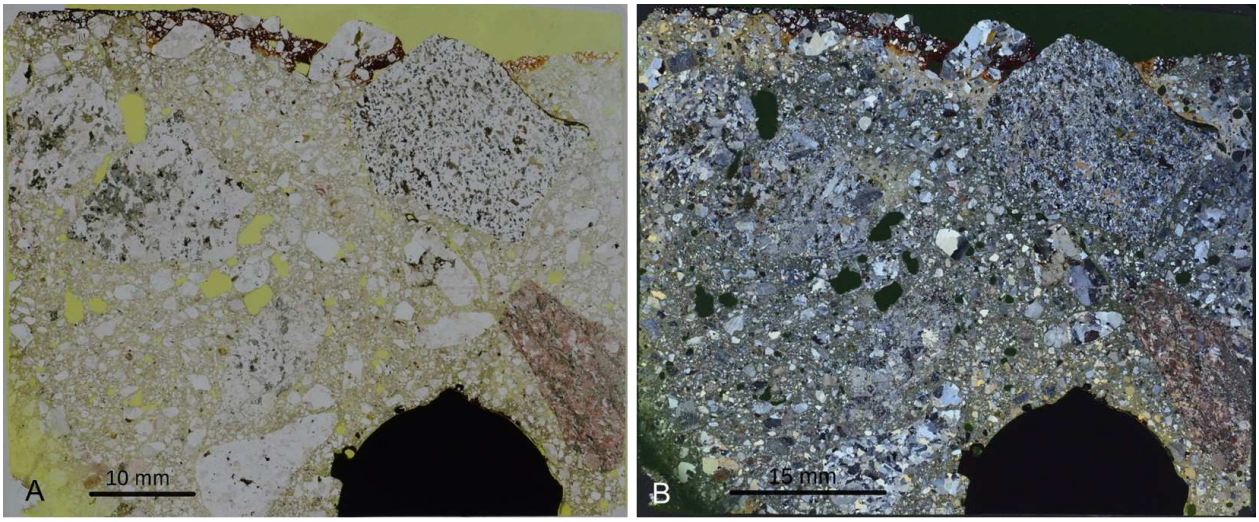

Fig. 6.44. Overview of thin section 4, **A.** in normal light, and **B.** in polarized light. The cement paste in the upper centimeter and around the reinforcement looks carbonated.

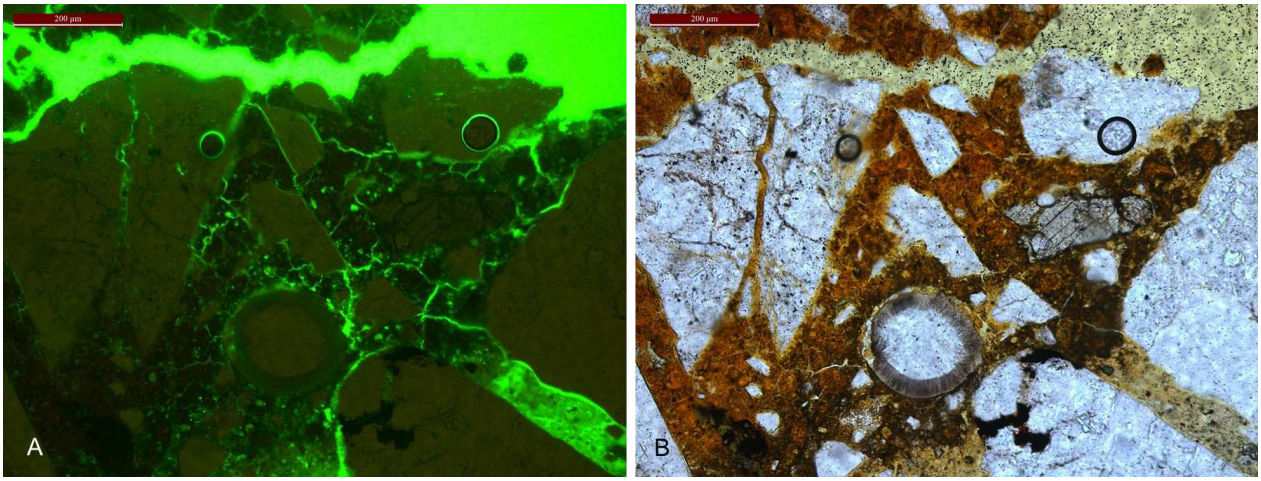

Fig. 6.45. Thin dehydration cracks in the transformed cement paste close to the surface. **A.** The fluorescent dye in the epoxy resin enhance cracks and porosity in the cement paste when it is illuminated with UV-light. **B.** The corrosion products are more visual in ppl. Scale 200 µm.

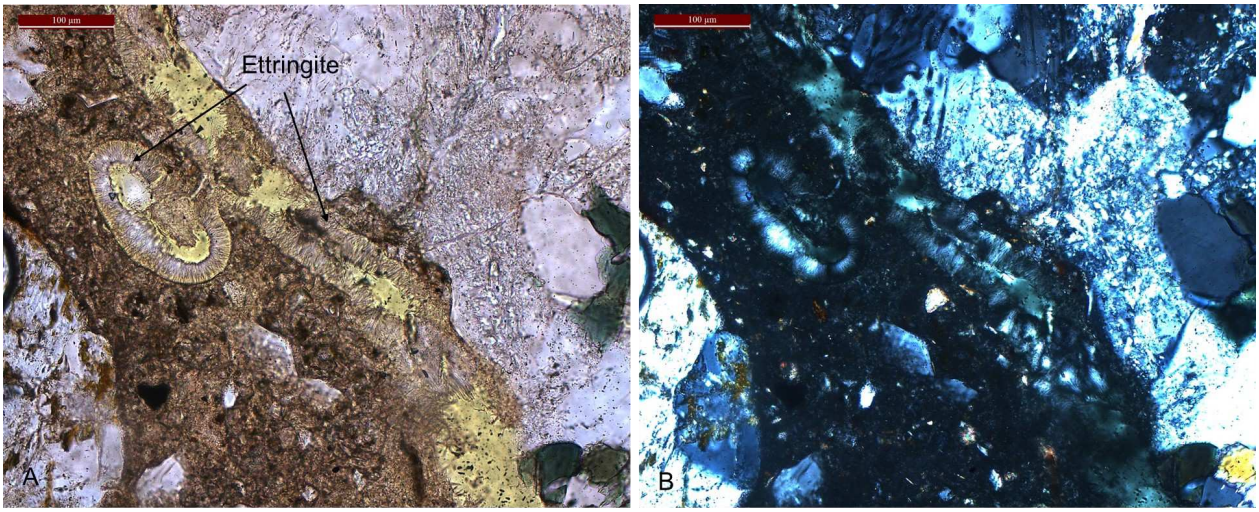

Fig. 6.46. A crack and with connected void filled with fibrous ettringire ($Ca_6Al_2(SO_4)_3(OH)_{12} \cdot 26H_2O$) in **A.** ppl, and **B.** xpl. The ettringite is often a sign of that the concrete experienced a sulfate attack. Scale 100 µm.

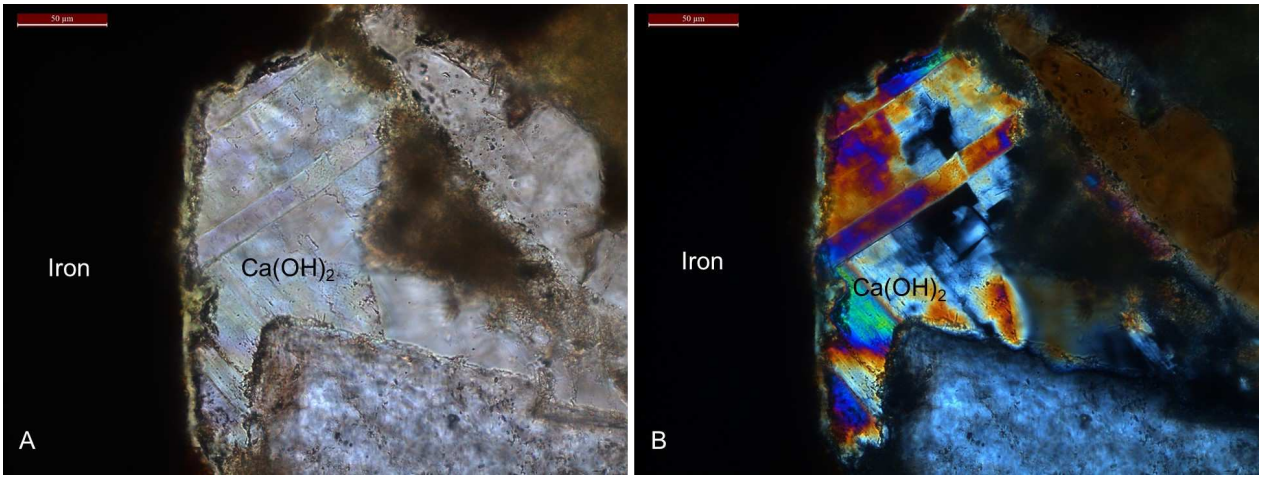

Fig. 6.47. A relatively large crystal of calcium hydroxide ($Ca(OH)_2$; probably portlandite) observed a crack between the reinforcement and cement paste in Thin section 4, **A.** ppl, and **B.** xpl. Scale 50 µm.

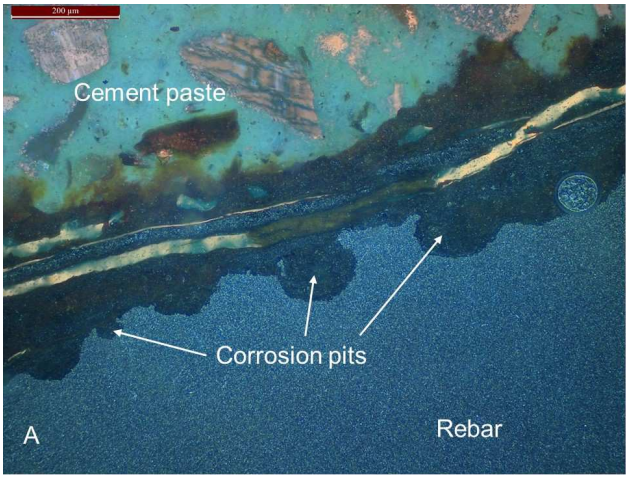

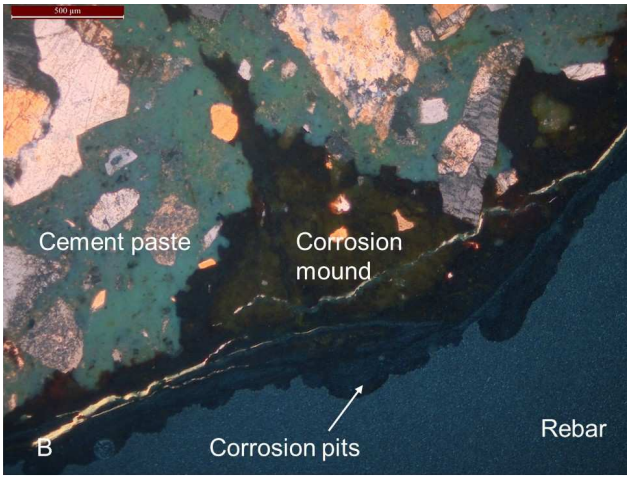

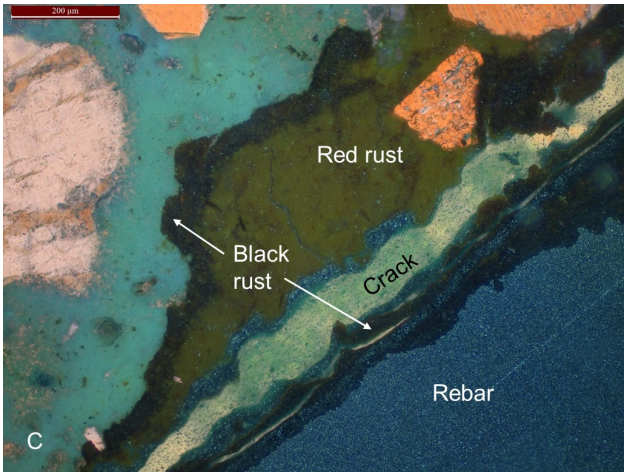

Fig. 6.48. Along the reinforcement bar (rebar) depressions have been formed in the iron. This is clearly seen in both **A.** and **B.** In all of the figures (**A-C**), red rust products with a black crust are penetrating the cement paste. An epoxy filled crack is separating the iron from the cement paste. Photomicrographs are in xpl, darkfield mode, scale 200 µm.

7.1 Theoretical Results

The most relevant findings from the literature study is here discussed and compared to the description of the corrosion products in this work (Subsection 7.1.1). Also a developed discussion of the relations between black and green rust is provided in Subsection 7.1.2. The corrosion process and the potential involvement of microorganisms in the studied samples is evaluated in Subsection 7.1.3.

7.1.1 Observed black rust in relation to literature

Generally the descriptions of black rust as a corrosion product in reinforced concrete are ambiguous within the literature reviewed. According to some authors, the black colored corrosion products described are specified as black rust (e.g. Tuutti 1982; Broomfield 2007; Fatemi et al. 2011; O'Donovan et al. 2013; Jacobsson 2016). However, most of the literature that mentions black corrosion products are referring to different designations, such as black precipitates, black materials, black oxides or black colored corrosion products. These are not always identified as black rust but rather other corrosion products of iron, commonly magnetite (Fe_3O_4), maghemite ($Fe(III)_2O_3$), goethite (α-Fe(III)OOH), lepidocrocite (γ-Fe(III)OOH), siderite ($FeCO_3$), etc. (e.g. Bernal et al. 1959; Ona-Nguema et al. 2002b; King 2008; Vera et al. 2009; Miot et al. 2014; Usher et al. 2014). Hence it is difficult to know if the researchers refer to the same kind of black corro-

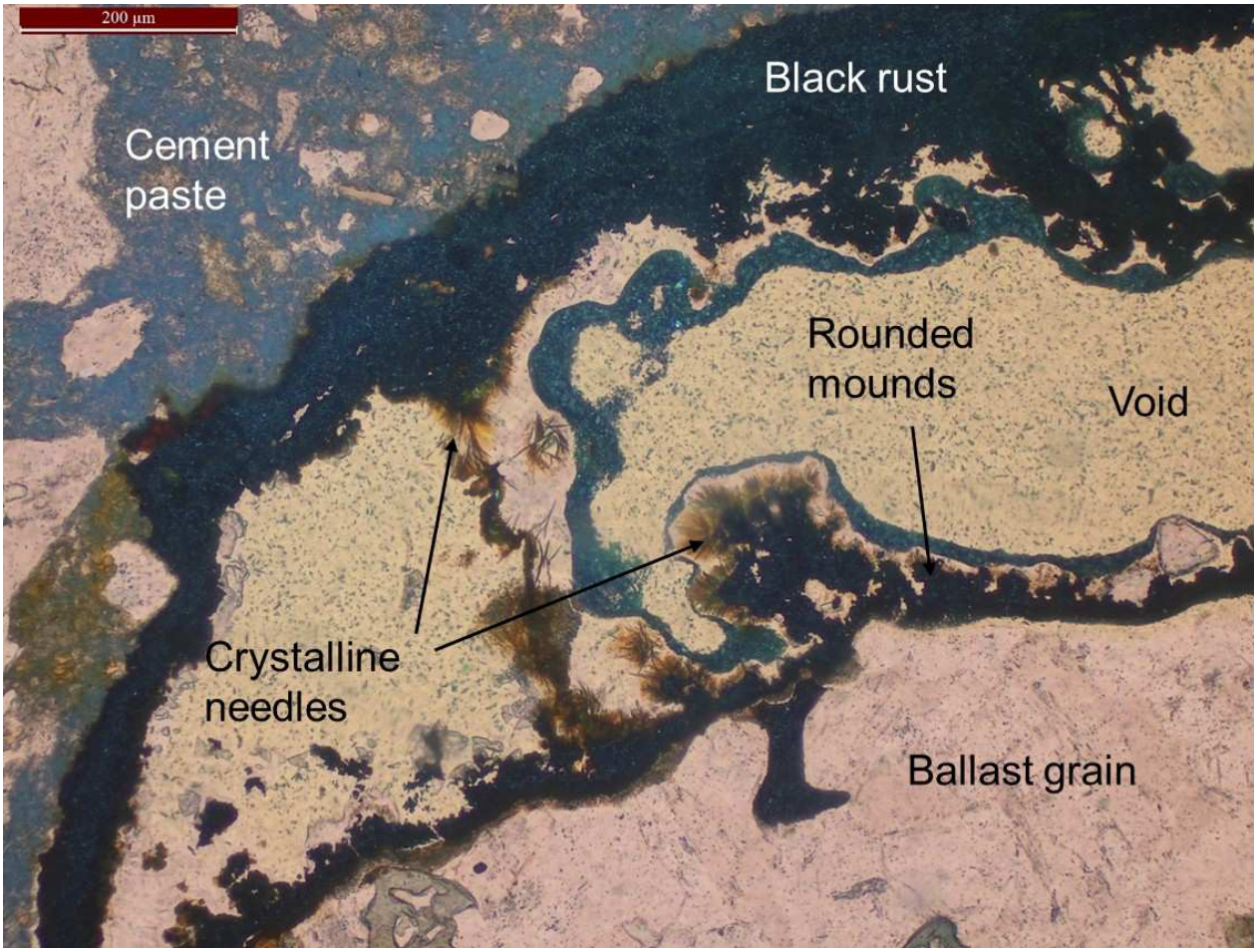

Fig. 6.49. Black rust and other corrosion products in a void close to the surface. The photomicrograph (in ppl, darkfield mode) is showing the different layers of products where the outer is the oldest product and the most central is the one which is most recently formed. Scale 200 µm.

sion product in their descriptions, or if the name "black corrosion product" is used as an umbrella term for different corrosion species of the same color.

The description of black rust in the literature (Fatemi et al. 2011; O'Donovan et al. 2013) is overall consistent with the results in this study. Mainly it is the color description by Broomfield (2007), Wong et al. (2010) and O'Donovan et al. (2013) that deviates. Their description can give the reader a sense of that black and green rust might be the same corrosion product. However that is not the case as both the literature review (Chapter 5) and the EDS results (Section 6.2) show that black rust should not be confused with green rust. Black and green rust evolve in similar environments (i.e. alkaline and oxygen deficient; Refait et al. 1998; 2006; 2011) and may be related to each other through oxidation, dehydration (Bernal et al. 1959; Świetlik et al. 2012; Miot et al. 2014) or bio-reduction processes (Ona-Nguema et al. 2002a; Ona-Nguema et al. 2002b; Vera et al. 2009). Additionally, McGill et al. (1976) presented evidence of epitaxial growth of magnetite on green rust but they only speak about black magnetite or black oxide, which leaves the black rust to a question of interpretation.

7.1.2 Black and green rust relations

Although black and green corrosion products differ in their chemical composition and structure, they both seem to play a part within the same corrosion process. Particularly the discoveries by Bernal et al. (1959) leads to the interpretation that green rust may be a precursor to black rust, as a result of oxidation and dehydration. Different varieties of iron oxyhydroxides (FeOOH) and magnetite (Fe_3O_4) are the result of these processes (Bernal et al. 1959; Miot et al. 2014). The transformation of green rust to other corrosion products in environments with high alkalinity (e.g. concrete), requires a lowered pH in order to occur as with ordinary corrosion processes (Section 2.2). Thus it is likely that these reactions are initiated during for example carbonation of the cement paste. In contrast to the above statements of black and green rust relations, Duffó et al. (2004) report that green rust is formed on the expense of magnetite due to a weakened passive layer. Further oxidation then evolves the green rust to commonly goethite and lepidocrocite. This may seem strange since black rust has been described to be chemically close to magnetite, though it is never assigned to be magnetite.

Corrosion research is prosperous within the field of green rust which scientifically proves its structure and relation to other iron-based corrosion phases. In contrast, the constituents of black rust are hard to specify by only reviewing the present literature. Thus there are still many areas to investigate corrosion science re-

garding black rust. Some suggestions are presented in Section 7.3.

7.1.3 Corrosion processes and microbial influence

The black rust phenomenon can be divided into several mechanisms such as corrosion initiation, transportation and precipitation. The anaerobic corrosion process could be initiated by impurities in the reinforcement or by outer factors such as carbonation or chloride attack. Microorganisms are another possible driving factor in the corrosion process (Refait et al. 2006; Duan et al. 2008; Refait et al. 2011; Świetlik et al. 2012; Miot et al. 2014; Usher et al. 2014). It is recognized that microbial influenced corrosion (MIC) is an important part to consider in corrosion science (Usher et al. 2014). Among the reviewed literature the formation of green rust seem to be strongly related to the activity of microorganisms, especially sulfate reducing bacteria (SRB; Refait et al. 2006; Rémazeilles et al. 2009; Refait et al. 2011; Usher et al. 2014; Walsh 2015) and dissimilatory iron-reducing bacteria (DIRB; Ona-Nguema et al. 2002a; Refait et al. 2006; Zegeye et al. 2011). The microorganisms are not only a driving mechanism in the corrosion process. They are also capable of changing the local chemical environment in the concrete, often by lowering the pH (Smart & Adams 2006). This could have a negative effect on the concrete itself and may act as a catalyst to other corrosion driving processes (Fagerlund 1992; Refait et al. 2006). Miot et al. (2014) showed that microorganisms can even control the corrosion rate to some extent. In their experiment a nitrogen-reducing bacteria species contributed to a faster oxidation process (a few days) of the green rust while the same process takes months when abiotically controlled.

The samples showed areas of elevated amounts of sulfur and iron, or chloride and iron contents in the EDS analyses of the corrosion products (Samples 1 and 3). However, these compounds are not necessarily related to microbial activity, but are most likely derived from seawater that has been infiltrating the concrete. There were no direct signs of microbial activity within the examined samples. But the samples come from environments that have the prerequisites for microbial influenced corrosion, at least the samples from The Sound. With respect to the conditions in this locality (seawater saturated and covered with a biofilm) it is likely that microbial activity might be incorporated in the corrosion process.

The corrosion process during anaerobic conditions described in Section 2.3, causes the iron to stay in solution. This condition allows the iron to be transported through the cracks and concrete pore-system before it is precipitated as a corrosion product. This is the case with black rust, since it can be found in voids and cracks within the concrete samples. Black rust is also found underneath or in the rust nodule as reported from the field studies in this work (Fig. 6.3 and Fig. 25). An explanation to the distribution of black rust is the transportation mechanisms of the iron solution, where anodic and cathodic reactions are likely playing an important role. The transportation occurs between low and high potential areas in the concrete. Since black rust is mainly found between the reinforcement and the concrete surface or in the nodule, the iron solution must be transported in an outward direction (i.e. towards the surface) where the iron solution can precipitate. The amount of available oxygen outside the concrete is rather limited since the corrosion process often occurs under water. The rust nodule can then prevent the oxygen from reaching the underlying structure. Anaerobic corrosion can then proceed and continuously leach iron from the reinforcement bar. Severe section loss of the reinforcement is seen in both samples from The Sound (Samples 1 and 2) and the water treatment plant (Sample 3). The transportation of iron may also explain why there is only minor accumulation of corrosion products on the reinforcement. Even though black rust is less expansive than red rust, it is possible that the iron transport additionally contributes to the absence of cracking and spalling of the concrete during anaerobic corrosion. Also, the fact that the iron can stay in solution for a relatively long time, without being exposed to oxygen, makes the transport mechanism of the iron possible.

7.2 Results from SEM and optical microscopy

Interpretations of the analytical results in terms of cement paste deterioration (7.2.1), crack patterns (7.2.2) and corrosion characteristic within the samples (7.2.3) are covered in this section. Subsection 7.2.4 provides a short discussion of the stoichiometry from the SEM analyses. Also, suggestions of corrosion products based on estimated stoichiometry is provided in Subsections 7.2.3 and 7.2.4.

7.2.1 Cement paste deterioration

In general for all the samples, the cement paste was mostly degraded in the concrete cover. Below the reinforcement only minor parts were carbonated or showed discoloration from corrosion products. Since the cement paste alteration was primarily observed in connection to cracks and voids it is hard to specify zonation properties in terms of distance from the surface or reinforcement. Concrete that is submerged, especially in seawater, is often suffering from a sulfate attack (Fagerlund 1992). The sulfate attack is likely to have caused some of the cracks in the cement paste. Formation of ettringite and other expansive chemical compounds in alredy exsisting spaces exert a pressure to the surrounding concrete which cracks. These cracks open up the concrete and makes it more vulnerable for chlorides as well as carbonation.

In the samples of this study, most of the cement paste deterioration could be confined in the upper 15-20 mm of the concrete cover, which also is within the depths of the reinforcement. In Fig. 6.31 carbonated or Ca-leached cement paste is observed below the reinforcemet. However, there can be additional or another causes for corrosion initiation than carbonation. Chlorides are a likely factor, since they can penetrate the concrete in a punctually manner (Tuutti 1982; Fagerlund 1992) and are abundant in both seawater and flocculation agent surrounding the concrete. They are likely to reach the rebar before the carbonation front. Additionally there were increased amounts of chlorides detected in the cement paste (Sample 3; Table A23)

and within the corrosion products (Sample 1; Table A8). There is also an increased amounts of magnesium within the cement paste found in several sites in Sample 3. One explanation is that the cement paste has been Mg-rich from the beginning. Since this sample derives from a water treatment plant there is a possibility that it could be magnesium-rich freshwater that have infiltrated the concrete.

Below the reinforcement there were only minor parts that were carbonated or showed discoloration from corrosion products. In many cases it seems that the degree of breakdown of cement paste follows the extent of corrosion of the iron, at least around the iron bar. Where there was more extensive corrosion, like in sample 2 and 3, the cement paste had also been affected in a wider circumference compared to Sample 1. In Sample 1, the cement paste is rather unaltered within a few millimeters from the rebar and the rebar itself shows only minor signs of corrosion.

A weakened concrete together with section loss of the reinforcement, is considered as a severe damage and shortens the lifetime of the building considerably. Other signs of a changed concrete chemistry are the presence of reaction products, like large crystals of calcium hydroxide (portlandite; $Ca(OH)_2$) and fibrous ettringite ($Ca_6Al_2(SO_4)_3(OH)_{12} \cdot 26H_2O$). Ettringite is probably related to a sulfate attack, however this was not investigated as it is not within the scope of this study. These reaction products are primarily observed in voids and cracks but also in the cement paste (Sample 1). However these are more difficult to see with an optical microscope due to the very fine-grained. From the SEM/EDS analyses there are Ettringite recorded and some possible spots of gypsum ($CaSO_4 \cdot 2H_2O$; Table A2 and Fig. A2).

Results from the EDS analyses of the cement paste indicate that the cement paste is damaged and has experienced a loss of calcium and alkali elements which results in a fragile porous and weakened strength of the concrete around the corrosion affected areas. This can be explained by carbonation, or a Ca-leaching which also lower pH, however this was not measured. Only the cement paste structures can answer for that statement. The relatively large crystals of portlandite indicate that a low pH has dissolved the calcium and then been recrystallized in other sites of higher alkalinity within the concrete. If microorganisms have been involved in the corrosion process, they would presumably account for some of the change in concrete chemistry as well.

7.2.2 Crack generations

Within the thin sections different sets of cracks were observed. These were characterized by different fillings such as corrosion products, reaction minerals, epoxy resin or they were just empty. If comparing the different cracks and categorize them it is possible to discern some generations of crack systems. Cracks that are filled with black or red corrosion products, ettringite, portlandite, or some other reaction mineral, are likely initial. Black rust is a product that precipitates in already existing cracks and voids, and the same goes for ettringite and portlandite. The ettringite is a sign of sulfate attack in the cement paste. This creates cracks that are radiating from rock aggregates and eventually cause loss of adhesion to the aggregate. Such cracks are likely to be filled with ettringite as a final step in the sulfate process (Fig. 6.46A-B)

The initial cracks are either formed during the hardening of the cement paste (i.e. cracks along the rock aggregates) or after hardening but before the corrosion event (i.e. cracks that goes through ballast particles). The latter has had much longer time to form so it is difficult to tell if those cracks are rather old or more recent. An example of those cracks can be seen in Fig. 6.33. Then there are secondary cracks filled with epoxy resin. These could have formed due to expanding forces within the concrete, such as formation of red rust during a later stage in the corrosion process or as a consequence of sulfate attack. Dehydration is another possible explanation for these cracks. Dehydration cracks are generally thin, filled with epoxy resin and generally found close to the surface or around the corroding iron (Fig. 6.46A-B). These have been formed somewhere in-between corrosion breakout and sample preparation. Empty cracks found in the samples are difficult to categorize. There is a possibility that these are either initial cracks which have been trapped within the epoxy resin as air pockets, or artefacts as a consequence of preparation (Fig 6.9). Micro-cracks (a few µm wide) were found in several microdomains during SEM. These are most likely dehydration cracks formed during or after sample preparation. A likely time of formation is during the carbon coating, when the sample was subjected to negative pressure, or possibly in the vacuum chamber of the SEM. The micro-cracks are probably the most recent cracks formed (Fig. 6.16).

7.2.3 Corrosion characteristics

The corrosion products of iron were possible to describe through their physical, and in some extent chemical properties in this study. To further specify chemical properties, like chemical formula, other methods will be needed (Section 7.3). Black rust has in literature been mentioned as a soft and spongy material with a gritty texture (Fatemi et al. 2011; O'Donovan et al. 2013). In this study black rust has been further described based on field studies as well as optical and scanning electron microscopy to try describing the corrosion product. Even though there is no known crystallographic structure to black rust it seems to follow some kind of structure.

Zonal formation in the corrosion products can be interpreted as liesegang structures. They are capable of forming in concrete and mortar according to Rodriguez-Navarro et al. (2002). But since these are only seen in the corrosion products and not the cement paste, this is more likely a sign of cyclic deposition of these corrosion products. Probably it is regulated by some kind of cyclicity in the rust formation. Guilbaud et al. (2013) has shown that the growth of green rusts can occur in repetitive steps of solution and re-adsorption of ions. This can explain the layered structures within the corrosion products. When a nodule from Sample 2 (which had experienced oxidation) was examined, some of its layers in the mixture of red rust were still black and had a metallic luster (Fig. 6.25). These were much harder compared to the porous red rust. Similar layers of black rust have also been detect-

ed within all of the thin sections and also in backscatter images during SEM analysis in some of the microdomains (Fig. 6.28). These microdomains consist mainly of iron. However, there were different shades of grey of the layered corrosion product in the backscatter image as described in Subsection 6.2.3 (Fig. 6.42A-B). These are probably iron oxides or hydroxides of different valences, Fe(II) or Fe(III).

Within Sample 4 pronounced depressions were observed in the steel surface (Fig. 6.48A-C). These are most likely corrosion pits derived from the corrosion process. Pit corrosion is a common phenomenon also in aerated conditions where there can arise an anaerobic microenvironment within the pit (Fig. 2.3; Broomfield 2007). Corrosion products that accumulates at the iron surface will eventually enclose the pit which prevents oxygen from entering. The corrosion products formed within these pits can be black rust as well as other rust species.

Other black or dark colored corrosion products with crystallographic attributes were easy to distinguish by the darkfield reflected light illumination during optical microscopy (Figs. 6.36 and 6.49). These examples cannot be attributed to the black rust description alone but are likely to be other kinds of iron corrosion products. Looking closer to Fig. 6.49 there are at least three layers of corrosion products surrounding the void. The outer dark grey is interpreted as black rust. There can also be a second thin black layer in between the needles and the black rust, which form rounded mounds similar to the shape of goethite. The needle layer growing out from the mounds can be lepidocrocite, which tends to form such crystals. That is also likely regarding the surrounding corrosion products. Then there is a layer of calcium hydroxide (portlandite), barely visible in this light. It can be seen more clearly in crossed polarized light. The innermost layer can only be distinguished from the outermost layer in the darkfield mode. In plain polarized light they look the same. This inner layer has a slightly more green tone in comparison to the black rust, which indicates a different corrosion product. Since this void is in connection with the surface there is a likeliness of external impact of this layer, such as oxidation.

Some of the microdomains in Sample 1 showed rather high (> 22 wt %) amounts of chloride in the EDS analysis (Table A8). These corrosion products seems to be situated on the reinforcement surface. The high amount of chloride are likely reflecting the original distribution within the sample, but may have been effected by the preparation of the sample. The high presence of iron together with chloride can be interpreted as iron chloride ($FeCl_3$) or a hydroxysalt of chloride green rust (GR(Cl^-). However, it is hard to tell whether it is chloride-green rust or not without more specific analytical data from for example Raman spectroscopy or X-ray powder diffraction (XRD). Refait et al. (1998) has shown that GR(Cl^-) can form through aerial oxidation of ferrous hydroxide and direct precipitation from dissolved ferrous and ferric salts. The results in this study imply that green rust has occurred as a corrosion product within the samples. However, this have not been proven and is beyond the scope of this study. In order to confirm this, more material analyses are needed.

7.2.4 Stoichiometry

It was not possible to calculate accurate stoichiometry of the corrosion products from the EDS analysis. Since the corrosion products of iron mainly are oxides and oxyhydroxides it is impossible to distinguish the corrosion species from each other since the SEM/EDS cannot identify the valences of iron (e.g. Fe(II) and Fe(III)). Neither can it detect hydrogen which makes it more difficult to identify corrosion species such as iron hydroxides. Therefore, the stoichiometry could only be estimated for some of the reaction products in the cement paste. Ettringite ($Ca_6Al_2(SO_4)_3(OH)_{12} \cdot 26H_2O$) and gypsum ($CaSO_4 \cdot 2H_2O$) could be identified through spot analyses. For the corrosion products iron was most prevalent, sometimes together with sulfur or chloride. These could indicate the presence of for example iron sulfide (FeS) and iron chloride ($FeCl_3$) or possibly chloride green rust (GR(Cl^-)) as suggested above (Subsection 7.2.3). However, it is not proven that the amount of chlorine measured is present in form of salts or Fe-complexes. The latter cannot be ruled out since Fe has a high affinity to form complexes. They could also be impurities on the iron coming from external sources such as seawater or flocculants.

7.3 Methodology

Samples containing unstable corrosion products, like the ones in this study, need special handling in order to stay unchanged before eventual analyses. However, the sample treatment may be dependent of what kind of analysis is to be done. For example, samples that will be analyzed in SEM need to be dehydrated before they are inserted in the vacuum chamber. This procedure will most likely oxidize the original corrosion product into a more stable phase. Therefore, SEM may be more suitable for studying structures rather than composition. Świetlik et al. (2012) concluded that a more true composition was derived from hydrated samples compared to dehydrated ones. Diffraction methods are preferred when examining the composition of the corrosion products, even though the result may not be fully reliable due to the heterogeneous nature of the corrosion product. Hence it is more advantageous to study corrosion products like green and black rust that are derived from a laboratory environment. Compared to field samples the outcome will be more predictable and give a lower uncertainty to the results. Additionally, correct handling of the reactive samples is favored in a controlled environment (Świetlik et al. 2012; Silva 2013).

From the experience of this work, a well-structured sample treatment plan is recommended, before the sampling occasion. Since samples used in this study are field samples the sample treatment had to be restricted to only necessary contact with the atmosphere. It was desirable to largely maintain an oxygen deficient environment for the corrosion products. This has been difficult during the preparation stage since resources and experiences were limited. Storage and treatment method can be improved in future studies. Suggestions are presented in Subsection 7.4.1. However, the sample treatment in this study was considered to be good enough for its purpose.

The preparation of the examined samples was a

rather time consuming process, which does not go along with reactive and/or sensitive samples. This process should preferably be quick and structured. Alternatively special equipment are needed to keep the samples in a stable condition. Previous studies have kept the samples in anoxic chambers to make as small impact as possible to the sample before analyses (Miot et al. 2014; Yin et al. 2017). The sample preparation in this study seemed to have made a rather insignificant impact to the samples since it was still possible to analyze the black corrosion products. However, it is hard to know if there have been earlier corrosion species (e.g. green rust) which have oxidized into black rust before the analyses.

During sample preparation the test with acetone as a drying agent quickly formed red rust on the reinforcement. The acetone resulted in a more intense oxidation process compared to aerial oxidation. The method of drying the sample parts with acetone was an attempt of working quickly with the samples. Świetlik et al. (2012) successfully used acetone for drying the samples prior to SEM analysis. However, those were not concrete samples but rather smaller pieces of tubercles. That method might be successful with smaller samples. Porous concrete takes time to dry since the water is easily trapped in the pore system through capillary forces. Acetone is more volatile and forces its way into the pore system and evaporates easily. In that moment a lot of oxygen can enter the pore system. This might have accelerated the oxidation process. Another reason can be the fact that acetone is a good solvent, and in many cases used to remove grease and dirt particles from iron and steel. The solvent removes the corrosion product on a corroded metal surface as well as the passive film on uncorroded metal surfaces. This will expose the surface to oxygen and can initiate corrosion.

7.4 Future studies

Examples of further studies within the issue of black corrosion are suggested in this section. Both a revised methodology, needed to increase accuracy in the analyses, and the need of more studies of the relation between different corrosion products are requested. This is found in Subsections 7.4.1 and 7.4.2 respectively.

7.4.1 Methodology

If this study will be repeated it is recommended to adjust the methodology, especially the sampling, sample storage, and sample preparation. As already mentioned, it is important to keep the samples as unchanged as possible before analysis. However, it is also dependent on the analytical methods that are planned. The sample storage should preferably be in a wet oxygen limited environment. Vacuum packing the samples directly in field or shortly after sampling might be an idea. Samples that should be stored for some time should be packed with boiled, cooled water or water from the sampling location.

It would be beneficial to have separate samples for studying the concrete degradation and corrosion products since these need different analytical methods. The concrete needs larger sample pieces and is not that sensitive to aerial exposure. The corrosion product samples on the other hand can be smaller and do not necessarily need to contain much of the concrete.

An additional idea can be to check the cement paste for changes in the pH value depending on its degree of alteration. Carbonation in the cement paste can be tested with a phenolphthalein or thymol blue indicator. Otherwise it can be difficult to notice change in the alkalinity if there is an ongoing corrosion process.

In order to find out more about the chemistry of black rust, more investigations are needed. Methods such as XRD or Raman spectroscopy can be suitable for this purpose. With Mössbauer spectroscopy it is possible to study the valence state of iron (i.e. Fe(II)-(III); Dyar 2018) and it is commonly used for detecting green rust species (Refait et al. 2006; Miot et al. 2014; Usher et al. 2014; Yin et al. 2017). These methods would give crystallographic info about the corrosion products but require rather homogeneous samples in order to be reliable (Świetlik et al. 2012), which can be a challenge for these kind of samples. But then again it is an advantage that only a small part of the product is needed and it can be analyzed in wet condition. Hence the results will probably show the unaltered product.

7.4.2 Relation between black, red and green rust

An interesting research area within this field would be the corrosion process of black rust in comparison to red rust (i.e. anaerobic vs aerobic corrosion). Black rust is sometimes observed to be faster than the red rust forming corrosion process in terms of material degradation. It can be important to understand these differences in order to assess the durability of concrete structures. The difference could be many, for example reaction rates, chemical conditions, starting position of the reactions, conditions needed for a reaction to take place etc. One suggestion would be to study the interference of microorganisms. Their metabolic impact might speed up the corrosion process, a theory that can be deduced from the experimental results by Miot et al. (2014).

The corrosion process of black rust in reinforced concrete is linked to the green rust through physical and maybe biotic factors. However, further studies are needed about the relations between black and green rusts, and the influence of microorganisms on those phases. This would increase the understanding of the phenomenon of black corrosion and fill the knowledge gap currently existing in the scientific community about black rust (e.g. how and why it is formed).

8 Conclusions

The present study contributes to the understanding about the corrosive nature of black rust by describing the phenomenon of black corrosion within reinforced concrete. Literature about corrosion processes and corrosion products have been reviewed and field samples of corroded reinforced concrete have been analyzed. The following could be concluded:

- The anaerobic corrosion process affects the reinforcement bars in a manner that leads to substantial

material loss due to dissolution of the iron.

- The dissolved iron material seems to be transported towards the concrete surface, where it extrudes in form of soft and layered rust nodules of black and yellow color.
- The initiation of black corrosion seems to be similar to the red rust corrosion. Since the corrosion process involves pit corrosion behavior the initiation might be primarily connected to chloride initiated corrosion.
- The corrosion process changes the joint chemistry and phase composition of the adjacent concrete. All samples that were examined by the SEM/EDS analyses (Samples 1, 2, and 3) show a changed composition in the cement paste, with leaching of elements (primarily Ca, Al and Si) as a major consequence.
- Due to seawater exposure some of the cement minerals recrystallized and formed in cracks, voids as well as in the cement paste. These minerals are: ettringite, portlandite and gypsum.
- Black rust is observed as a dark, soft and mud-like substance that fills porous areas such as cracks and voids in the concrete without having a consistent internal crystallographic structure. Despite this, black rust precipitates in a cyclic pattern with alternating layers made of ferric and ferrous iron oxides and – hydroxides.
- Darkfield reflected light illumination has been useful when studying corrosion products using optical microscopy. Different corrosion products could easily be distinguished with the help of this method.
- The sampling method and preparation has been sufficient for the aim of this work, but has to be improved when doing further analysis. A well-structured plan for sampling and preparation is required for exerting minimal impact to the samples. Samples have to be processed and analyzed quickly. If the samples are to be stored for a longer period of time the samples should be in an anaerobic and moist to wet condition.
- In order to identify the exact mineralogy of black rust in terms of stoichiometry and distinction between ferric and ferrous components, diffraction analysis such as XRD or Raman Spectroscopy are needed.

Black and green rust can be found in the same corrosive environment during different stages of the corrosion process. An enhanced characterization of black rust is desired, but requires further studies about the relationship between these phases as well as the influence of microbial corrosion. Additionally, no signs of microbial activity were found in the samples. A closer investigation was however not within the scope of this work.

9 Acknowledgements

Much appreciation is given to my supervisors: Charlotte Möller (Department of Geology, LU) for encouraging guidance and initiating the idea of this project; Birgit Fredrich and Jan Erik Lindqvist (RISE CBI) for supporting me, especially during microscopy, analyses and for providing useful inputs in the writing process. The interest and assistance from the other employees of RISE CBI were appreciated and a special recognition is given to Daniel Andersson and Adam Persson for letting me participate during the field sampling. Further I would like to acknowledge Anders Lindskog for support with sample preparation, Åsa Wallin for help in the SEM-laboratory, Carl Alwmark and Leif Johansson for guidance and support with SEM analyses. At last I thank my family and friends for their support during this project.

10 References

Alonso, M. C. & Sanchez, M., 2009: Analysis of the variability of chloride threshold values in the literature. Materials and Corrosion 60, 631–637. doi: 10.1002/maco.200905296.

Angst, U., Elsener, B., Larsen, C. K. & Vennesland, Ø., 2009: Critical chloride content in reinforced concrete — A review. Cement and Concrete Research 39, 1122–1138. doi: 10.1016/j.cemconres.2009.08.006.

Badan, B., Magrini, M. & Ramous, E., 1991: A study of the microbiological-corrosion products of steel and cast iron pipes in fresh water. Journal of materials science 26, 1951–1954.

Bernal, J. D., Dasgupta, D. R. & Mackay, A. L., 1959: The Oxides and Hydroxides of Iron and Their Structural Inter-Relationships. Clay Minerals 4, 15–30. doi: 10.1180/claymin.1959.004.21.02.

Boubitsas, D., 2015: Chloride transport and chloride thresholdvalues - Studies on concretes and motars with Portland cement and limestone blendes cement. Ph. D. thesis, Lund, Sweden, Faculty of Engineering, Division of Building materials, Lund University. 86 pp.

Broomfield, J. P., 2007: Corrosion of steel in concrete: understanding, investigation and repair. Taylor & Francis, London ; New York. 277 pp.

Burström, P. G., 2007: Byggnadsmaterial: uppbyggnad, tillverkning och egenskaper. Studentlitteratur, Lund. 562 pp.

Duan, J., Wu, S., Zhang, X., Huang, G., Du, M. & Hou, B., 2008: Corrosion of carbon steel influenced by anaerobic biofilm in natural seawater. Electrochimica Acta 54, 22–28. doi: 10.1016/j.electacta.2008.04.085.

Duffó, G. S., Reinoso, M., Ramos, C. P. & Farina, S. B., 2012: Characterization of steel rebars embedded in a 70-year old concrete structure. Cement and Concrete Research 42, 111–117. doi: 10.1016/j.cemconres.2011.08.003.

Duffó, G. S., Morris, W., Raspini, I. & Saragovi, C., 2004: A study of steel rebars embedded in concrete during 65 years. Corrosion Science 46, 2143–2157. doi: 10.1016/j.corsci.2004.01.006.

Dyar, M. D., 2018: Mössbauer Spectroscopy. Retrieved 20 December 2018, from https://serc.carleton.edu/research_education/geochemsheets/techniques/mossbauer.html.

Egerton, R. F., 2008: Physical principles of electron microscopy: an introduction to TEM, SEM, and AEM. Springer, New York, NY. 202 pp.

Fagerlund, G., 1992: Betongkonstruktioners beständighet: en översikt. Cementa, Danderyd. 101 pp.

Fatemi, H., Moore, M. & Khatri, R., 2011: Importance of detection of black rust formation. Austroads 8th Bridge Conference: proceedings, 31 October - 5 November 2000, Sydney, Australia: sustainable bridges: the thread of society, 98–110. Austroads, Sydney, New South Wales, Australia.

Génin, J.-M. R., Abdelmoula, M., Ruby, C. & Upadhyay, C., 2006: Speciation of iron; characterisation and structure of green rusts and FeII–III oxyhydroxycarbonate fougerite. Comptes Rendus Geoscience 338, 402–419. doi: 10.1016/j.crte.2006.04.005.

Gestsdóttir, E. & Guðmundsson, T., 2012: Bond Behaviour of Naturally Corroded Reinforcement in Concrete Structures. Master's thesis, Göteborg, Sweden, Chalmers University of Technology. 76 pp.

GSSI, 2017: Concrete Handbook. Handbook, MN72-367 Rev H, Geophysical Survey Systems, Inc. (GSSI), New Hampshire, USA. 39 pp.

Guilbaud, R., White, M. L. & Poulton, S. W., 2013: Surface charge and growth of sulphate and carbonate green rust in aqueous media. Geochimica et Cosmochimica Acta 108, 141–153. doi: 10.1016/j.gca.2013.01.017.

Jackson, M. D., Mulcahy, S. R., Chen, H., Li, Y., Li, Q., Cappelletti, P. & Wenk, H.-R., 2017: Phillipsite and Al-tobermorite mineral cements produced through low-temperature water-rock reactions in Roman marine concrete. American Mineralogist 102, 1435–1450. doi: 10.2138/am-2017-5993CCBY.

Jacobsson, M., 2016: Betongskador i vattenverk [Concrete damages in water plants]. Rapport, 2016–18, Svenskt Vatten AB, Bromma, Sweden. 60 pp.

King, F., 2008: Corrosion of carbon steel under anaerobic conditions in a repository for SF and HLW in Opalinus Clay. NAGRA, 44.

Lea, F. M. & Hewlett, P. C., 2008: Lea's chemistry of cement and concrete. Elservier Butterworth-Heinemann, Oxford; MA. 1057 pp.

L'Hostis, V., Neff, D., Bellot-Gurlet, L. & Dillmann, P., 2009: Characterization of long-term corrosion of rebars embedded in concretes sampled on French historical buildings aged from 50 to 80 years. Materials and Corrosion 60, 93–98. doi: 10.1002/maco.200805019.

Ljungkrantz, C., Möller, G., Petersons, N. & Svensk byggtjänst, 1997: Betonghandbok. Svensk byggtjänst, Solna. 1127 pp.

McCafferty, E., 2010: Introduction to corrosion science. Springer, New York. 575 pp.

McGill, I. R., McEnaney, B. & Smith, D. C., 1976: Crystal structure of green rust formed by corrosion of cast iron. Nature 259, 200–201. doi: 10.1038/259200a0.

Miot, J., Li, J., Benzerara, K., Sougrati, M. T., Ona-Nguema, G., Bernard, S., Jumas, J.-C. & Guyot, F., 2014: Formation of single domain magnetite by green rust oxidation promoted by microbial anaerobic nitrate-dependent iron oxidation. Geochimica et Cosmochimica Acta 139, 327–343. doi: 10.1016/j.gca.2014.04.047.

O'Donovan, R., O'Rourke, B. D., Ruane, K. D. & Murphy, J. J., 2013: Anaerobic Corrosion of Reinforcement. Key Engineering Materials 569–570, 1124–1131. doi: 10.4028/www.scientific.net/KEM.569-570.1124.

Ona-Nguema, G., Abdelmoula, M., Jorand, F., Benali, O., Géhin, A., Block, J.-C. & Génin, J.-M. R., 2002a: Microbial Reduction of Lepidocrocite γ-FeOOH by Shewanella putrefaciens; The Formation of Green Rust. Hyperfine Interactions 139–140, 231–237. doi: 10.1023/A:1021235425553.

Ona-Nguema, G., Abdelmoula, M., Jorand, F., Benali, O., Block, J.-C. & Génin, J.-M. R., 2002b: Iron(II,III) Hydroxycarbonate Green Rust Formation and Stabilization from Lepidocrocite Bioreduction. Environmental Science & Technology 36, 16–20. doi: 10.1021/es0020456.

Pei, X., Noël, M., Green, M., Fam, A. & Shier, G., 2017: Cementitious coatings for improved corrosion resistance of steel reinforcement. Surface and Coatings Technology 315, 188–195. doi: 10.1016/j.surfcoat.2017.02.036.

Refait, P., Abdelmoula, M., Génin, J.-M. R. & Sabot, R., 2006: Green rusts in electrochemical and microbially influenced corrosion of steel. Comptes Rendus Geoscience 338, 476–487. doi: 10.1016/j.crte.2006.04.012.

Refait, P., Nguyen, D. D., Jeannin, M., Sable, S., Langumier, M. & Sabot, R., 2011: Electrochemical formation of green rusts in deaerated seawater-like solutions. Electrochimica Acta 56, 6481–6488. doi: 10.1016/j.electacta.2011.04.123.

Refait, P., Abdelmoula, M. & GÉnin, J.-M. R., 1998: Mechanisms of formation and structure of green rust one in aqueous corrosion of iron in the presence of chloride ions. Corrosion Science 40, 1547–1560. doi: 10.1016/S0010-938X(98)00066-3.

Rémazeilles, C., Neff, D., Kergourlay, F., Foy, E., Conforto, E., Guilminot, E., Reguer, S., Refait, P. & Dillmann, P., 2009: Mechanisms of long-term anaerobic corrosion of iron archaeological artefacts in seawater. Corrosion Science 51, 2932–2941. doi: 10.1016/j.corsci.2009.08.022.

Rodriguez-Navarro, C., Cazalla, O., Elert, K. & Sebastian, E., 2002: Liesegang pattern development in carbonating traditional lime mortars. Proceedings of the Royal Society A: Mathematical, Physical and Engineering Sciences, 458, 2261–2273. Royal Society, London, United Kingdom. doi: 10.1098/rspa.2002.0975.

Silva, N., 2013: Chloride induced corrosion of reinforcement steel in concrete - Threshold values and ion distributions at the concrete-steel interface. Ph. D. thesis, Göteborg, Sweden, Department of Civil and Environmental Engineering, Division of Building Technology, Chalmers University of Technology. 153 pp.

Smart, N. R. & Adams, R., 2006: Natural analogues for expansion due to the anaerobic corrosion of ferrous materials. Technical Report, TR-06-44, SKB, Stockholm, Sweden. 37 pp.

Świetlik, J., Raczyk-Stanisławiak, U., Piszora, P. & Nawrocki, J., 2012: Corrosion in drinking water pipes: The importance of green rusts. Water Research 46, 1–10. doi: 10.1016/j.watres.2011.10.006.

Tuutti, K., 1982: Corrosion of steel in concrete. Ph. D. thesis (monograph), Lund, Sweden, Lund University. 468 pp.

Usher, K. M., Kaksonen, A. H. & MacLeod, I. D., 2014: Marine rust tubercles harbour iron corroding archaea and sulphate reducing bacteria. Corrosion Science 83, 189–197. doi: 10.1016/j.corsci.2014.02.014.

Vera, R., Villarroel, M., Carvajal, A. M., Vera, E. & Ortiz, C., 2009: Corrosion products of reinforcement in concrete in marine and industrial environments. Materials Chemistry and Physics 114, 467–474. doi: 10.1016/j.matchemphys.2008.09.063.

Walsh, M. T., 2015: Corrosion of Steel in Submerged Concrete Structures. Ph. D. thesis, Florida, United States, University of South Florida. 139 pp.

Wong, H. S., Zhao, Y. X., Karimi, A. R., Buenfeld, N. R. & Jin, W. L., 2010: On the penetration of corrosion products from reinforcing steel into concrete due to chloride-induced corrosion. Corrosion Science 52, 2469–2480. doi: 10.1016/j.corsci.2010.03.025.

Yin, W., Huang, L., Pedersen, E. B., Frandsen, C. & Hansen, H. C. B., 2017: Glycine buffered synthesis of layered iron(II)-iron(III) hydroxides (green rusts). Journal of Colloid and Interface Science 497, 429–438. doi: 10.1016/j.jcis.2016.11.076.

Zegeye, A., Abdelmoula, M., Usman, M., Hanna, K. & Ruby, C., 2011: In situ monitoring of lepidocrocite bioreduction and magnetite formation by reflection Mössbauer spectroscopy. American Mineralogist 96, 1410–1413. doi: 10.2138/am.2011.3794.

Zegeye, A., Bonneville, S., Benning, L. G., Sturm, A., Fowle, D. A., Jones, C., Canfield, D. E., Ruby, C., MacLean, L. C., Nomosatryo, S., Crowe, S. A. & Poulton, S. W., 2012: Green rust formation controls nutrient availability in a ferruginous water column. Geology 40, 599–602. doi: 10.1130/G32959.1.

Zhou, Y., Gencturk, B., Willam, K. & Attar, A., 2015: Carbonation-Induced and Chloride-Induced Corrosion in Reinforced Concrete Structures. Journal of Materials in Civil Engineering 27, 04014245. doi: 10.1061/(ASCE)MT.1943-5533.0001209.

Appendix

The purpose of the appendix is to show the remaining analysis material from the scanning electron microscopy. Analyzed slices are listed in order 1.1, 1.2, 2, and 3, representing Samples 1, 2 and 3. EDS tables, BSE images, element maps, and graphs compiled from the EDS analyses are shown in this appendix.

Table. A1. EDS analysis of Site 1, Slice 1.1.

Spectrum Label	O	Na	Mg	Al	Si	P	S	Cl	K	Ca	Ti	Cr	Fe	Zn	Total
Slice 1.1, Site 1, Zone 1															
Spectrum 200	29,70	3,17	0,16	0,21	0,64	0,03	7,18	0,31	0,11	0,06	0,00	0,09	58,34	0,00	100,00
Spectrum 201	31,83	3,29	0,05	0,25	1,22	0,06	8,49	0,12	0,24	4,98	0,10	0,06	49,33	0,00	100,00
Spectrum 202	28,21	1,86	0,07	0,03	1,36	0,02	5,26	0,18	0,05	0,02	0,00	0,03	62,64	0,27	100,00
Spectrum 203	31,07	2,49	0,29	0,66	2,38	0,03	7,15	0,16	0,32	0,06	0,03	0,00	55,24	0,13	100,00
Spectrum 204	30,89	1,47	0,04	0,04	0,25	0,07	8,82	0,14	0,06	0,10	0,03	0,06	58,03	0,00	100,00
Slice 1.1, Site 1, Zone 2															
Spectrum 205	25,05	0,55	0,08	0,06	0,51	0,07	2,44	0,08	0,00	0,22	0,04	0,03	70,64	0,22	100,00
Spectrum 206	22,74	0,15	0,00	0,10	0,39	0,00	0,16	0,01	0,02	0,08	0,01	0,02	76,27	0,05	100,00
Spectrum 207	28,75	2,66	0,01	0,07	0,51	0,00	6,39	0,27	0,03	0,08	0,10	0,00	61,14	0,00	100,00
Spectrum 208	29,23	2,72	0,00	0,29	1,59	0,05	5,97	0,05	0,06	0,01	0,00	0,00	60,04	0,00	100,00
Spectrum 209	25,09	1,58	0,15	0,08	0,37	0,04	2,53	0,03	0,02	0,03	0,02	0,04	70,03	0,00	100,00
Spectrum 210	25,64	1,43	0,20	0,07	0,26	0,09	3,20	0,16	0,09	0,08	0,00	0,00	68,63	0,15	100,00
Spectrum 211	25,85	1,38	0,17	0,00	0,46	0,10	3,29	0,09	0,00	0,08	0,00	0,03	68,48	0,05	100,00
Spectrum 212	26,12	1,76	0,11	0,00	0,43	0,12	3,60	0,13	0,09	0,09	0,00	0,04	67,34	0,17	100,00
Slice 1.1, Site 1, Zone 3															
Spectrum 214	27,28	0,87	0,11	0,36	1,10	0,10	4,21	0,08	0,03	0,28	0,00	0,00	65,27	0,30	100,00
Spectrum 215	25,29	1,02	0,02	0,10	0,28	0,09	2,83	0,04	0,02	0,07	0,03	0,00	70,18	0,03	100,00
Spectrum 216	29,25	1,35	0,05	0,04	0,29	0,04	7,07	0,13	0,06	0,00	0,10	0,06	61,56	0,00	100,00
Spectrum 217	27,51	1,98	0,18	0,22	0,40	0,12	4,96	0,22	0,06	0,12	0,02	0,09	64,13	0,00	100,00
Spectrum 218	29,02	2,78	0,15	0,04	0,21	0,08	6,75	0,20	0,01	0,05	0,13	0,05	60,55	0,00	100,00
Spectrum 221	29,94	1,44	0,22	0,02	0,19	0,24	7,70	0,10	0,10	0,02	0,00	0,00	60,03	0,00	100,00
Spectrum 222	28,77	1,77	0,07	0,05	0,14	0,21	6,54	0,18	0,08	0,14	0,04	0,00	61,87	0,14	100,00
Spectrum 223	27,68	0,17	0,33	0,08	0,21	0,07	5,62	1,08	0,06	0,42	0,00	0,00	64,29	0,00	100,00
Spectrum 226	25,87	0,87	0,09	0,01	0,23	0,11	3,49	0,13	0,00	0,00	0,12	0,07	69,02	0,00	100,00
Spectrum 227	26,95	1,06	0,10	0,00	0,29	0,00	4,68	0,13	0,00	0,08	0,09	0,00	66,61	0,00	100,00
Spectrum 228	27,04	1,67	0,06	0,00	0,11	0,00	4,94	0,15	0,19	0,00	0,00	0,00	65,86	0,00	100,00
Slice 1.1, Site 1, Zone 4															
Spectrum 219	23,48	0,29	0,16	0,02	0,61	0,00	0,66	0,03	0,01	1,46	0,00	0,00	73,29	0,00	100,00
Spectrum 220	24,00	0,00	0,00	0,00	0,33	0,00	1,60	0,06	0,08	0,23	0,01	0,00	73,63	0,05	100,00
Spectrum 225	23,86	0,36	0,15	0,00	0,08	0,00	1,44	0,02	0,12	1,25	0,05	0,11	72,57	0,00	100,00

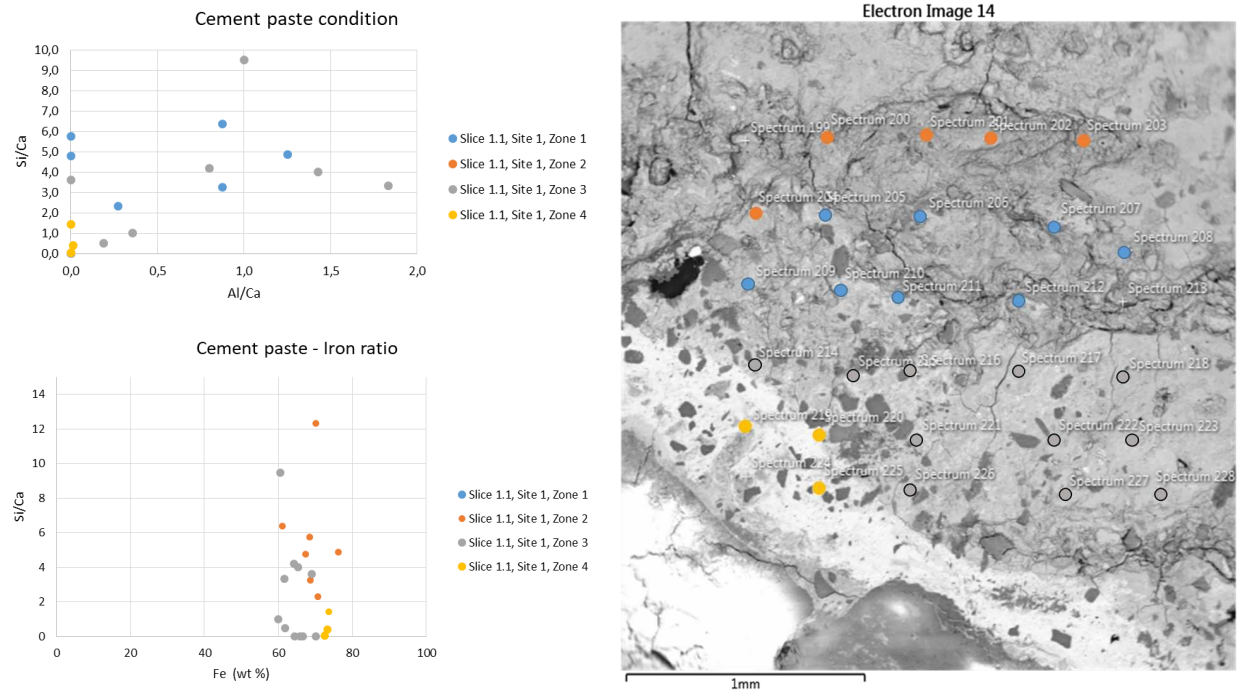

Fig. A1. Graphs and BSE image of Site 1, Slice 1.1.

Table A2. EDS analysis of Site 2, Slice 1.1

Spectrum Label	O	Na	Mg	Al	Si	P	S	Cl	K	Ca	Ti	Cr	Fe	Zn	Total
Slice 1.1, Site 1, Zone 1		**S-rich (Ettringite)**													
Spectrum 229	41,11	0,04	0,00	1,70	7,90	0,03	10,30	0,63	0,02	36,87	0,00	0,00	1,40	0,00	100,00
Spectrum 230	41,48	0,05	0,00	0,72	8,72	0,06	10,47	0,31	0,03	37,13	0,04	0,00	0,99	0,00	100,00
Spectrum 231	41,16	0,00	0,01	1,46	8,41	0,07	9,97	0,35	0,19	37,39	0,00	0,06	0,75	0,19	100,00
Spectrum 232	41,27	0,06	0,09	0,95	8,45	0,00	10,52	0,53	0,00	35,47	0,05	0,13	2,47	0,01	100,00
Slice 1.1, Site 1, Zone 2		**S-poor**													
Spectrum 233	38,40	0,23	0,32	0,73	16,34	0,05	1,71	0,66	0,00	38,32	0,00	0,00	3,01	0,21	100,00
Spectrum 234	33,38	0,00	0,84	0,86	8,23	0,03	1,17	2,66	0,00	50,87	0,11	0,00	1,82	0,04	100,00
Spectrum 235	42,70	0,40	3,02	5,20	18,20	0,01	3,46	1,75	0,08	24,89	0,00	0,00	0,09	0,19	100,00
Spectrum 236	39,05	0,37	0,59	1,79	15,77	0,12	2,39	1,05	0,05	36,20	0,07	0,00	2,54	0,01	100,00

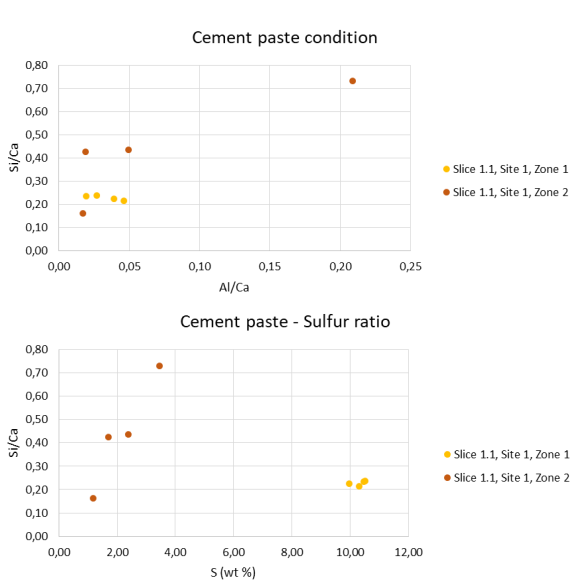

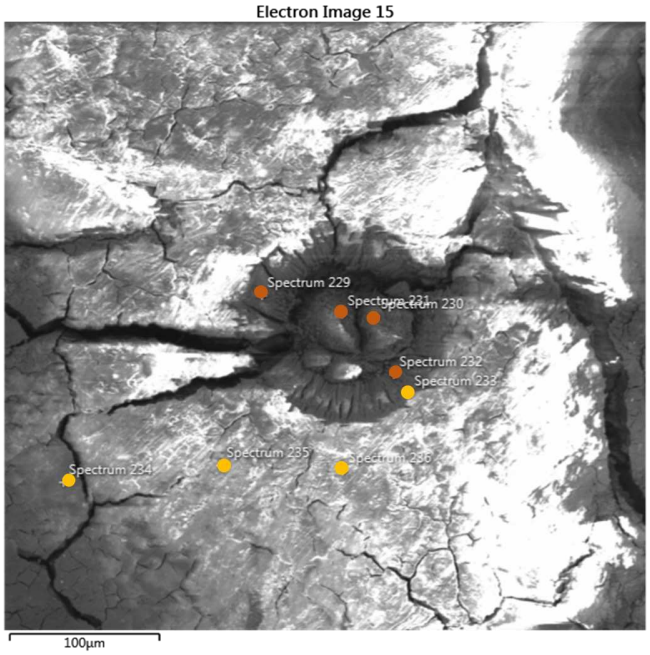

Fig. A2. Graphs and BSE image of Site 2, Slice 1.1.

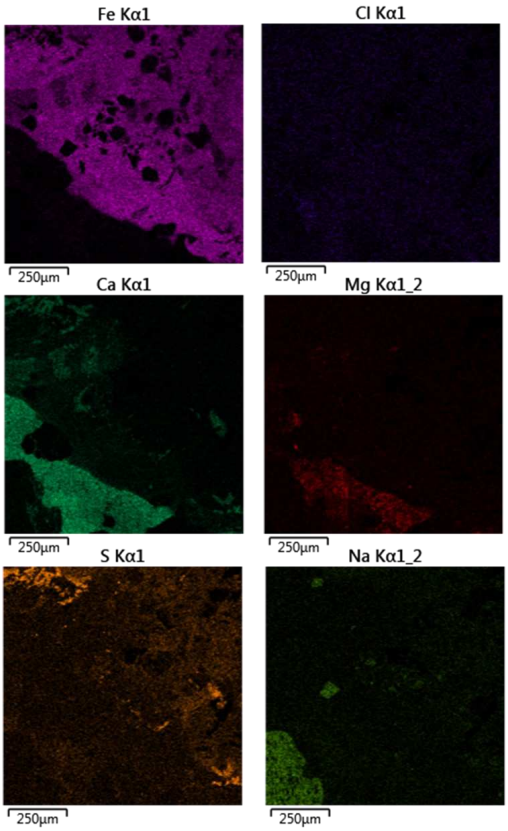

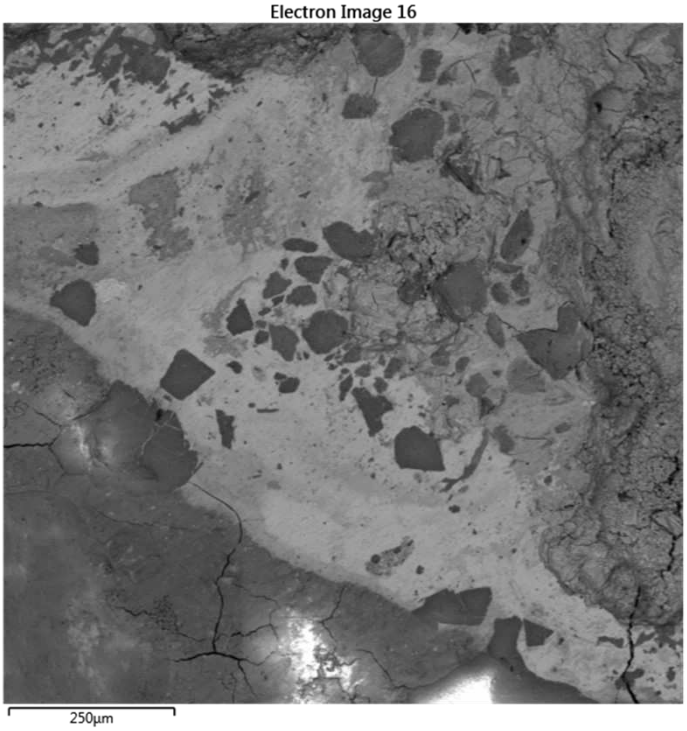

Fig. A3. BSE image and element maps of Site 3, Slice1.1.

Table A3. EDS analysis of Site 4, Slice 1.1

Spectrum Label	O	Na	Mg	Al	Si	P	S	Cl	K	Ca	Ti	Cr	Fe	Zn	Total
Slice 1.1, Site 4, Zone 1															
Spectrum 237	32,82	5,12	0,30	0,05	3,72	0,27	8,16	0,75	0,17	0,09	0,00	0,11	48,43	0,00	100,00
Spectrum 238	38,02	6,89	0,25	0,08	7,57	0,44	10,75	0,75	0,28	0,00	0,00	0,22	34,59	0,17	100,00
Slice 1.1, Site 4, Zone 2															
Spectrum 239	28,89	4,03	0,08	0,15	1,09	0,08	6,08	0,81	0,10	0,01	0,08	0,00	58,58	0,03	100,00
Spectrum 240	31,16	3,08	0,00	0,22	2,75	0,13	7,30	0,70	0,21	0,12	0,00	0,05	54,29	0,00	100,00
Spectrum 241	31,58	1,56	0,07	0,00	3,11	0,55	7,29	0,74	0,22	0,23	0,00	0,20	54,18	0,26	100,00
Spectrum 242	30,60	3,83	0,05	0,16	1,47	0,16	7,49	0,46	0,12	0,06	0,07	0,00	55,40	0,13	100,00
Spectrum 243	31,17	2,93	0,26	0,03	3,14	0,18	6,97	0,72	0,06	0,36	0,03	0,14	54,02	0,00	100,00
Spectrum 246	31,26	4,64	0,05	0,16	2,80	0,23	7,24	0,84	0,26	0,19	0,05	0,00	52,27	0,00	100,00
Slice 1.1, Site 4, Zone 3															
Spectrum 245	46,78	0,84	0,08	0,05	13,46	0,07	15,06	0,14	0,02	14,95	0,03	0,00	8,36	0,17	100,00
Spectrum 248	47,42	0,67	0,01	0,00	0,04	0,05	24,15	0,00	0,00	26,47	0,00	0,05	1,12	0,00	100,00
Slice 1.1, Site 4, Zone 4															
Spectrum 252	31,07	0,12	0,01	0,09	9,32	0,54	2,21	0,34	0,01	1,05	0,00	0,32	54,91	0,00	100,00
Spectrum 253	23,22	0,24	0,01	0,07	0,48	0,46	0,77	2,34	0,03	0,13	0,00	0,13	72,13	0,00	100,00

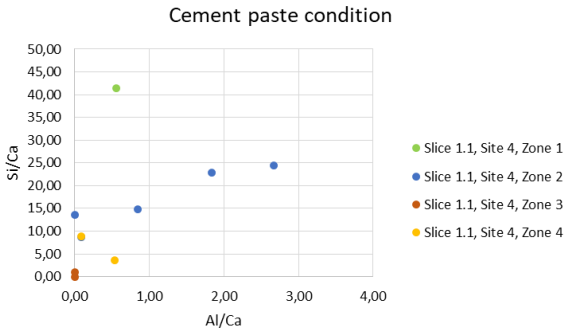

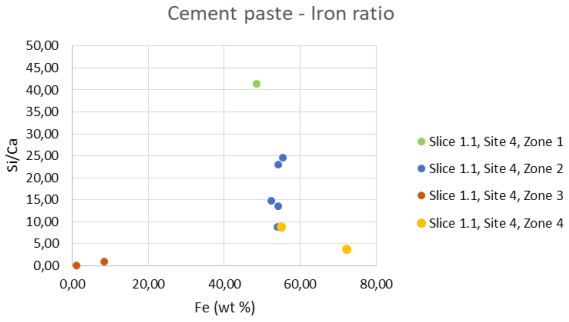

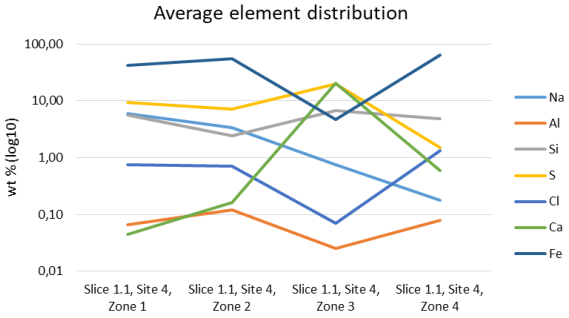

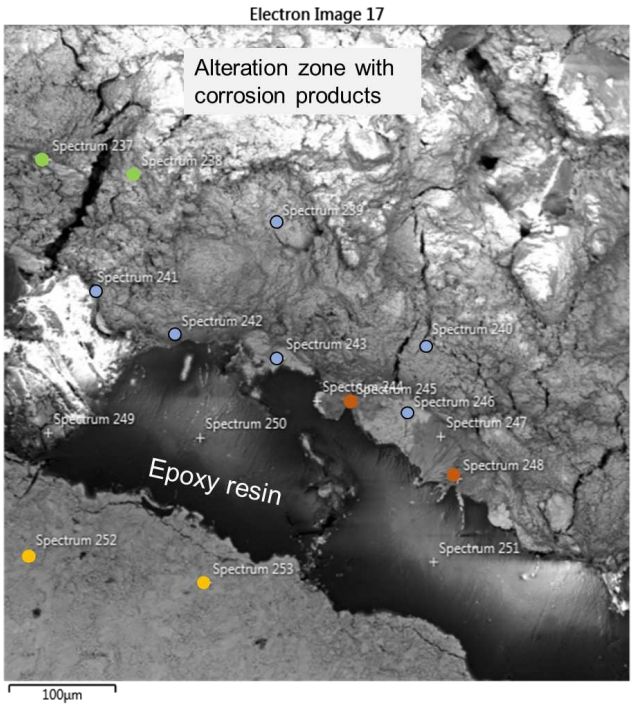

Fig. A4. Graphs and BSE image of Site 4, Slice 1.1.

Table A4. EDS analysis of Site 5, Slice 1.1

Spectrum Label	O	Na	Mg	Al	Si	P	S	Cl	K	Ca	Ti	Cr	Fe	Zn	Total
Slice 1.1, Site 5, Zone 1															
Spectrum 254	25,13	0,00	0,00	0,11	0,50	0,45	2,94	3,03	0,00	0,06	0,03	0,13	67,62	0,00	100,00
Spectrum 255	28,61	0,00	0,16	0,14	1,47	0,05	5,61	0,66	0,00	0,09	0,00	0,55	62,65	0,00	100,00
Spectrum 256	25,25	0,00	0,06	0,00	1,55	0,00	2,21	0,69	0,05	0,00	0,00	0,14	69,60	0,46	100,00
Spectrum 257	24,92	0,00	0,00	0,15	1,14	0,08	1,99	0,73	0,04	0,00	0,00	0,37	70,58	0,00	100,00
Spectrum 259	26,86	0,00	0,08	0,10	0,56	0,01	4,65	1,27	0,03	0,00	0,00	0,46	65,99	0,00	100,00
Spectrum 260	31,44	0,00	0,19	0,37	4,02	0,14	6,90	1,92	0,06	0,04	0,06	0,67	54,20	0,00	100,00
Slice 1.1, Site 5, Zone 2															
Spectrum 258	23,43	0,00	0,00	0,03	0,44	0,00	1,14	1,07	0,09	0,04	0,00	0,21	73,55	0,00	100,00
Spectrum 261	23,42	0,05	0,00	0,02	0,16	0,10	1,06	0,32	0,00	0,27	0,00	0,12	74,09	0,39	100,00
Spectrum 262	23,95	0,12	0,02	0,13	0,40	0,20	1,24	0,30	0,00	0,09	0,00	0,56	72,99	0,00	100,00
Spectrum 263	25,02	0,00	0,00	0,13	0,49	0,14	2,75	1,81	0,00	0,02	0,02	0,51	69,11	0,00	100,00

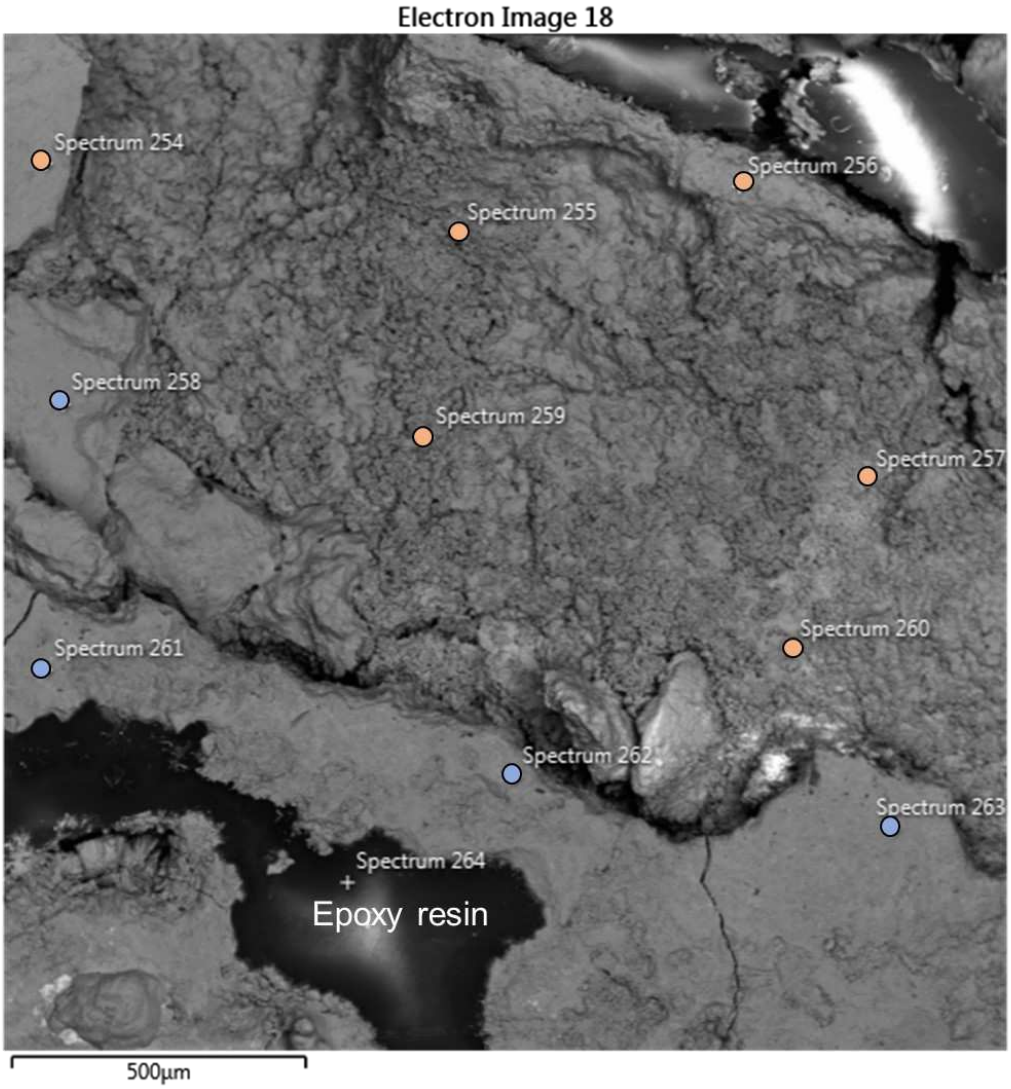

Fig. A5. BSE image of Site 5, Slice 1.1.

Table A5. EDS analysis of Site 6, Slice 1.1

Spectrum Label	O	Na	Mg	Al	Si	P	S	Cl	K	Ca	Ti	Cr	Fe	Zn	Total
Slice 1.1, Site 6, Zone 1	Rust growth on reinforcement														
Spectrum 265	22,68	0,00	0,00	0,00	0,30	0,10	0,15	0,15	0,00	0,00	0,02	0,17	76,30	0,13	100,00
Spectrum 266	22,58	0,00	0,01	0,00	0,19	0,03	0,21	0,18	0,00	0,05	0,00	0,09	76,49	0,18	100,00
Spectrum 268	22,72	0,03	0,03	0,02	0,10	0,01	0,46	0,29	0,03	0,00	0,00	0,00	76,26	0,05	100,00
Spectrum 269	22,58	0,00	0,00	0,05	0,32	0,06	0,01	0,02	0,02	0,00	0,00	0,17	76,77	0,00	100,00
Spectrum 270	22,31	0,09	0,01	0,00	0,15	0,00	0,20	1,31	0,02	0,00	0,06	0,14	75,68	0,04	100,00
Spectrum 272	22,55	0,05	0,00	0,00	0,25	0,05	0,05	0,04	0,00	0,02	0,06	0,11	76,82	0,00	100,00
Spectrum 273	22,95	0,11	0,00	0,04	0,12	0,06	0,63	0,23	0,01	0,08	0,00	0,00	75,62	0,15	100,00
Spectrum 275	22,17	0,01	0,00	0,01	0,06	0,02	0,03	1,34	0,02	0,03	0,00	0,77	75,55	0,00	100,00
Spectrum 276	22,84	0,00	0,08	0,02	0,03	0,07	0,51	0,12	0,00	0,00	0,00	0,12	76,00	0,22	100,00
Spectrum 277	22,45	0,00	0,01	0,07	0,10	0,03	0,17	0,43	0,00	0,00	0,00	0,00	76,75	0,00	100,00
Spectrum 278	22,54	0,00	0,03	0,04	0,21	0,04	0,08	0,00	0,03	0,02	0,01	0,02	76,98	0,00	100,00
Spectrum 279	22,73	0,00	0,00	0,08	0,23	0,08	0,40	0,73	0,00	0,00	0,00	0,06	75,34	0,35	100,00
Spectrum 281	22,72	0,00	0,00	0,12	0,01	0,09	0,33	0,13	0,00	0,00	0,06	0,07	76,46	0,00	100,00
Spectrum 282	22,58	0,00	0,02	0,00	0,02	0,03	0,32	0,17	0,00	0,04	0,00	0,11	76,56	0,15	100,00
Spectrum 283	22,69	0,01	0,01	0,00	0,07	0,06	0,38	0,26	0,00	0,00	0,00	0,20	76,26	0,05	100,00
Spectrum 286	22,62	0,00	0,02	0,01	0,26	0,01	0,17	0,08	0,00	0,01	0,00	0,11	76,71	0,00	100,00
Spectrum 287	22,79	0,02	0,00	0,06	0,27	0,08	0,28	0,09	0,00	0,05	0,00	0,08	76,29	0,00	100,00
Spectrum 288	22,61	0,00	0,00	0,00	0,25	0,07	0,12	0,07	0,00	0,04	0,01	0,08	76,74	0,00	100,00
Spectrum 289	22,73	0,00	0,05	0,02	0,28	0,04	0,24	0,04	0,03	0,00	0,00	0,08	76,49	0,00	100,00
Spectrum 291	22,91	0,00	0,00	0,00	0,16	0,08	0,52	0,17	0,00	0,02	0,00	0,29	75,46	0,39	100,00
Spectrum 292	21,61	0,00	0,09	0,00	0,13	0,08	0,14	4,44	0,03	0,01	0,06	0,13	73,22	0,07	100,00
Spectrum 293	22,78	0,00	0,01	0,07	0,17	0,21	0,23	0,25	0,00	0,03	0,02	0,22	76,01	0,00	100,00
Spectrum 294	22,83	0,13	0,00	0,02	0,16	0,01	0,57	0,55	0,05	0,12	0,00	0,08	75,46	0,00	100,00
Slice 1.1, Site 6, Zone 1	Cl-rich rust														
Spectrum 267	21,06	0,06	0,00	0,08	0,66	0,19	0,26	9,55	0,00	0,00	0,00	0,30	67,76	0,07	100,00
Spectrum 271	17,87	0,04	0,00	0,17	0,62	0,05	0,05	22,43	0,00	0,01	0,00	0,17	58,53	0,07	100,00
Spectrum 274	20,79	0,29	0,00	0,07	0,50	0,07	0,20	9,49	0,00	0,05	0,00	0,08	68,47	0,00	100,00
Spectrum 280	21,69	0,00	0,15	0,09	0,19	0,05	0,35	5,31	0,03	0,01	0,00	0,24	71,90	0,00	100,00
Spectrum 284	22,56	0,00	0,07	0,07	1,13	0,55	0,27	5,71	0,00	0,04	0,05	0,55	68,38	0,60	100,00
Spectrum 285	20,98	0,07	0,00	0,00	0,31	0,08	0,17	7,84	0,00	0,09	0,00	0,18	70,28	0,00	100,00
Spectrum 290	18,37	0,00	0,01	0,09	0,10	0,06	0,04	18,50	0,00	0,06	0,00	0,17	62,60	0,00	100,00

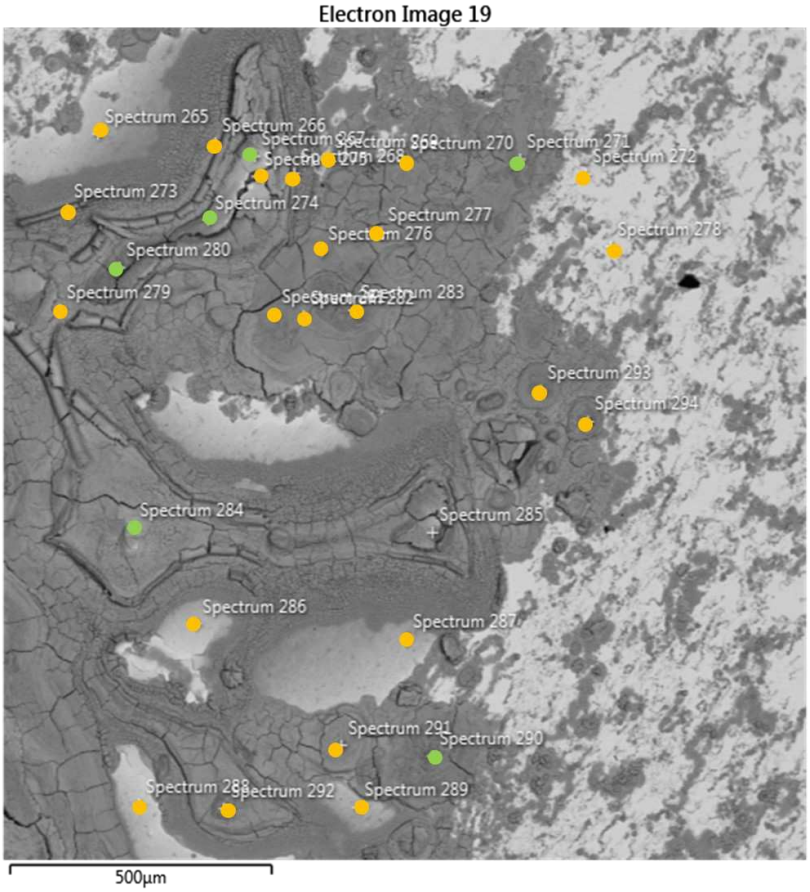

Fig. A6. BSE image of Site 6, Slice 1.1.

Table A6. EDS analysis of Site 7, Slice 1.1

Spectrum Label	O	Na	Mg	Al	Si	P	S	Cl	K	Ca	Ti	Cr	Fe	Zn	Total
Slice 1.1, Site 7, Zone 1															
Spectrum 295	22,52	0,02	0,02	0,03	0,25	0,05	0,02	0,02	0,00	0,01	0,00	0,10	76,95	0,00	100,00
Spectrum 296	21,02	0,03	0,00	0,03	0,14	0,04	0,06	6,58	0,03	0,22	0,00	0,02	71,81	0,00	100,00
Spectrum 301	22,69	0,07	0,05	0,00	0,21	0,06	0,04	0,11	0,03	2,17	0,00	0,14	74,44	0,00	100,00
Spectrum 307	27,40	0,61	0,04	0,19	7,20	0,08	0,06	0,09	0,30	1,69	0,00	0,04	62,24	0,07	100,00
Spectrum 310	23,91	0,00	0,02	0,07	1,55	0,35	0,04	0,16	0,03	3,32	0,00	0,10	70,35	0,10	100,00
Slice 1.1, Site 7, Zone 2															
Spectrum 297	33,41	2,51	0,02	4,49	12,97	0,04	0,05	0,02	0,10	2,78	0,00	0,01	43,55	0,07	100,00
Spectrum 298	31,80	1,81	0,07	3,67	11,06	0,00	0,04	0,20	0,11	4,20	0,00	0,17	46,79	0,08	100,00
Spectrum 299	26,89	0,33	0,17	0,60	5,40	0,15	0,11	0,37	0,11	6,33	0,01	0,10	59,45	0,00	100,00
Spectrum 300	28,72	0,33	0,15	0,53	8,13	0,16	0,05	0,61	0,04	7,82	0,11	0,04	53,30	0,00	100,00
Spectrum 309	41,33	0,10	0,03	0,06	28,33	0,02	0,12	0,00	0,03	1,20	0,02	0,00	28,71	0,04	100,00
Slice 1.1, Site 7, Zone 3															
Spectrum 302	31,45	0,63	0,68	1,10	8,15	0,06	0,32	0,11	0,19	31,03	0,00	0,00	26,28	0,00	100,00
Spectrum 303	39,55	0,11	2,05	1,77	18,97	0,07	0,67	1,80	0,00	33,95	0,03	0,17	0,87	0,00	100,00
Spectrum 304	38,13	0,09	3,88	1,74	16,47	0,11	0,39	2,43	0,03	35,24	0,00	0,05	1,43	0,00	100,00
Spectrum 305	34,19	0,28	2,27	3,04	11,81	0,08	0,25	0,22	0,23	19,90	0,09	0,09	27,08	0,47	100,00
Spectrum 306	38,65	0,18	0,49	1,10	19,20	0,03	0,36	2,69	0,07	36,88	0,00	0,00	0,34	0,02	100,00
Spectrum 308	37,71	0,04	3,51	1,61	15,55	0,09	0,29	1,76	0,05	38,68	0,04	0,08	0,59	0,00	100,00
Spectrum 311	31,98	0,00	0,49	0,46	7,11	0,11	0,37	2,06	0,04	53,20	0,06	0,00	3,83	0,29	100,00
Spectrum 312	31,34	0,01	0,20	0,26	6,82	0,00	0,65	2,93	0,05	50,36	0,00	0,00	7,38	0,00	100,00

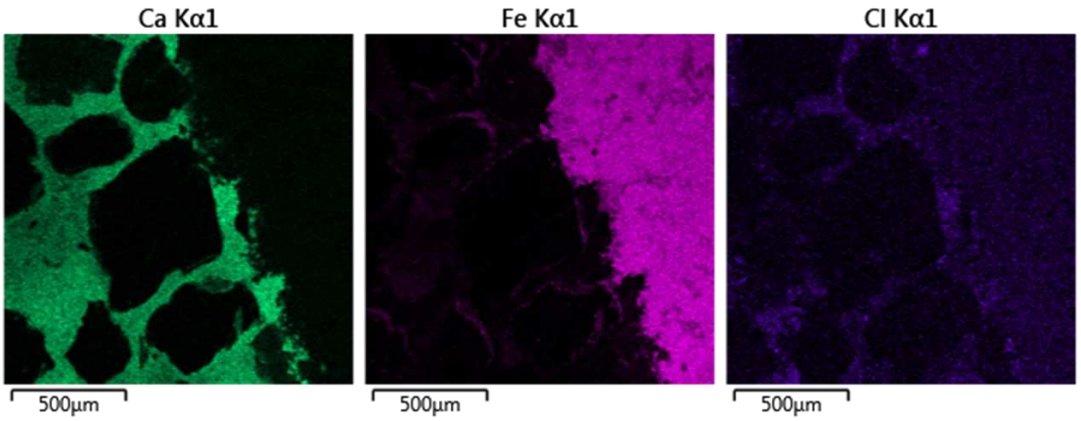

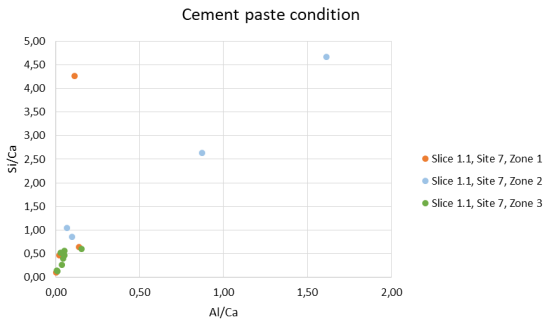

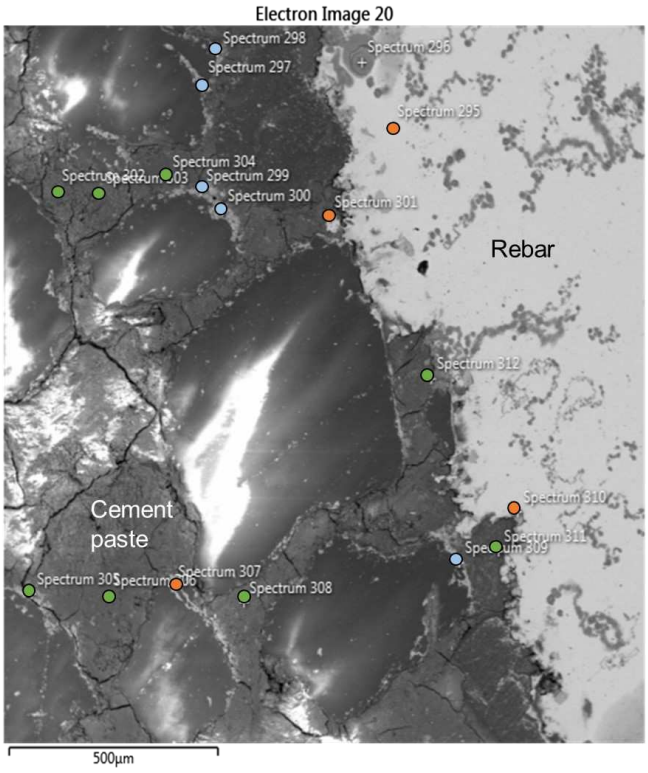

Fig. A7. Element maps, graph and BSE image of Site 7, Slice 1.1.

Table A7. EDS analysis of Site 9, Slice 1.1

Spectrum Label	O	Na	Mg	Al	Si	P	S	Cl	K	Ca	Ti	Cr	Fe	Zn	Total
Slice 1.1, Site 9, Cement paste															
Spectrum 313	37,02	1,67	0,64	1,18	15,48	0,03	0,05	0,26	0,76	40,98	0,32	0,14	1,47	0,00	100,00
Spectrum 314	36,92	0,13	0,31	1,38	15,45	0,02	0,31	1,62	0,00	41,93	0,15	0,00	1,73	0,06	100,00
Spectrum 315	37,01	0,93	0,74	1,06	15,24	0,01	0,20	0,18	0,38	42,59	0,00	0,16	1,50	0,00	100,00
Spectrum 316	38,17	2,48	2,26	1,43	16,50	0,12	0,26	0,00	0,90	36,98	0,04	0,00	0,60	0,27	100,00
Spectrum 317	39,82	2,89	3,78	1,83	18,86	0,00	0,36	0,13	0,94	30,76	0,05	0,00	0,58	0,00	100,00
Spectrum 318	36,52	0,52	2,14	3,61	12,08	0,19	0,32	0,38	0,22	39,48	0,32	0,00	4,19	0,04	100,00
Spectrum 320	38,22	0,34	0,82	2,34	15,55	0,29	0,58	0,28	0,02	40,78	0,00	0,04	0,73	0,00	100,00
Spectrum 321	36,38	1,00	0,35	1,85	13,39	0,08	0,25	0,05	0,62	44,81	0,15	0,00	1,07	0,00	100,00
Spectrum 322	34,79	0,81	0,13	8,31	8,76	0,00	0,24	4,49	0,77	40,75	0,00	0,00	0,95	0,00	100,00
Spectrum 323	38,54	1,61	7,32	2,43	14,71	0,03	0,30	0,02	0,55	33,45	0,00	0,00	1,03	0,01	100,00
Spectrum 324	37,44	0,67	1,50	2,15	14,84	0,01	0,30	0,08	0,36	41,16	0,00	0,00	1,47	0,00	100,00
Spectrum 325	36,30	0,16	1,95	1,41	14,32	0,01	0,17	2,25	0,12	41,54	0,05	0,00	1,65	0,07	100,00
Spectrum 326	36,09	1,71	0,93	1,74	14,23	0,00	0,18	0,11	0,68	35,02	0,11	0,18	8,92	0,09	100,00
Spectrum 327	36,73	0,95	1,33	7,76	10,55	0,09	0,41	0,07	0,20	33,02	0,26	0,00	8,63	0,00	100,00
Slice 1.1, Site 9, Clinker grain?															
Spectrum 319	33,40	0,60	0,19	0,87	8,55	0,00	0,30	0,02	0,23	53,60	0,05	0,00	2,20	0,00	100,00
Spectrum 328	28,76	0,05	0,04	0,22	0,92	0,00	0,03	0,14	0,17	65,79	0,00	0,10	3,77	0,01	100,00

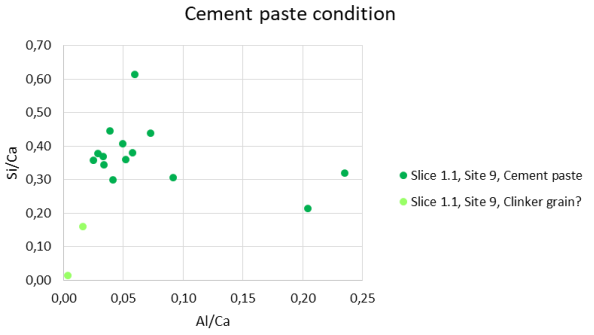

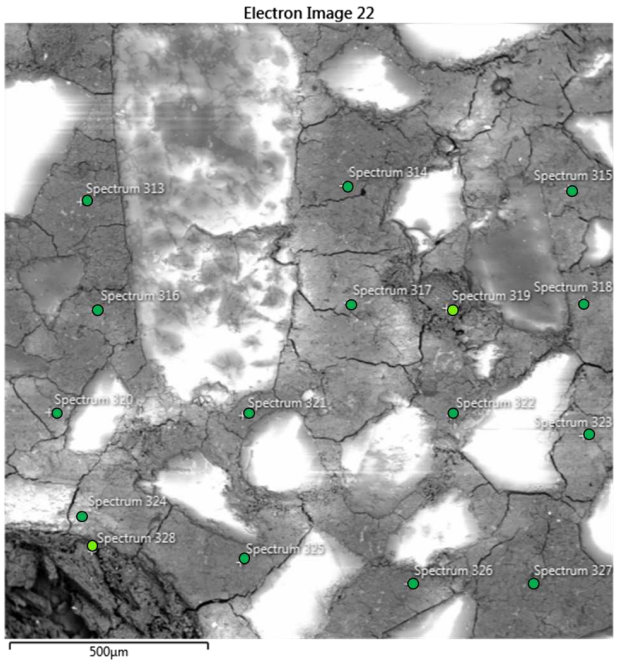

Fig. A8. Graph and BSE image of Site 9, Slice 1.1.

Table A8. EDS analysis of Site 9, Slice 1.1

Spectrum Label	O	Na	Mg	Al	Si	P	S	Cl	K	Ca	Ti	Cr	Fe	Zn	Total
Slice 1.1, Site 10, Zone 1															
Spectrum 329	21,93	0,00	0,00	0,05	0,03	0,01	0,33	3,46	0,00	0,68	0,02	0,03	73,18	0,29	100,00
Spectrum 330	23,04	0,22	0,00	0,01	0,12	0,01	0,77	0,34	0,00	0,11	0,04	0,04	75,10	0,21	100,00
Spectrum 336	21,51	0,00	0,00	0,03	0,14	0,00	0,20	4,94	0,03	0,25	0,09	0,02	72,49	0,30	100,00
Spectrum 337	23,11	0,27	0,00	0,07	0,06	0,00	0,84	0,24	0,09	0,08	0,00	0,13	75,11	0,00	100,00
Spectrum 341	22,58	0,00	0,00	0,00	0,06	0,00	0,26	1,15	0,04	3,34	0,03	0,00	72,29	0,25	100,00
Spectrum 342	22,79	0,26	0,00	0,00	0,10	0,00	0,50	0,16	0,09	0,04	0,00	0,11	75,76	0,19	100,00
Spectrum 346	32,32	2,57	0,07	4,51	13,35	0,00	0,32	6,20	0,00	0,22	0,00	0,12	40,09	0,23	100,00
Spectrum 347	22,31	0,00	0,00	0,08	0,09	0,01	0,36	2,21	0,00	1,00	0,03	0,07	73,55	0,29	100,00
Spectrum 348	22,77	0,32	0,00	0,07	0,07	0,00	0,72	1,36	0,00	0,39	0,00	0,00	74,29	0,01	100,00
Spectrum 352	23,03	0,00	0,00	0,11	0,00	0,02	0,82	0,43	0,00	0,01	0,00	0,14	75,43	0,00	100,00
Spectrum 353	22,48	0,06	0,03	0,00	0,20	0,01	0,54	2,04	0,07	0,07	0,00	0,07	74,43	0,00	100,00
Spectrum 356	22,91	0,66	0,02	0,06	0,20	0,05	0,31	1,11	0,13	4,13	0,06	0,00	70,15	0,20	100,00
Spectrum 357	22,87	1,15	0,02	0,02	0,13	0,08	0,16	0,83	0,23	4,90	0,00	0,02	69,60	0,00	100,00
Slice 1.1, Site 10, Zone 2															
Spectrum 331	20,68	0,00	0,05	0,25	1,10	0,80	0,27	15,32	0,00	0,03	0,16	0,27	61,09	0,00	100,00
Spectrum 332	18,25	0,00	0,00	0,35	0,40	0,07	0,56	22,79	0,05	0,12	0,09	0,17	57,16	0,00	100,00
Spectrum 333	19,26	0,00	0,00	0,00	0,73	0,13	0,22	17,15	0,06	0,04	0,00	0,16	62,09	0,17	100,00
Spectrum 334	19,14	0,15	0,05	0,12	0,37	0,14	0,16	16,64	0,00	0,00	0,01	0,00	63,23	0,00	100,00
Spectrum 335	19,74	0,00	0,00	0,04	0,06	0,12	0,03	12,25	0,00	0,01	0,02	0,11	67,43	0,18	100,00
Spectrum 338	20,89	0,00	0,00	0,04	1,49	0,47	0,16	13,62	0,10	0,13	0,04	0,94	61,61	0,51	100,00
Spectrum 339	18,79	0,00	0,00	0,12	0,47	0,00	0,60	19,92	0,07	0,00	0,05	0,10	59,89	0,00	100,00
Spectrum 340	20,49	0,03	0,05	0,00	0,05	0,11	0,02	8,87	0,00	0,00	0,00	0,28	70,06	0,03	100,00
Spectrum 343	20,54	0,00	0,00	0,13	1,67	0,44	0,16	15,51	0,00	0,07	0,00	0,34	61,13	0,00	100,00
Spectrum 344	18,33	0,00	0,29	0,06	0,37	0,20	0,52	22,47	0,00	0,00	0,16	0,11	57,49	0,00	100,00
Spectrum 345	20,58	0,00	0,08	0,15	0,24	0,14	0,82	12,88	0,00	0,02	0,14	0,06	64,90	0,00	100,00
Spectrum 349	20,83	0,15	0,00	0,02	1,20	0,31	0,14	11,93	0,00	0,02	0,01	0,23	65,16	0,00	100,00
Spectrum 350	20,64	0,00	0,02	0,03	1,39	0,19	0,07	12,81	0,06	0,09	0,10	0,36	63,77	0,46	100,00

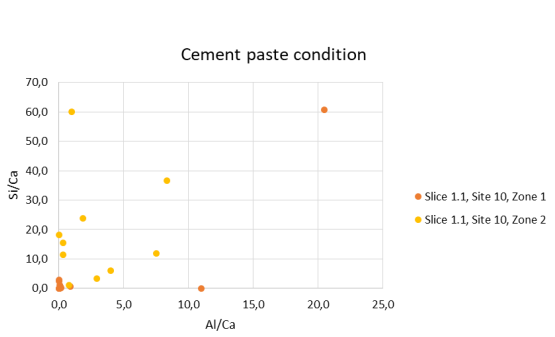

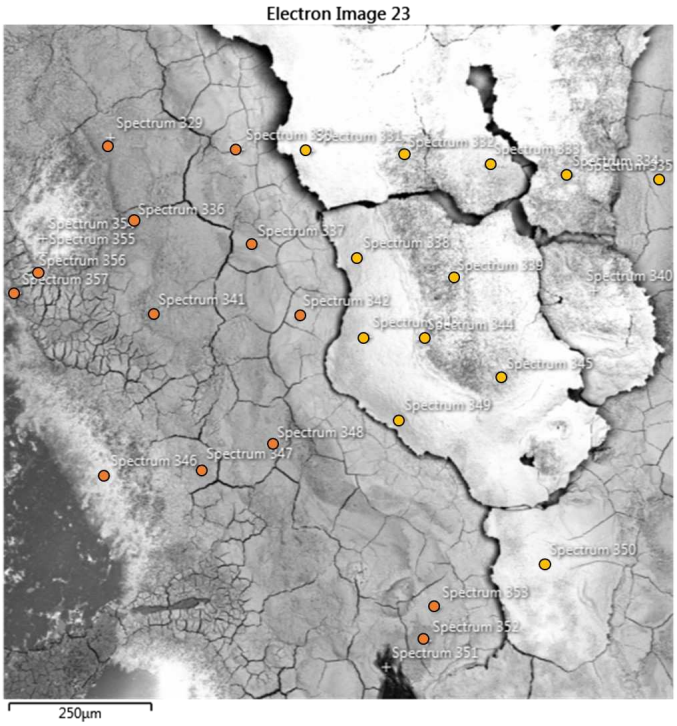

Fig. A9. Graph and BSE image of Site 10, Slice 1.1.

Table A9. EDS analysis of Site 11, Slice 1.1

Spectrum Label	O	Na	Mg	Al	Si	P	S	Cl	K	Ca	Ti	Cr	Fe	Zn	Total
Si-rich core + Fe															
Spectrum 358	50,29	0,06	0,04	0	42,37	0	0,05	0,67	0,01	0,04	0	0,13	6,33	0	100
Spectrum 359	35,79	0,03	0,01	0,02	21,53	0	0,17	4,2	0,07	0,1	0,01	0,07	37,95	0,07	100
Fe-rich + Si															
Spectrum 360	21,97	0,01	0	0	0,53	0,03	0,46	5,02	0,03	0,27	0	0,03	71,22	0,43	100
Spectrum 361	22,61	0,43	0	0,1	0,2	0	0,48	1,76	0,05	1,05	0	0,05	73,07	0,19	100
Spectrum 362	22,85	0,4	0	0	0,08	0	0,27	1,05	0,05	5,18	0,12	0	69,82	0,17	100
Spectrum 363	21,5	0	0	0,12	0,12	0,03	0,22	5,24	0,05	0,22	0	0,17	72,05	0,27	100
Spectrum 364	22,56	0,08	0	0	0,05	0,02	0,14	0,88	0,06	3,58	0	0	72,63	0	100

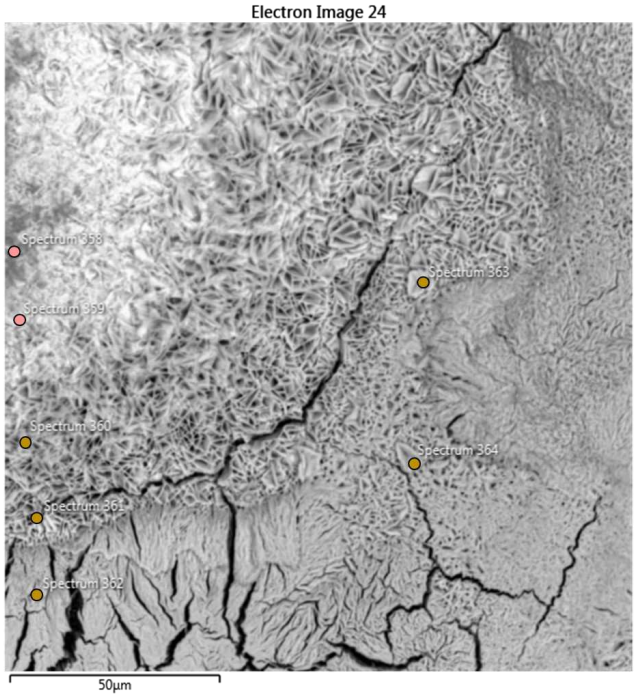

Fig. A10. BSE image of Site 11, Slice 1.1.

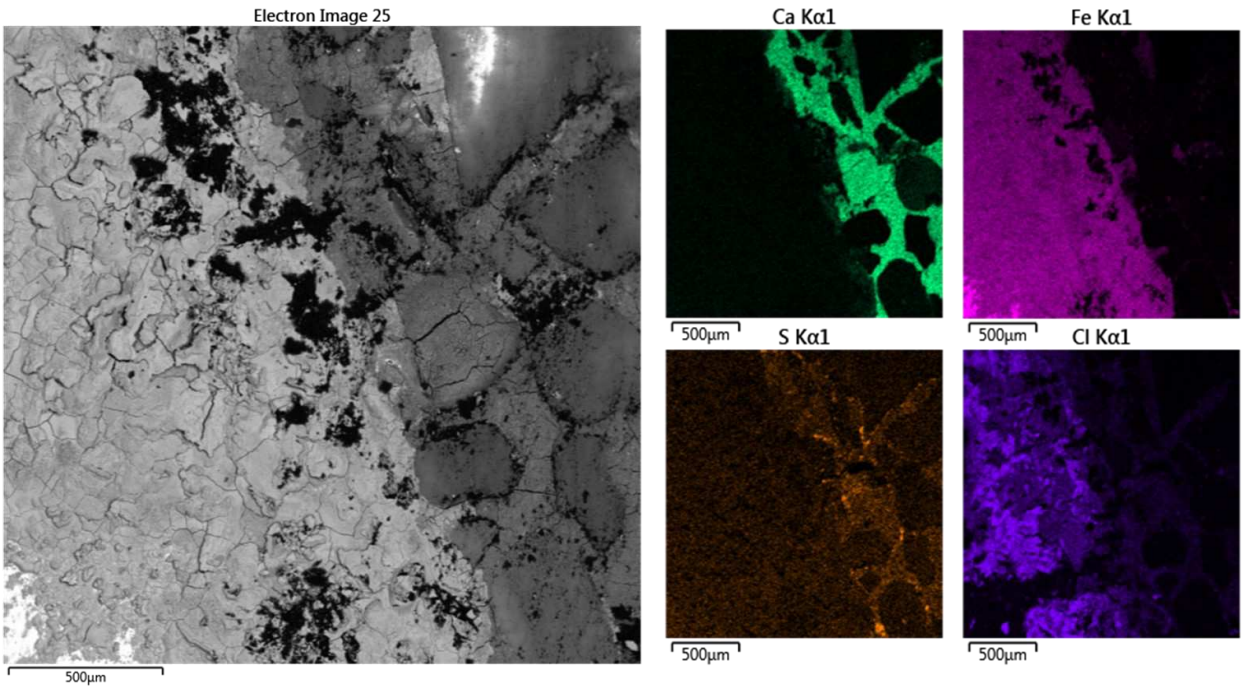

Fig. A11. BSE image and element maps of Site 12, Slice 1.1.

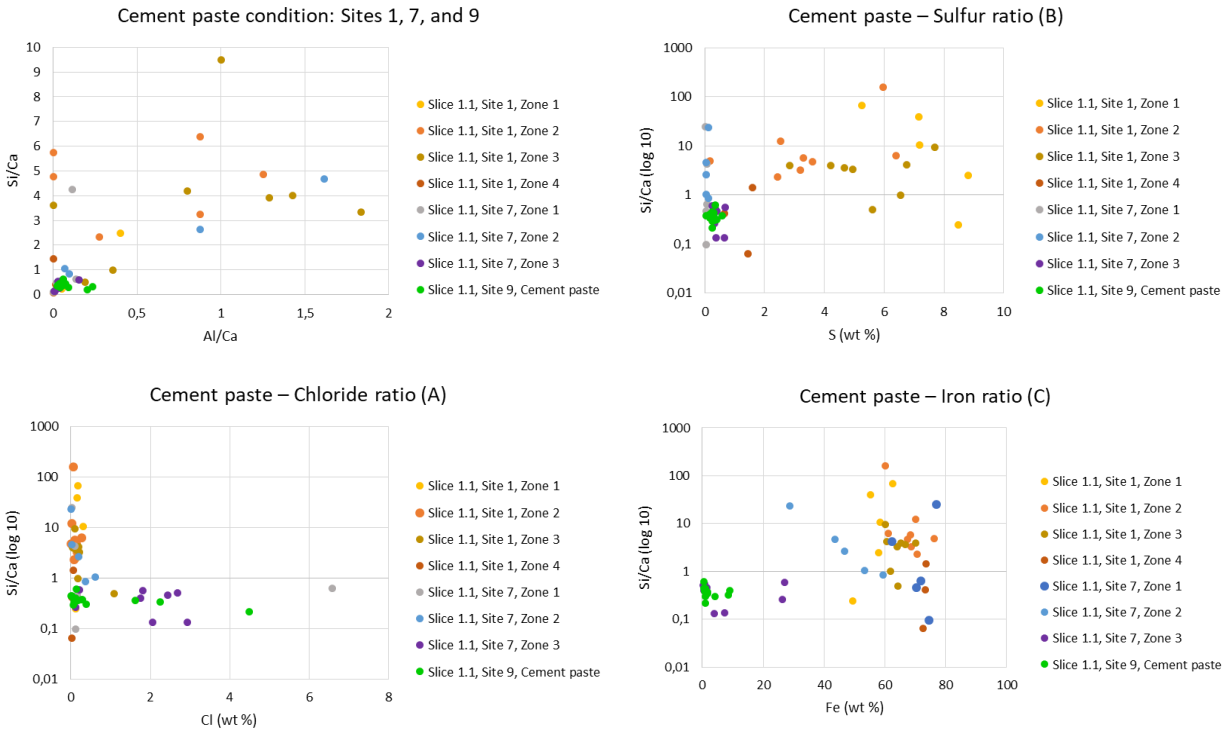

Fig. A12. Graphs of combined cement paste conditions of Sites 1, 7 and 9, Slice 1.1.

Table A10. EDS analysis of Site 1, Slice 1.2.

Spectrum Label	O	Na	Mg	Al	Si	P	S	Cl	K	Ca	Ti	Cr	Fe	Zn	Total
Slice 1.2, Site 1, Zone 1	**Light grey surface**														
Spectrum 1	23,44	0,00	0,14	0,05	0,69	0,09	0,65	0,21	0,03	0,11	0,05	0,00	74,21	0,34	100,00
Spectrum 2	23,96	0,00	0,26	0,28	1,43	0,00	0,61	0,25	0,06	0,23	0,06	0,03	72,52	0,30	100,00
Spectrum 3	23,77	0,15	0,21	0,27	1,01	0,01	0,70	0,21	0,11	0,17	0,00	0,05	73,30	0,03	100,00
Spectrum 4	23,07	0,05	0,23	0,01	0,45	0,01	0,59	0,54	0,15	0,06	0,00	0,04	74,57	0,24	100,00
Spectrum 5	23,40	0,00	0,11	0,00	0,65	0,03	0,78	0,45	0,03	0,10	0,03	0,00	74,17	0,25	100,00
Spectrum 6	23,44	0,14	0,03	0,03	0,45	0,00	0,91	0,08	0,00	0,09	0,00	0,03	74,57	0,23	100,00
Spectrum 7	23,98	0,01	0,06	0,22	1,01	0,05	0,97	0,16	0,03	0,05	0,00	0,00	73,34	0,10	100,00
Spectrum 8	23,87	0,23	0,00	0,08	0,43	0,05	1,35	0,12	0,17	0,00	0,00	0,04	73,65	0,00	100,00
Spectrum 9	23,11	0,02	0,01	0,07	0,36	0,00	0,62	0,14	0,05	0,10	0,00	0,08	75,46	0,00	100,00
Spectrum 10	23,37	0,07	0,08	0,04	0,47	0,07	0,75	0,13	0,04	0,14	0,00	0,00	74,70	0,12	100,00
Spectrum 11	24,68	0,44	0,05	0,10	0,95	0,00	1,82	0,12	0,01	0,02	0,01	0,06	71,74	0,00	100,00
Slice 1.2, Site 1, Zone 2	**Medium grey middle**														
Spectrum 12	34,93	1,08	0,43	0,41	1,13	0,10	12,28	0,31	0,21	0,12	0,01	0,05	48,42	0,51	100,00
Spectrum 13	40,42	0,14	2,83	8,65	12,84	0,05	4,71	0,07	1,87	0,18	1,37	0,00	26,80	0,04	100,00
Spectrum 14	25,31	0,64	0,09	0,10	0,90	0,07	2,51	0,27	0,18	0,00	0,00	0,00	69,72	0,21	100,00
Spectrum 15	29,20	0,89	0,42	1,73	4,89	0,05	3,14	0,69	1,99	0,08	0,00	0,00	56,81	0,11	100,00
Spectrum 16	28,72	0,95	0,18	1,24	2,58	0,07	4,39	0,59	0,38	0,14	0,04	0,07	60,51	0,13	100,00
Spectrum 17	30,80	0,77	0,09	0,22	0,72	0,09	8,44	0,60	0,02	0,07	0,00	0,07	58,10	0,00	100,00
Spectrum 18	29,13	2,50	0,21	0,43	1,14	0,06	6,18	0,82	0,08	0,09	0,12	0,00	59,24	0,00	100,00
Spectrum 19	26,73	1,02	0,00	0,03	0,17	0,06	4,68	0,76	0,06	0,04	0,05	0,08	65,90	0,44	100,00
Spectrum 20	26,98	0,98	0,13	0,54	0,97	0,16	3,98	0,67	0,06	0,00	0,05	0,01	65,47	0,00	100,00
Spectrum 21	26,28	0,76	0,03	0,05	0,28	0,04	4,01	0,29	0,06	0,09	0,07	0,02	67,86	0,16	100,00
Spectrum 22	42,70	11,95	0,39	0,16	0,15	0,02	20,82	0,06	0,01	0,00	0,02	0,00	23,11	0,62	100,00
Spectrum 23	26,93	1,21	0,06	0,51	1,34	0,14	3,70	0,68	0,18	0,13	0,05	0,05	65,00	0,00	100,00
Spectrum 24	28,04	1,42	0,06	0,07	0,24	0,15	5,84	0,58	0,05	0,16	0,00	0,05	63,35	0,00	100,00
Spectrum 25	30,32	3,62	0,10	0,51	1,09	0,13	7,23	0,23	0,06	0,19	0,01	0,09	56,40	0,00	100,00
Spectrum 26	29,34	1,43	0,11	0,01	0,34	0,02	7,16	0,05	0,04	0,00	0,00	0,03	61,48	0,00	100,00
Spectrum 27	30,38	3,65	0,13	0,38	0,57	0,08	7,77	0,28	0,02	0,14	0,01	0,10	56,48	0,00	100,00
Spectrum 28	33,16	1,13	0,39	0,22	0,55	0,09	10,92	0,42	0,11	0,20	0,00	0,00	52,66	0,16	100,00
Spectrum 29	29,05	1,56	0,16	0,86	2,00	0,12	5,24	0,42	0,23	0,08	0,05	0,00	60,23	0,00	100,00
Spectrum 30	27,42	1,76	0,06	0,16	0,92	0,31	4,58	0,82	0,02	0,09	0,00	0,05	63,37	0,45	100,00
Spectrum 31	31,90	4,63	0,00	0,45	1,08	0,06	8,98	0,13	0,03	0,23	0,03	0,04	52,28	0,17	100,00
Slice 1.2, Site 1, Zone 3	**Dark grey spotty area**														
Spectrum 32	*42,32*	*12,98*	*0,36*	*0,19*	*0,33*	*0,09*	*20,47*	*1,68*	*0,01*	*0,34*	*0,11*	*0,00*	*20,90*	*0,21*	*100,00*
Spectrum 33	28,06	2,08	0,12	0,10	0,46	0,11	5,64	0,44	0,07	0,12	0,05	0,00	62,54	0,21	100,00
Spectrum 34	*40,94*	*4,15*	*0,15*	*0,88*	*4,95*	*0,09*	*15,66*	*0,34*	*0,16*	*0,36*	*0,00*	*0,01*	*32,04*	*0,28*	*100,00*
Spectrum 35	41,86	1,70	1,03	9,35	14,03	0,07	6,21	1,08	2,91	0,22	0,12	0,00	21,41	0,00	100,00
Spectrum 36	28,62	2,14	0,11	0,52	1,26	0,12	5,54	0,79	0,05	0,00	0,00	0,07	60,57	0,19	100,00
Spectrum 37	*38,33*	*5,78*	*0,15*	*0,52*	*0,99*	*0,24*	*16,93*	*5,95*	*0,10*	*0,45*	*0,09*	*0,00*	*30,48*	*0,00*	*100,00*
Slice 1.2, Site 1, Zone 4	**Lighter area below**														
Spectrum 38	25,92	0,10	0,11	0,30	1,17	0,43	2,91	1,75	0,00	0,02	0,00	0,15	66,51	0,61	100,00
Spectrum 39	26,58	0,73	0,13	0,18	0,50	0,33	3,96	0,83	0,02	0,17	0,02	0,15	66,14	0,26	100,00
Spectrum 40	37,18	0,41	0,48	0,62	1,36	0,09	14,42	0,41	0,23	0,25	0,04	0,00	44,52	0,00	100,00
Spectrum 41	28,83	2,06	0,41	0,43	0,93	0,18	6,09	1,68	0,00	0,15	0,08	0,00	59,17	0,00	100,00

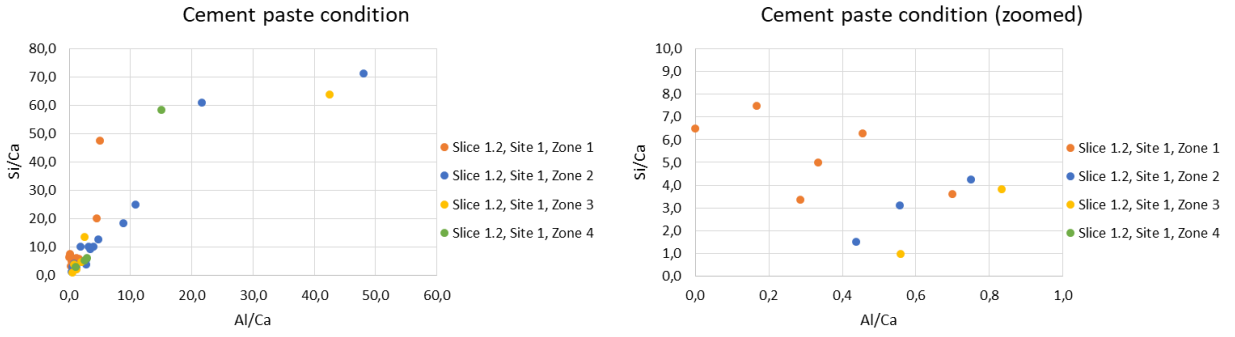

Fig. A13. Graphs and of Site 1, Slice 1.2.

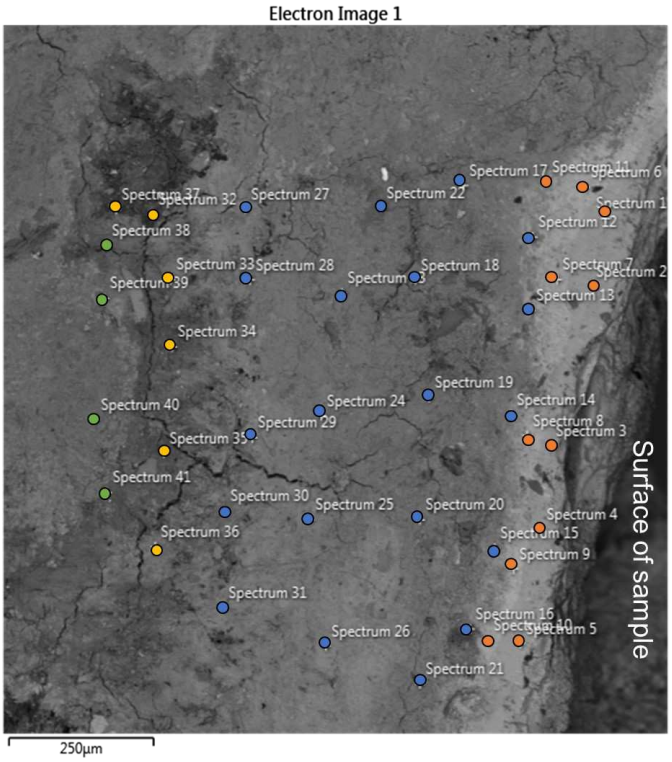

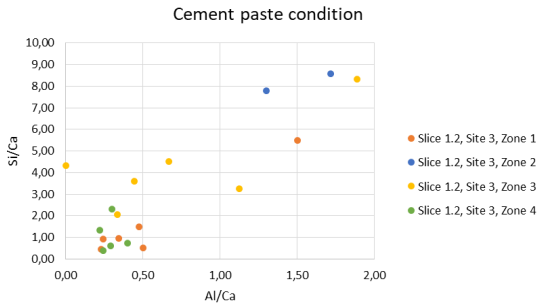

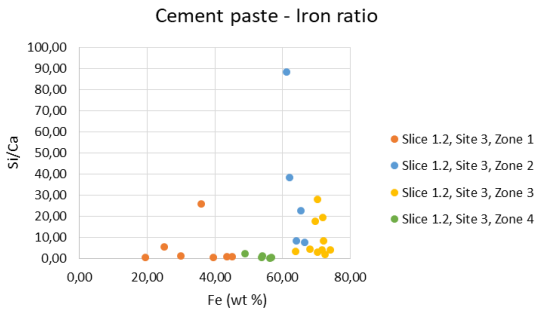

Fig. A14. BSE image of Site 1, Slice 1.2.

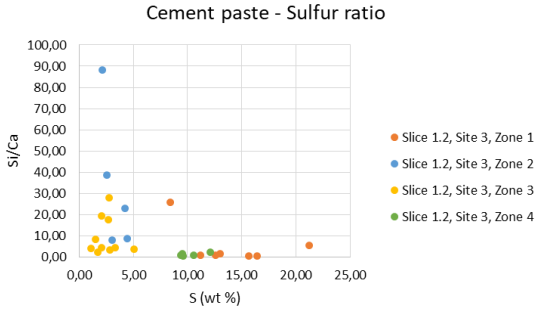

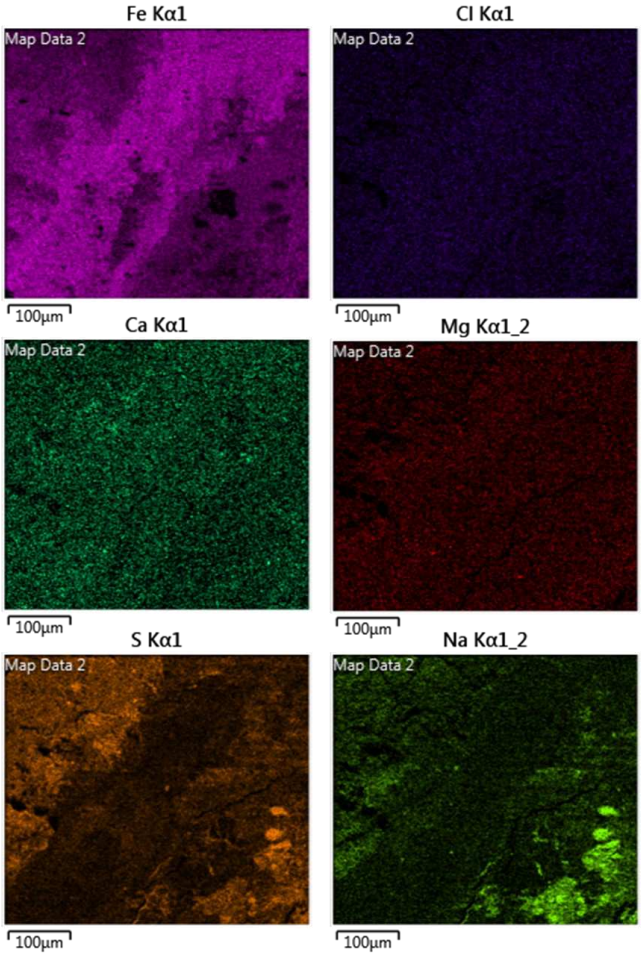

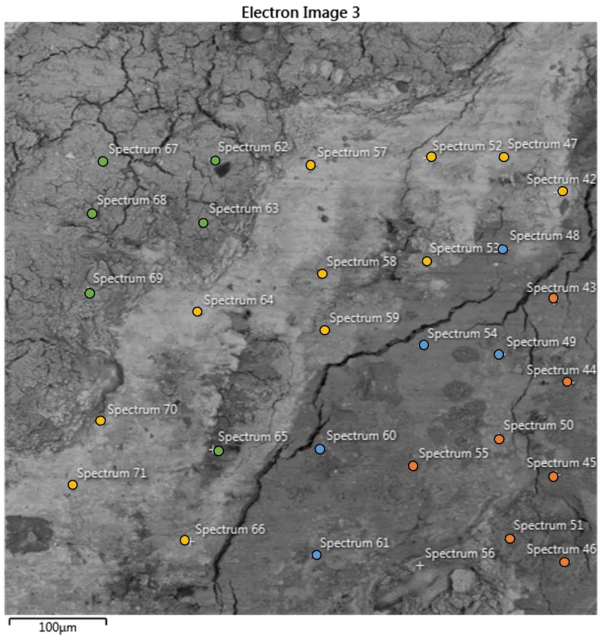

Fig. A15. Element maps, graphs and BSE image of Site 3, Slice 1.2.

Table A11. EDS analysis of Site 3, Slice 1.2.

Spectrum Label	O	Na	Mg	Al	Si	P	S	Cl	K	Ca	Ti	Cr	Fe	Zn	Total
Slice 1.2, Site 3, Zone 1															
Spectrum 43	36,15	18,60	0,35	0,19	0,59	0,26	13,02	0,34	0,12	0,40	0,00	0,00	29,98	0,00	100,00
Spectrum 44	42,85	9,74	0,34	0,03	0,11	0,02	21,22	0,14	0,06	0,02	0,00	0,02	24,98	0,49	100,00
Spectrum 45	38,43	25,67	0,23	0,06	0,12	0,00	15,67	0,00	0,00	0,26	0,01	0,00	19,56	0,00	100,00
Spectrum 46	34,58	7,76	0,16	0,06	0,23	0,03	12,57	0,67	0,06	0,25	0,00	0,05	43,53	0,07	100,00
Spectrum 50	33,74	8,60	0,34	0,12	0,33	0,14	11,20	0,04	0,06	0,35	0,06	0,00	45,03	0,00	100,00
Spectrum 51	38,04	5,38	0,11	0,05	0,05	0,01	16,40	0,10	0,03	0,10	0,00	0,01	39,63	0,08	100,00
Spectrum 55	33,67	16,53	0,30	1,02	3,10	0,21	8,42	0,51	0,02	0,12	0,05	0,00	36,04	0,00	100,00
Slice 1.2, Site 3, Zone 2															
Spectrum 48	27,06	1,50	0,12	0,01	0,91	0,23	4,20	0,29	0,06	0,04	0,00	0,06	65,52	0,00	100,00
Spectrum 49	26,20	1,30	0,28	0,13	0,78	0,60	3,06	0,60	0,05	0,10	0,00	0,04	66,43	0,42	100,00
Spectrum 54	27,25	1,95	0,26	0,12	0,60	0,49	4,41	0,82	0,00	0,07	0,00	0,00	64,03	0,00	100,00
Spectrum 60	27,90	0,50	0,13	2,15	3,53	0,50	2,14	0,84	0,52	0,04	0,11	0,09	61,16	0,39	100,00
Spectrum 61	27,77	0,50	1,56	0,47	3,09	0,73	2,52	0,80	0,00	0,08	0,00	0,00	62,18	0,31	100,00
Slice 1.2, Site 3, Zone 3															
Spectrum 42	25,31	1,43	0,15	0,00	0,53	0,08	2,69	0,09	0,04	0,03	0,02	0,08	69,56	0,00	100,00
Spectrum 47	24,52	0,63	0,04	0,08	0,39	0,00	2,06	0,11	0,00	0,02	0,00	0,02	71,99	0,14	100,00
Spectrum 52	24,20	0,56	0,15	0,05	0,31	0,01	1,74	0,10	0,06	0,15	0,00	0,02	72,65	0,00	100,00
Spectrum 53	27,68	1,87	0,10	0,08	0,65	0,10	5,08	0,28	0,04	0,18	0,00	0,08	63,86	0,00	100,00
Spectrum 57	25,21	0,77	0,00	0,09	0,26	0,06	2,81	0,19	0,00	0,08	0,05	0,09	70,39	0,00	100,00
Spectrum 58	24,54	0,77	0,07	0,00	0,39	0,01	2,10	0,23	0,01	0,09	0,00	0,10	71,69	0,00	100,00
Spectrum 59	25,90	1,30	0,09	0,08	0,54	0,12	3,34	0,42	0,00	0,12	0,00	0,00	68,00	0,09	100,00
Spectrum 64	25,27	0,46	0,01	0,09	0,56	0,00	2,73	0,13	0,04	0,02	0,02	0,13	70,39	0,14	100,00
Spectrum 66	24,37	0,39	0,09	0,17	0,75	0,13	1,54	0,29	0,11	0,09	0,00	0,00	72,06	0,02	100,00
Spectrum 70	23,42	0,46	0,04	0,11	0,54	0,03	0,75	0,14	0,05	0,00	0,06	0,00	74,40	0,00	100,00
Spectrum 71	23,65	0,14	0,04	0,21	0,37	0,05	1,06	0,13	0,02	0,09	0,01	0,00	74,15	0,06	100,00
Slice 1.2, Site 3, Zone 4															
Spectrum 62	33,97	4,18	0,07	0,03	0,23	0,03	12,08	0,33	0,15	0,10	0,00	0,00	48,84	0,00	100,00
Spectrum 63	31,36	1,49	0,08	0,09	0,19	0,05	9,36	0,21	0,06	0,31	0,00	0,00	56,81	0,00	100,00
Spectrum 65	28,57	0,36	0,18	0,78	2,08	0,34	4,94	1,94	0,16	0,07	0,03	0,05	60,46	0,04	100,00
Spectrum 67	31,52	1,56	0,05	0,08	0,13	0,03	9,62	0,31	0,00	0,33	0,00	0,00	56,37	0,00	100,00
Spectrum 68	32,69	1,37	0,09	0,18	0,33	0,05	10,59	0,19	0,07	0,45	0,07	0,04	53,89	0,00	100,00
Spectrum 69	31,76	2,69	0,13	0,09	0,54	0,04	9,49	0,35	0,06	0,41	0,00	0,14	54,12	0,17	100,00

Table A12. EDS analysis of Site 5, Slice 1.2.

Spectrum Label	O	Na	Mg	Al	Si	P	S	Cl	K	Ca	Ti	Cr	Fe	Zn	Total
Slice 1.2, Site 5, Zone 1		Cement right - S rich													
Spectrum 72	35,75	4,96	0,62	0,19	0,47	0,07	13,55	0,90	0,00	0,76	0,03	0,03	42,37	0,30	100,00
Spectrum 73	41,17	2,97	0,51	0,10	0,17	0,02	19,46	0,29	0,02	1,85	0,08	0,11	33,18	0,07	100,00
Spectrum 74	42,94	3,10	1,24	0,12	0,19	0,00	21,24	0,20	0,06	0,41	0,00	0,17	29,91	0,41	100,00
Spectrum 75	39,72	1,85	0,69	0,12	0,09	0,15	17,95	0,20	0,03	0,86	0,04	0,01	38,28	0,00	100,00
Spectrum 76	36,93	2,16	0,91	0,17	0,39	0,26	14,62	0,43	0,00	1,31	0,00	0,00	42,45	0,37	100,00
Spectrum 77	42,04	1,32	0,88	0,04	1,08	0,07	19,80	0,09	0,03	0,66	0,00	0,02	33,87	0,08	100,00
Spectrum 78	39,89	1,33	0,90	0,01	0,14	0,13	18,14	0,15	0,03	0,51	0,10	0,02	38,67	0,00	100,00
Slice 1.2, Site 5, Zone 2		Cement w higher Fe													
Spectrum 79	25,90	2,38	0,03	0,00	0,41	0,14	3,72	1,76	0,11	0,31	0,00	0,05	64,93	0,24	100,00
Spectrum 81	26,28	1,86	0,12	0,14	0,56	0,30	3,46	0,37	0,00	0,42	0,02	0,05	66,43	0,00	100,00
Spectrum 82	31,26	3,87	0,07	0,17	0,70	0,27	8,72	1,66	0,02	1,76	0,15	0,03	51,04	0,29	100,00
Spectrum 83	27,80	0,79	0,27	0,08	0,53	0,20	5,20	0,39	0,01	0,36	0,08	0,03	64,26	0,00	100,00
Slice 1.2, Site 5, Zone 3		Light grey rim													
Spectrum 80	24,06	0,73	0,03	0,08	0,39	0,13	1,49	0,38	0,00	0,11	0,00	0,13	72,46	0,00	100,00
Spectrum 86	24,12	0,49	0,06	0,06	0,78	0,23	1,19	0,25	0,00	0,00	0,10	0,00	72,58	0,13	100,00
Spectrum 87	23,61	0,38	0,00	0,04	0,61	0,36	0,73	0,32	0,00	0,04	0,01	0,00	73,86	0,04	100,00
Slice 1.2, Site 5, Zone 4		Transition zone?													
Spectrum 84	26,10	1,49	0,04	0,00	0,35	0,62	3,38	0,65	0,07	0,09	0,00	0,00	67,07	0,15	100,00
Spectrum 85	25,27	1,21	0,00	0,04	0,38	0,65	2,37	0,31	0,06	0,07	0,00	0,02	69,55	0,07	100,00
Spectrum 90	25,35	1,57	0,03	0,05	0,84	0,12	2,75	1,24	0,04	0,14	0,00	0,00	67,75	0,12	100,00
Slice 1.2, Site 5, Zone 5		Cement left - S rich													
Spectrum 88	29,63	2,53	0,05	0,02	0,25	0,16	7,30	0,30	0,03	1,60	0,00	0,04	57,97	0,14	100,00
Spectrum 89	36,47	0,87	0,12	0,09	1,09	0,07	14,31	0,66	0,16	0,02	0,01	0,03	45,96	0,16	100,00

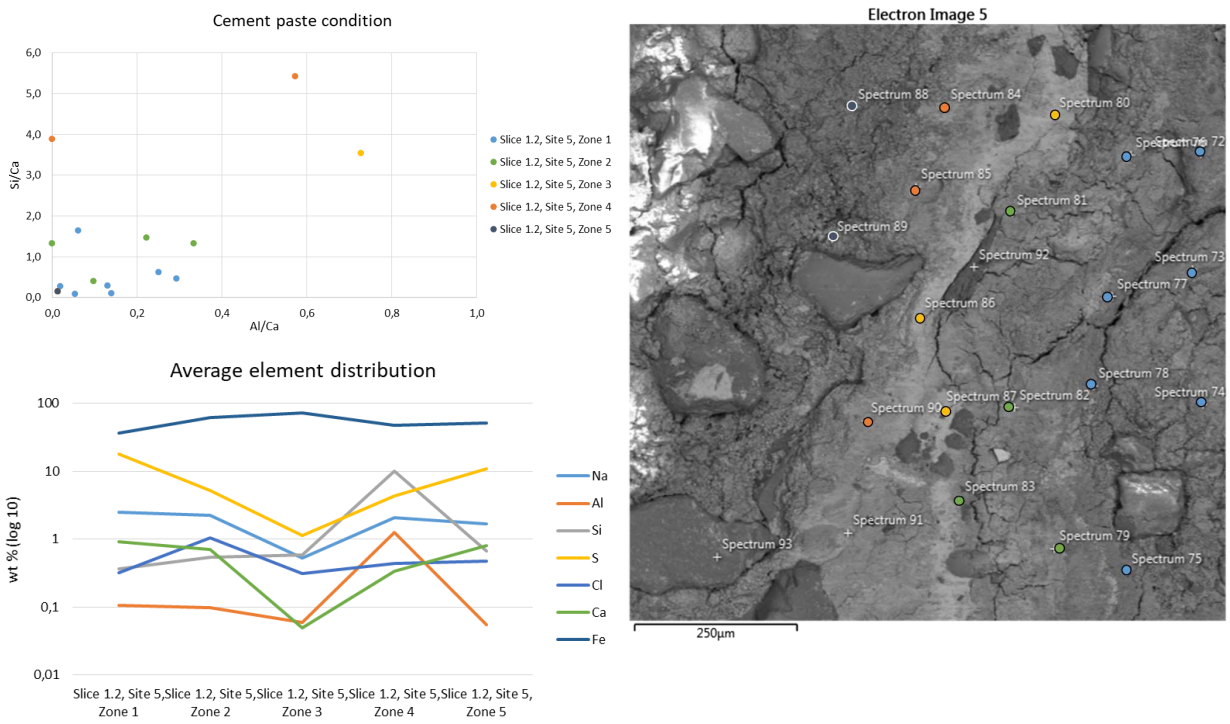

Fig. A16. Graphs and BSE image of Site 5, Slice 1.2.

Table A13. EDS analysis of Site 6, Slice 1.2.

Spectrum Label	O	Na	Mg	Al	Si	P	S	Cl	K	Ca	Ti	Cr	Fe	Zn	Total
Slice 1.2, Site 6, Zone 1															
Spectrum 94	27,85	1,33	0,53	1,14	2,35	0,16	3,22	0,14	0,20	1,70	0,05	0,00	61,20	0,13	100,00
Spectrum 95	26,39	0,74	0,41	0,55	2,24	0,27	2,13	0,13	0,09	0,48	0,00	0,02	66,56	0,00	100,00
Spectrum 96	26,27	1,31	0,29	0,63	1,14	0,39	2,62	0,17	0,12	0,82	0,00	0,07	66,13	0,03	100,00
Spectrum 97	25,24	1,84	0,07	0,15	0,09	0,70	2,38	0,24	0,09	0,21	0,00	0,00	68,48	0,50	100,00
Spectrum 98	25,87	0,99	0,36	0,38	1,20	0,23	2,38	0,01	0,05	0,80	0,01	0,00	67,74	0,00	100,00
Spectrum 99	25,31	0,35	0,34	0,08	2,22	0,38	1,21	0,27	0,07	0,48	0,06	0,02	68,64	0,59	100,00
Spectrum 100	25,92	0,46	0,19	0,09	0,32	0,72	2,97	0,37	0,08	0,17	0,06	0,08	68,57	0,00	100,00
Spectrum 101	25,36	2,24	0,16	0,11	0,20	0,45	2,55	0,03	0,00	0,27	0,00	0,00	68,43	0,21	100,00
Spectrum 103	26,85	0,86	0,77	0,48	2,14	0,05	2,79	0,13	0,12	0,53	0,00	0,01	65,27	0,00	100,00
Slice 1.2, Site 6, Zone 2															
Spectrum 102	23,63	0,17	0,28	0,13	0,78	0,15	0,50	0,03	0,02	1,22	0,00	0,04	73,05	0,00	100,00
Spectrum 104	23,06	0,18	0,14	0,06	0,15	0,06	0,58	0,08	0,05	0,32	0,00	0,13	75,19	0,00	100,00
Spectrum 105	23,76	0,00	0,26	0,19	0,93	0,17	0,59	0,03	0,07	0,29	0,00	0,06	73,52	0,13	100,00
Spectrum 106	22,99	0,11	0,24	0,15	0,26	0,16	0,23	0,06	0,00	0,72	0,05	0,00	75,03	0,00	100,00
Spectrum 107	24,72	0,30	0,73	0,21	0,79	0,38	1,22	0,06	0,09	1,86	0,07	0,03	69,28	0,26	100,00
Spectrum 108	22,90	0,10	0,16	0,08	0,18	0,21	0,22	0,02	0,00	0,51	0,00	0,04	75,58	0,00	100,00
Spectrum 109	23,14	0,00	0,20	0,02	0,78	0,08	0,17	0,00	0,04	0,66	0,00	0,06	74,85	0,01	100,00
Slice 1.2, Site 6, Zone 3															
Spectrum 110	24,87	0,03	0,10	0,00	1,48	0,11	1,37	0,02	0,03	2,24	0,05	0,13	69,57	0,00	100,00
Spectrum 111	28,96	0,09	0,16	0,05	3,26	0,19	4,00	0,03	0,01	5,84	0,00	0,29	57,12	0,00	100,00
Spectrum 112	27,08	0,08	0,00	0,05	2,28	0,12	3,02	0,00	0,00	3,50	0,05	0,12	63,69	0,00	100,00
Spectrum 113	25,57	0,83	0,18	0,14	1,87	0,12	0,80	0,07	0,00	11,42	0,03	0,46	58,50	0,00	100,00
Spectrum 116	25,24	0,17	6,58	0,17	0,64	0,14	0,33	0,30	0,00	2,36	0,02	0,00	63,84	0,21	100,00
Spectrum 117	25,10	0,18	0,12	0,07	1,11	0,10	1,59	0,13	0,03	5,04	0,00	0,26	66,27	0,00	100,00
Spectrum 118	24,09	0,44	0,07	0,09	1,23	0,14	0,53	0,02	0,00	3,14	0,00	0,30	69,94	0,02	100,00
Spectrum 119	29,27	1,33	0,05	0,06	5,73	0,31	1,92	0,14	0,00	11,72	0,00	0,35	49,12	0,00	100,00
Spectrum 120	25,27	0,75	0,01	0,02	1,52	0,21	1,40	0,03	0,00	4,68	0,12	0,14	65,85	0,00	100,00

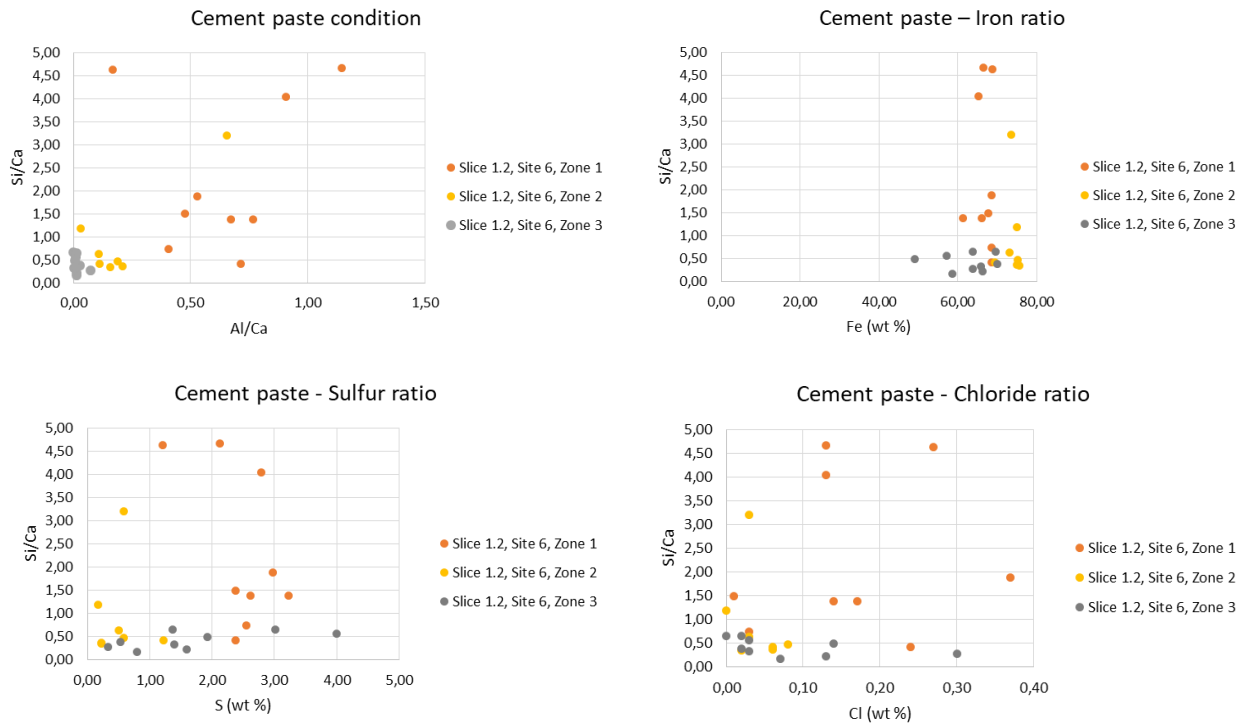

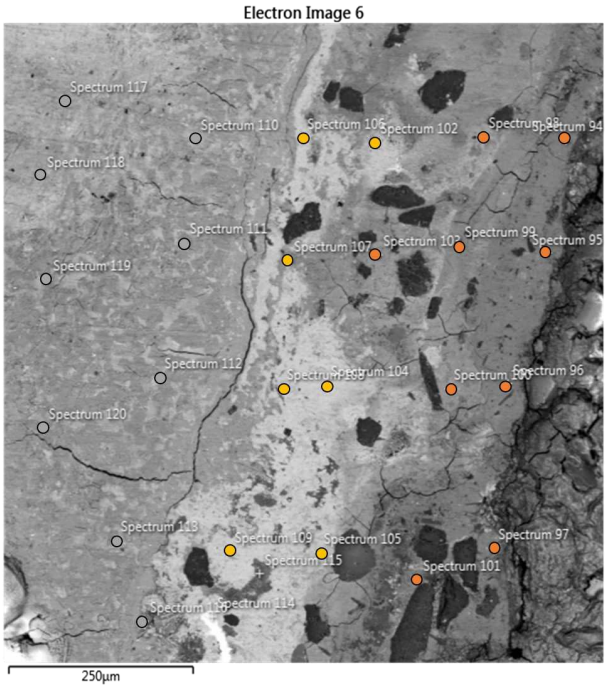

Fig. A17. Graphs and BSE image of Site 6, Slice 1.2.

Table A14. EDS analysis of Site 8, Slice 1.2.

Spectrum Label	O	Na	Mg	Al	Si	P	S	Cl	K	Ca	Ti	Cr	Fe	Zn	Total
Slice 1.2, Site 8, Zone 1	Cement paste														
Spectrum 121	27,00	0,27	0,00	0,09	0,08	0,00	6,27	7,25	0,00	3,36	0,07	0,20	55,40	0,00	100,00
Spectrum 122	21,86	0,92	0,02	0,11	0,20	0,24	0,93	8,33	0,00	0,00	0,04	1,00	66,35	0,00	100,00
Spectrum 123	23,39	1,99	0,04	0,09	0,20	0,12	1,94	5,35	0,00	0,17	0,10	0,42	66,19	0,00	100,00
Spectrum 124	22,82	1,92	0,05	0,09	0,04	0,05	1,54	5,29	0,03	0,20	0,01	0,28	67,66	0,00	100,00
Spectrum 125	21,62	0,00	0,02	0,00	0,11	0,05	0,16	4,39	0,02	0,03	0,00	0,40	73,20	0,00	100,00
Spectrum 127	22,25	1,05	0,00	0,04	0,08	0,09	0,65	4,07	0,01	0,00	0,02	0,55	71,19	0,00	100,00
Spectrum 128	26,49	0,78	0,01	0,00	0,09	0,11	5,32	4,99	0,04	0,83	0,07	0,42	60,86	0,00	100,00
Spectrum 129	32,86	1,15	0,10	0,00	0,10	0,14	11,32	2,52	0,00	2,45	0,00	0,25	49,12	0,00	100,00
Slice 1.2, Site 8, Zone 2	Cl- rich spots														
Spectrum 126	20,81	0,00	0,00	0,09	0,13	0,15	1,46	14,16	0,00	0,12	0,10	0,30	62,68	0,00	100,00
Spectrum 130	23,32	0,00	0,21	1,03	3,18	0,54	5,61	34,23	0,00	0,00	0,14	2,04	29,71	0,00	100,00
Spectrum 135	20,56	0,00	0,10	0,18	0,31	0,76	0,44	15,18	0,00	0,20	0,07	2,25	59,95	0,00	100,00
Spectrum 143	19,21	0,01	0,09	0,08	0,62	0,02	0,33	17,40	0,06	0,00	0,03	0,07	62,03	0,05	100,00
Slice 1.2, Site 8, Zone 3	Iron														
Spectrum 132	22,67	0,00	0,02	0,02	0,32	0,09	0,10	0,09	0,00	0,08	0,00	0,14	76,46	0,00	100,00
Spectrum 133	24,40	0,05	0,00	0,05	0,32	0,03	2,11	0,66	0,03	0,03	0,00	0,21	72,11	0,00	100,00
Spectrum 134	23,00	0,00	0,00	0,06	0,52	0,20	0,89	3,17	0,00	0,07	0,00	0,47	71,64	0,00	100,00
Spectrum 136	22,75	0,38	0,01	0,05	0,46	0,05	0,15	0,44	0,05	0,03	0,14	0,00	75,49	0,00	100,00
Spectrum 137	22,59	0,01	0,09	0,01	0,28	0,07	0,04	0,04	0,00	0,10	0,01	0,07	76,68	0,00	100,00
Spectrum 138	26,86	0,00	0,00	0,09	0,34	0,04	4,65	0,43	0,00	0,00	0,01	0,14	67,35	0,09	100,00
Spectrum 139	22,56	0,00	0,00	0,01	0,24	0,06	0,10	0,07	0,00	0,05	0,00	0,08	76,63	0,19	100,00
Spectrum 140	22,53	0,00	0,01	0,00	0,24	0,09	0,02	0,00	0,00	0,00	0,03	0,07	77,00	0,00	100,00
Spectrum 141	23,06	0,00	0,05	0,02	0,66	0,07	0,31	0,16	0,04	0,00	0,00	0,10	75,51	0,01	100,00
Spectrum 142	22,56	0,00	0,01	0,01	0,25	0,11	0,02	0,01	0,06	0,00	0,03	0,15	76,74	0,06	100,00
Spectrum 144	22,66	0,00	0,04	0,05	0,24	0,13	0,08	0,03	0,02	0,08	0,00	0,10	76,56	0,01	100,00
Spectrum 145	22,71	0,00	0,06	0,04	0,37	0,01	0,46	1,40	0,00	0,11	0,00	0,14	74,71	0,00	100,00

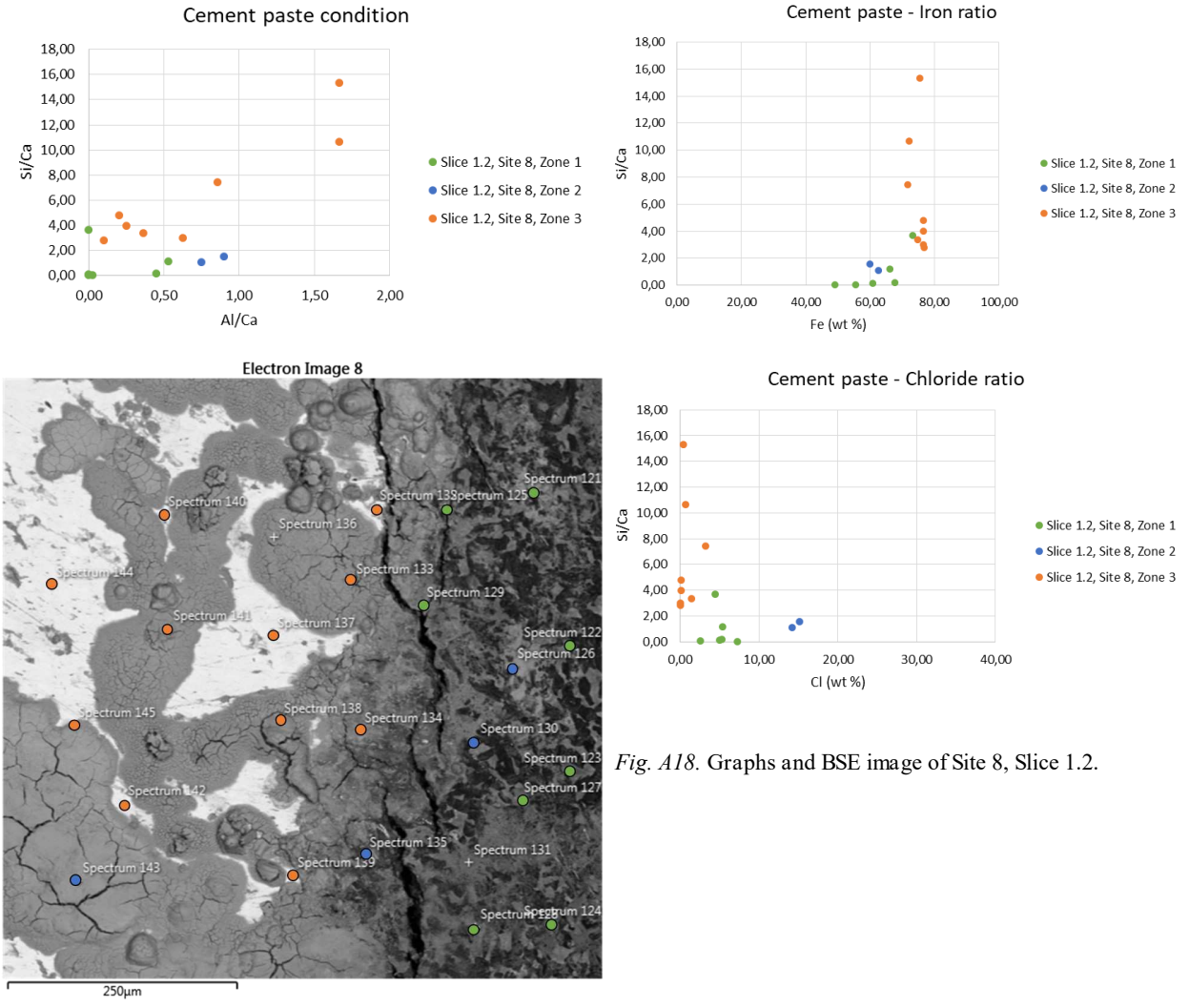

Fig. A18. Graphs and BSE image of Site 8, Slice 1.2.

Table A15. EDS analysis of Site 9, Slice 1.2.

Spectrum Label	O	Na	Mg	Al	Si	P	S	Cl	K	Ca	Ti	Cr	Fe	Zn	Total
Slice 1.2, Site 9, Zone 1		**Iron**													
Spectrum 146	22,55	0,00	0,01	0,00	0,27	0,10	0,02	0,03	0,00	0,01	0,00	0,06	76,94	0,00	100,00
Spectrum 147	22,67	0,20	0,00	0,00	0,29	0,05	0,16	0,02	0,02	0,05	0,00	0,09	76,45	0,00	100,00
Spectrum 148	22,56	0,05	0,00	0,06	0,28	0,06	0,01	0,00	0,02	0,00	0,02	0,06	76,89	0,00	100,00
Spectrum 149	22,62	0,00	0,00	0,00	0,34	0,05	0,06	0,00	0,02	0,01	0,03	0,15	76,71	0,00	100,00
Spectrum 150	22,70	0,00	0,05	0,00	0,48	0,06	0,09	0,28	0,00	0,08	0,02	0,14	76,10	0,00	100,00
Spectrum 151	22,61	0,03	0,00	0,03	0,16	0,08	0,21	0,25	0,00	0,00	0,02	0,06	76,55	0,00	100,00
Spectrum 152	23,78	0,00	0,05	0,04	1,29	0,03	0,45	0,17	0,01	2,39	0,01	0,07	71,62	0,09	100,00
Spectrum 153	23,40	0,00	0,10	0,06	1,21	0,01	0,29	0,25	0,08	0,53	0,00	0,09	73,96	0,04	100,00
Spectrum 154	22,74	0,05	0,03	0,13	0,32	0,07	0,02	0,09	0,00	1,45	0,00	0,11	75,01	0,00	100,00
Spectrum 155	22,60	0,01	0,00	0,10	0,13	0,04	0,03	0,03	0,00	1,30	0,07	0,10	75,58	0,01	100,00
Spectrum 157	23,08	0,00	0,00	0,06	0,77	0,03	0,08	0,00	0,01	1,86	0,00	0,10	74,01	0,00	100,00
Slice 1.2, Site 9, Zone 2		**Cement paste**													
Spectrum 158	40,27	0,01	2,83	3,73	16,66	0,22	1,59	0,41	0,00	31,28	0,23	0,00	2,76	0,00	100,00
Spectrum 159	37,21	0,14	0,38	1,78	15,65	0,13	0,75	0,23	0,05	31,97	0,15	0,10	11,46	0,00	100,00
Spectrum 161	37,06	0,03	0,34	0,89	15,82	0,02	0,57	0,53	0,08	38,09	0,05	0,07	6,46	0,00	100,00
Spectrum 162	38,06	0,23	3,20	2,39	15,18	0,04	0,51	0,64	0,10	37,01	0,17	0,11	2,36	0,00	100,00
Spectrum 163	36,08	0,05	0,23	0,73	15,32	0,04	0,34	0,25	0,04	33,62	0,00	0,09	13,19	0,02	100,00
Spectrum 164	39,95	0,00	0,45	0,66	20,58	0,11	0,43	0,41	0,10	36,63	0,00	0,00	0,54	0,14	100,00
Spectrum 165	46,28	1,25	0,03	9,92	29,92	0,00	0,00	0,10	10,17	0,84	0,18	0,06	1,25	0,00	100,00
Spectrum 166	40,88	0,20	1,87	5,22	19,20	0,31	0,59	1,90	0,03	28,27	0,14	0,00	1,38	0,00	100,00

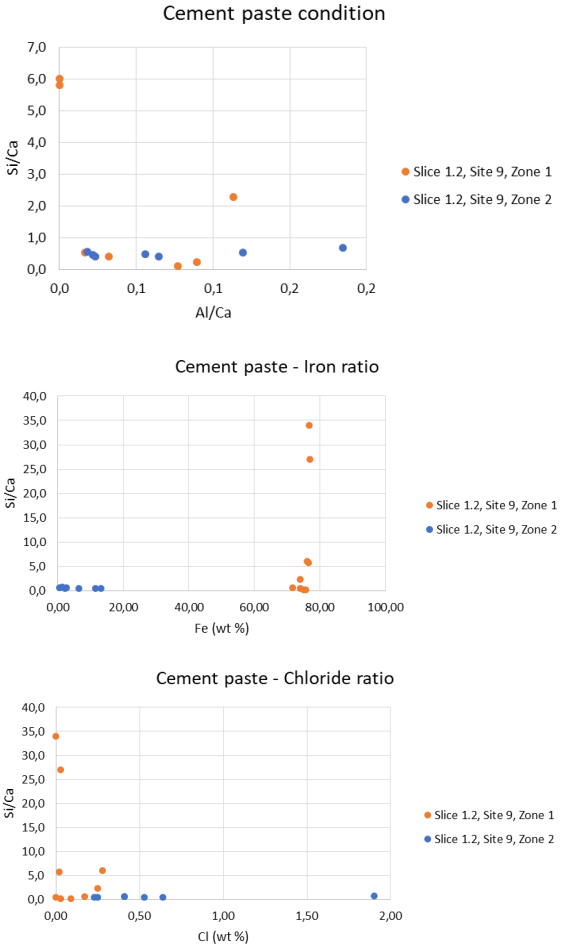

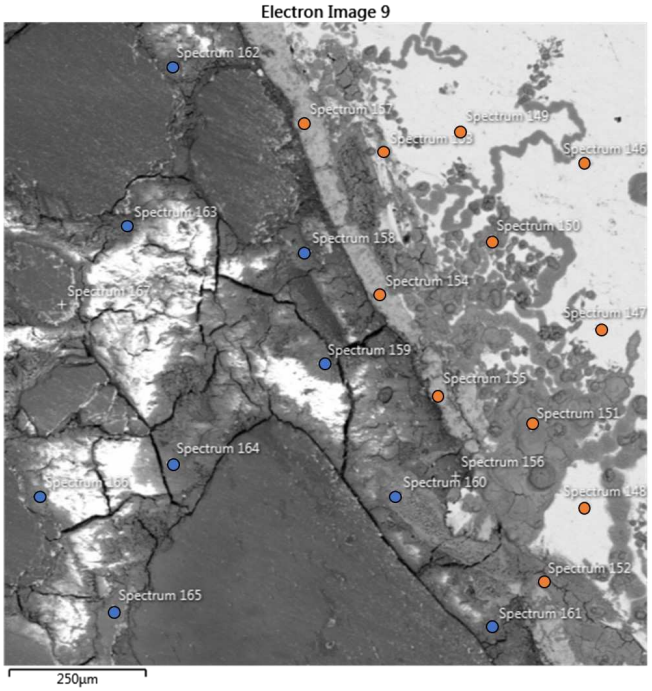

Fig. A19. Graphs and BSE image of Site 9, Slice 1.2.

Table A16. EDS analysis of Site 11, Slice 1.2.

Spectrum Label	O	Na	Mg	Al	Si	P	S	Cl	K	Ca	Ti	Cr	Fe	Zn	Total
Slice 1.2, Site 11, Zone 1	**Iron**														
Spectrum 168	22,59	0,01	0,00	0,03	0,31	0,06	0,03	0,00	0,03	0,00	0,02	0,15	76,77	0,00	100,00
Spectrum 169	22,56	0,01	0,00	0,09	0,28	0,06	0,00	0,03	0,05	0,07	0,00	0,17	76,68	0,00	100,00
Spectrum 170	22,77	0,08	0,04	0,05	0,30	0,09	0,09	0,01	0,00	0,93	0,00	0,22	75,41	0,00	100,00
Spectrum 171	22,62	0,09	0,02	0,08	0,13	0,00	0,04	0,05	0,00	1,67	0,10	0,10	75,11	0,00	100,00
Spectrum 172	23,29	0,26	0,00	0,09	0,98	0,06	0,06	0,10	0,04	2,33	0,01	0,18	72,59	0,00	100,00
Spectrum 173	22,89	0,07	0,06	0,00	0,57	0,07	0,11	0,13	0,00	0,71	0,00	0,27	75,12	0,00	100,00
Spectrum 174	23,05	0,14	0,04	0,07	0,82	0,06	0,08	0,10	0,09	0,82	0,00	0,14	74,59	0,00	100,00
Spectrum 175	22,53	0,14	0,00	0,00	0,21	0,00	0,10	0,16	0,04	0,58	0,01	0,08	76,15	0,00	100,00
Spectrum 176	22,57	0,03	0,04	0,00	0,32	0,05	0,02	0,05	0,00	0,13	0,00	0,14	76,65	0,00	100,00
Spectrum 177	22,48	0,00	0,03	0,01	0,24	0,02	0,01	0,00	0,00	0,08	0,00	0,11	76,95	0,07	100,00
Spectrum 178	23,13	0,00	0,09	0,05	1,04	0,01	0,03	0,22	0,00	1,40	0,00	0,16	73,76	0,11	100,00
Spectrum 179	22,74	0,00	0,03	0,08	0,39	0,12	0,03	0,00	0,00	0,34	0,00	0,13	76,15	0,00	100,00
Slice 1.2, Site 11, Zone 2	**Cement paste with high Fe**														
Spectrum 180	32,08	0,30	0,47	0,47	7,43	0,08	0,32	0,82	0,04	48,95	0,16	0,00	8,87	0,00	100,00
Spectrum 181	36,69	1,36	0,61	1,70	14,55	0,00	0,82	0,36	0,53	35,23	0,00	0,00	8,05	0,11	100,00
Spectrum 182	37,44	1,76	1,27	1,68	17,11	0,00	0,20	0,21	0,66	28,33	0,03	0,02	11,14	0,13	100,00
Spectrum 184	35,04	0,51	0,64	1,15	11,33	0,00	0,88	0,29	0,18	42,61	0,11	0,00	7,23	0,05	100,00
Spectrum 185	27,65	0,17	0,02	0,26	1,69	0,02	0,10	0,53	0,56	47,52	0,00	0,01	21,48	0,00	100,00

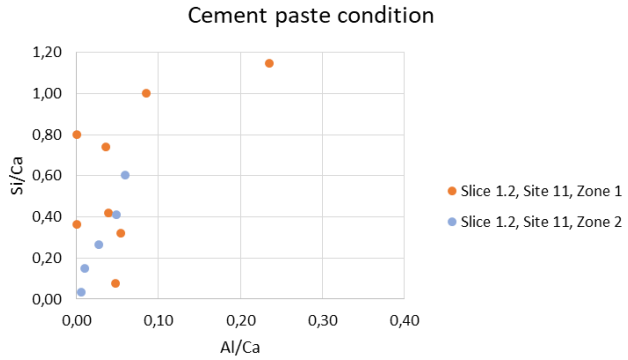

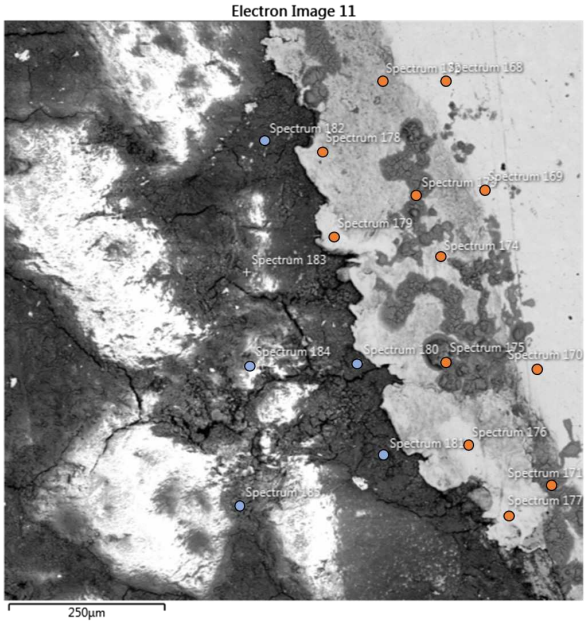

Fig. A20. Graphs and BSE image of Site 11, Slice 1.2.

Table A17. EDS analysis of Site 13, Slice 1.2.

Spectrum Label	O	Na	Mg	Al	Si	P	S	Cl	K	Ca	Ti	Cr	Fe	Zn	Total
Slice 1.2, Site 13, cement paste															
Spectrum 186	38,99	1,10	0,74	1,93	18,75	0,10	0,13	0,74	0,36	34,75	0,23	0,03	2,16	0,00	100,00
Spectrum 187	38,56	0,73	5,70	3,27	15,15	0,22	0,72	1,62	0,21	28,80	0,09	0,15	4,60	0,17	100,00
Spectrum 188	39,05	0,48	0,69	1,65	17,98	0,51	0,29	0,41	0,23	37,59	0,03	0,00	1,09	0,00	100,00
Spectrum 189	38,79	2,55	2,41	3,66	16,51	0,12	0,35	0,18	1,03	30,69	0,15	0,00	3,49	0,07	100,00
Spectrum 190	37,13	0,66	1,97	1,51	15,60	0,05	0,17	1,74	0,31	37,82	0,39	0,00	2,45	0,19	100,00
Spectrum 191	38,28	0,77	1,83	2,48	16,55	0,16	0,14	0,76	0,30	35,91	0,35	0,00	2,46	0,00	100,00
Spectrum 192	38,24	0,34	1,17	1,81	16,64	0,07	0,37	0,45	0,01	38,58	0,14	0,05	2,11	0,00	100,00
Spectrum 193	39,47	1,10	0,50	4,72	17,71	0,07	0,23	0,57	0,41	32,29	0,35	0,00	2,58	0,00	100,00
Spectrum 194	38,72	0,17	0,99	1,55	18,06	0,03	0,13	0,35	0,02	38,54	0,05	0,00	1,32	0,08	100,00
Spectrum 195	39,68	0,78	3,06	4,17	17,13	0,08	0,51	0,44	0,23	31,11	0,09	0,00	2,57	0,13	100,00
Spectrum 196	39,71	1,53	0,77	2,02	19,68	0,11	0,14	0,27	0,40	34,00	0,08	0,12	1,10	0,07	100,00
Spectrum 197	40,27	1,84	0,38	1,80	21,16	0,02	0,15	0,31	0,42	32,59	0,00	0,07	0,98	0,00	100,00
Spectrum 198	39,43	3,17	0,61	2,29	19,32	0,00	0,20	0,18	1,13	32,24	0,12	0,10	1,19	0,01	100,00

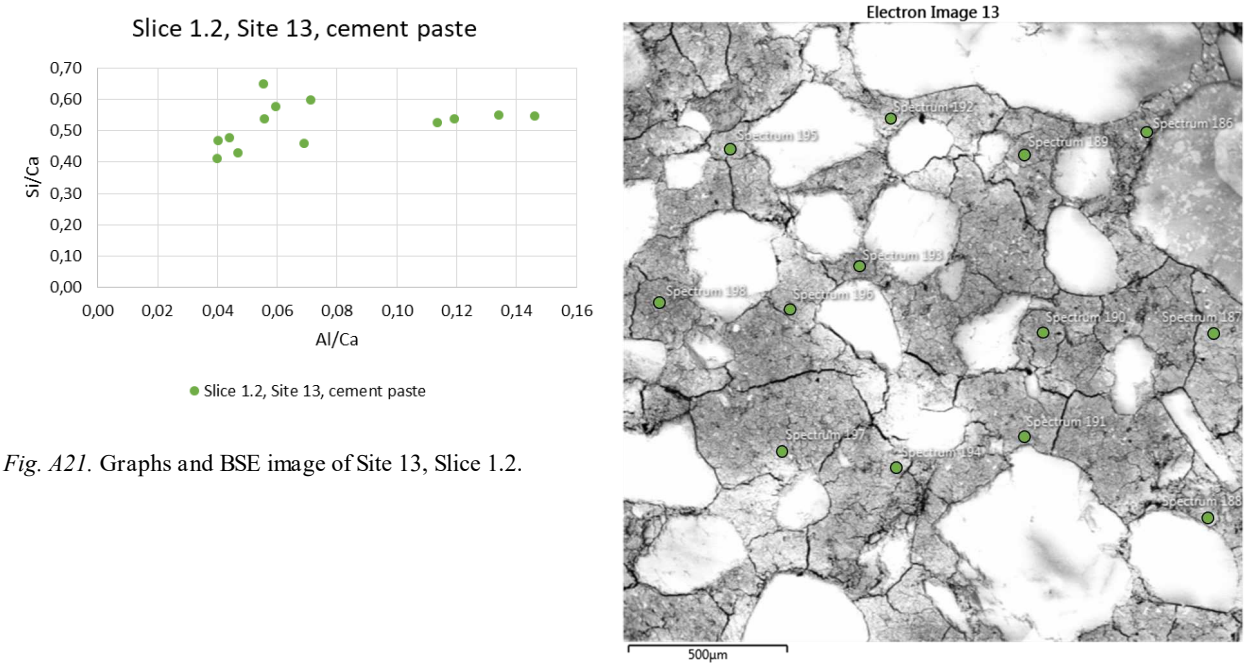

Fig. A21. Graphs and BSE image of Site 13, Slice 1.2.

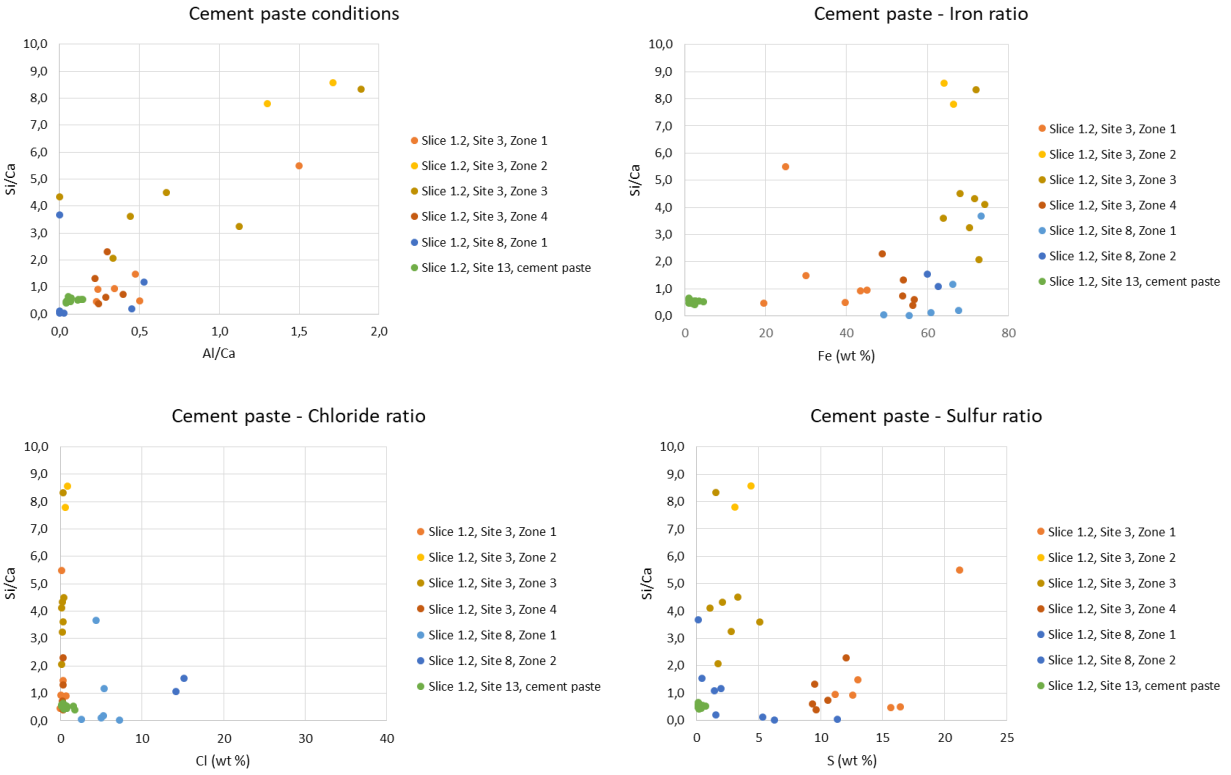

Fig. A22. Comparison of cement paste condition and element ratios between Sites 3, 8, and 13 in Slice 1.2.

Table A18. EDS analysis of Site 3, Slice 2.

Spectrum Lable	O	Na	Mg	Al	Si	P	S	Cl	K	Ca	Ti	Cr	Fe	Zn	Total:
Slice 2, Site 3, Zone 1															
Spectrum 153	24,38	0,40	0,53	0,10	0,93	0,01	1,16	0,15	0,00	2,51	0,00	0,02	69,42	0,40	100,00
Spectrum 154	24,57	0,38	0,85	0,04	1,10	0,06	1,12	0,17	0,00	2,45	0,09	0,00	68,53	0,63	100,00
Spectrum 155	25,00	0,85	0,87	0,06	0,83	0,03	1,83	0,09	0,00	1,66	0,06	0,11	67,47	1,13	100,00
Spectrum 156	24,74	1,39	0,72	0,07	1,07	0,02	1,32	0,07	0,01	2,61	0,00	0,05	67,40	0,54	100,00
Spectrum 157	24,37	0,29	0,70	0,08	0,91	0,08	1,05	0,20	0,00	2,88	0,04	0,00	68,65	0,74	100,00
Slice 2, Site 3, Zone 2															
Spectrum 158	26,07	0,28	1,97	0,04	1,41	0,06	1,82	0,31	0,00	7,02	0,00	0,00	59,74	1,27	100,00
Spectrum 159	26,03	0,45	1,47	0,02	1,62	0,05	2,12	0,28	0,04	3,27	0,06	0,06	63,13	1,39	100,00
Spectrum 160	26,81	0,59	2,86	0,05	0,92	0,06	2,61	0,26	0,10	7,40	0,00	0,04	57,16	1,15	100,00
Spectrum 161	26,49	0,34	1,48	0,04	0,72	0,01	2,69	0,22	0,09	9,27	0,02	0,01	58,13	0,50	100,00
Spectrum 162	26,39	0,16	1,49	0,02	1,12	0,02	1,68	0,17	0,04	15,87	0,02	0,02	52,19	0,80	100,00
Spectrum 164	26,12	0,13	1,74	0,05	1,31	0,05	1,52	0,33	0,03	12,16	0,04	0,00	55,98	0,55	100,00
Spectrum 165	25,72	0,20	2,32	0,07	0,90	0,04	1,61	0,20	0,00	7,70	0,02	0,01	60,11	1,11	100,00
Spectrum 166	26,32	0,22	2,68	0,09	1,39	0,04	1,82	0,23	0,02	7,35	0,00	0,03	58,63	1,18	100,00
Spectrum 167	26,47	0,14	0,98	0,30	4,24	0,07	0,55	0,12	0,06	5,05	0,00	0,06	61,21	0,77	100,00
Spectrum 171	25,52	0,07	1,37	0,10	2,70	0,13	0,54	0,19	0,08	5,50	0,02	0,00	62,81	0,99	100,00
Slice 2, Site 3, Zone 3															
Spectrum 168	33,20	0,21	1,03	0,23	14,81	0,00	0,51	0,09	0,01	2,86	0,00	0,07	46,43	0,56	100,00
Spectrum 169	27,59	0,22	1,23	0,51	5,65	0,09	0,44	0,13	0,04	6,07	0,02	0,00	57,25	0,76	100,00
Spectrum 170	29,24	0,34	1,19	0,56	8,38	0,06	0,36	0,18	0,13	5,64	0,00	0,00	52,94	0,98	100,00
Spectrum 176	33,15	0,83	1,48	0,98	13,41	0,19	0,46	0,26	0,16	6,31	0,02	0,21	41,73	0,83	100,00
Spectrum 177	30,88	0,32	1,19	0,92	10,56	0,04	0,29	0,13	0,12	6,33	0,04	0,03	48,42	0,73	100,00
Slice 2, Site 3, Zone 4															
Spectrum 172	46,21	0,06	0,38	0,06	35,50	0,05	0,14	0,09	0,00	1,55	0,00	0,00	15,62	0,34	100,00
Spectrum 173	46,71	0,19	0,33	0,10	36,14	0,01	0,24	0,05	0,09	1,43	0,03	0,00	14,40	0,27	100,00
Spectrum 174	47,23	0,15	0,34	0,27	36,74	0,09	0,17	0,05	0,00	1,58	0,07	0,02	13,05	0,23	100,00
Spectrum 175	45,41	0,10	0,21	0,07	34,16	0,05	0,23	0,10	0,01	1,81	0,00	0,00	17,81	0,03	100,00
Spectrum 178	48,31	0,02	0,23	0,06	38,70	0,05	0,23	0,18	0,09	0,94	0,00	0,04	10,82	0,34	100,00
Spectrum 179	48,86	0,00	0,17	0,08	39,64	0,03	0,16	0,12	0,09	0,91	0,03	0,00	9,74	0,16	100,00

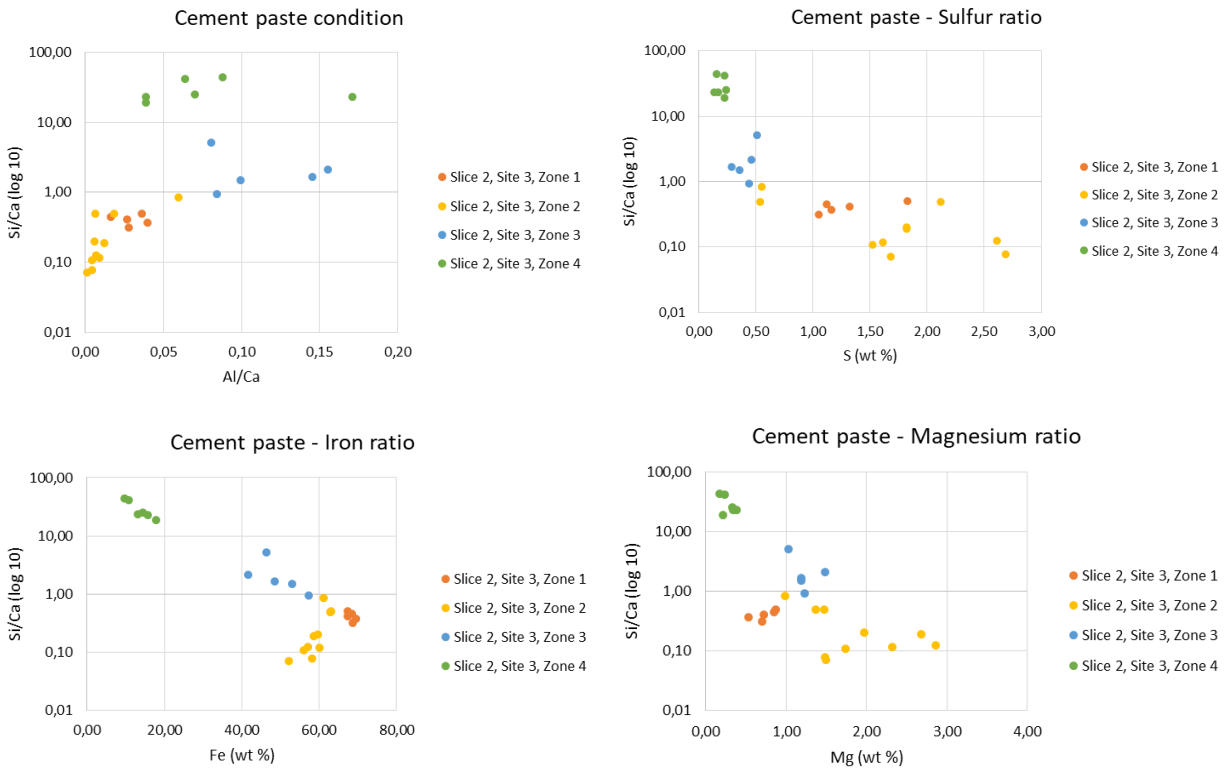

Fig. A23. Graphs of Site 3, Slice 1.2.

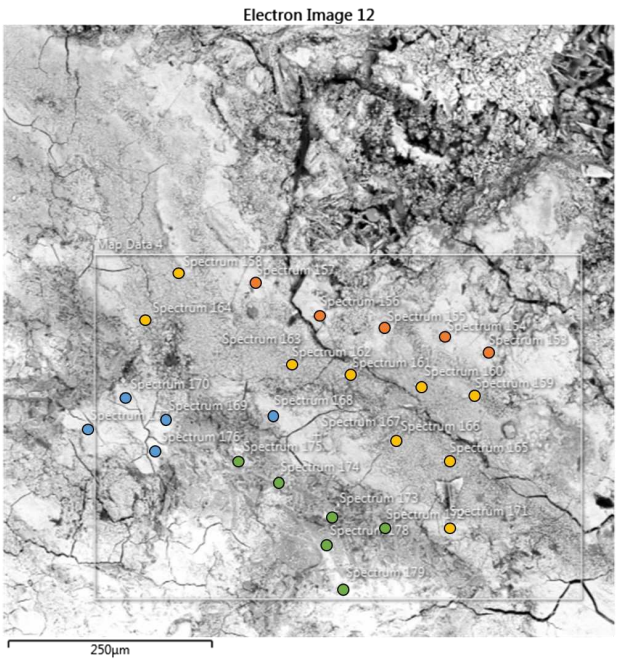

Fig. A24. Graphs and BSE image of Site 3, Slice 2.

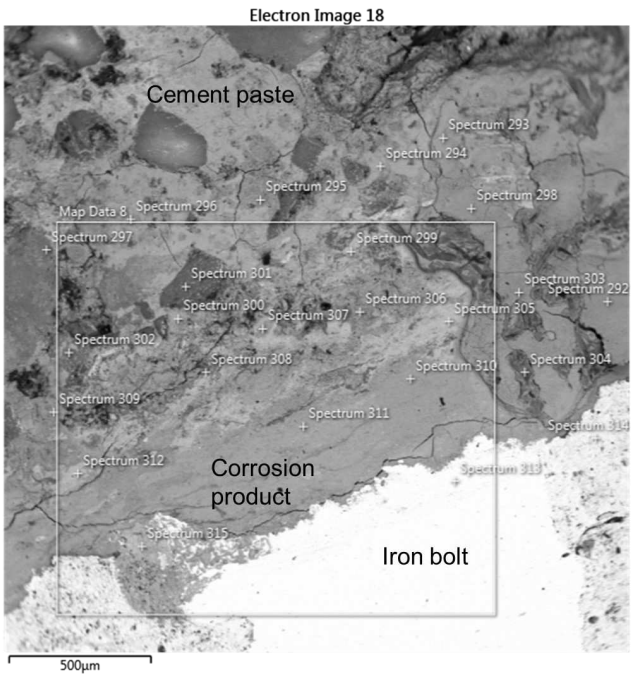

Fig. A25. BSE image of Site 9, Slice 2.

Table A19. EDS analysis of Site 9, Slice 2.

Spectrum Lable	O	Na	Mg	Al	Si	P	S	Cl	K	Ca	Ti	Cr	Fe	Zn	Total:
Spectrum 292	23,49	0,27	2,38	0,00	0,36	0,06	0,04	0,11	0,13	2,73	0,00	0,00	70,03	0,38	100,00
Spectrum 293	22,89	0,06	0,58	0,00	0,36	0,00	0,25	0,39	0,03	0,73	0,00	0,00	74,54	0,16	100,00
Spectrum 294	23,08	0,14	0,56	0,10	0,70	0,01	0,11	0,37	0,03	0,98	0,00	0,09	73,83	0,00	100,00
Spectrum 295	26,26	0,41	2,37	0,63	4,47	0,03	0,11	1,72	0,10	2,96	0,13	0,00	60,81	0,00	100,00
Spectrum 296	27,31	0,22	2,99	0,87	5,60	0,05	0,12	0,96	0,25	1,55	0,00	0,00	59,94	0,14	100,00
Spectrum 298	23,10	0,21	0,79	0,00	0,28	0,00	0,33	0,88	0,06	3,34	0,00	0,02	70,97	0,00	100,00
Spectrum 299	23,03	0,02	0,63	0,05	0,67	0,03	0,07	0,40	0,01	1,26	0,00	0,03	73,79	0,02	100,00
Spectrum 300	23,59	0,75	0,62	0,09	1,22	0,08	0,03	0,37	0,15	2,88	0,05	0,00	70,13	0,03	100,00
Spectrum 302	34,55	1,12	10,36	1,40	12,25	0,02	0,07	0,35	0,43	5,34	0,03	0,00	34,08	0,00	100,00
Spectrum 303	23,03	0,27	0,60	0,05	0,24	0,09	0,15	0,11	0,05	2,17	0,04	0,00	73,17	0,00	100,00
Spectrum 304	23,80	0,87	1,49	0,14	0,72	0,02	0,15	0,14	0,10	4,25	0,08	0,00	68,24	0,00	100,00
Spectrum 305	23,14	0,00	0,91	0,02	0,87	0,02	0,04	0,37	0,01	0,61	0,00	0,03	73,88	0,09	100,00
Spectrum 306	22,86	0,22	0,78	0,03	0,26	0,05	0,06	0,15	0,13	1,25	0,00	0,07	74,13	0,00	100,00
Spectrum 307	25,52	0,24	4,04	0,19	2,86	0,02	0,05	0,36	0,13	1,17	0,01	0,05	65,27	0,08	100,00
Spectrum 308	26,33	0,32	4,50	0,04	2,15	0,08	0,22	0,27	0,07	12,38	0,00	0,08	53,48	0,09	100,00
Spectrum 309	23,50	1,17	2,16	0,00	0,37	0,00	0,04	0,16	0,22	3,66	0,02	0,06	68,38	0,26	100,00
Spectrum 310	22,94	0,31	0,38	0,06	0,57	0,01	0,06	0,10	0,07	1,15	0,00	0,00	74,35	0,00	100,00
Spectrum 311	24,15	0,54	1,34	0,18	1,85	0,00	0,14	0,17	0,07	0,77	0,00	0,04	70,75	0,00	100,00
Spectrum 312	23,41	0,21	0,76	0,08	1,13	0,04	0,03	0,09	0,06	0,86	0,00	0,06	73,25	0,03	100,00
Spectrum 315	22,37	0,06	0,02	0,00	0,05	0,05	0,03	0,09	0,01	0,07	0,00	0,00	77,25	0,00	100,00

Table A20. EDS analysis of Site 10, Slice 2.

Spectrum Lable	O	Na	Mg	Al	Si	P	S	Cl	K	Ca	Ti	Cr	Fe	Zn	Total:
Slice 2, Site 10, Zone 1	iron														
Spectrum 316	22,37	0,04	0,01	0,00	0,05	0,02	0,04	0,00	0,01	0,07	0,00	0,04	77,35	0,00	100,00
Spectrum 317	23,90	0,11	0,46	0,07	1,75	0,06	0,09	0,01	0,05	1,96	0,00	0,00	71,54	0,00	100,00
Slice 2, Site 10, Zone 2	corrosion product														
Spectrum 318	23,91	0,35	0,75	0,06	1,79	0,03	0,10	0,05	0,27	1,12	0,00	0,07	71,45	0,06	100,00
Spectrum 319	25,65	0,87	0,46	0,03	4,38	0,12	0,00	0,00	0,32	2,18	0,06	0,03	65,88	0,00	100,00
Spectrum 320	23,83	0,33	0,43	0,07	1,93	0,00	0,07	0,02	0,27	0,88	0,00	0,00	71,93	0,23	100,00
Spectrum 321	25,07	0,54	0,42	0,08	3,09	0,03	0,03	0,07	0,43	6,35	0,02	0,07	63,70	0,12	100,00
Spectrum 322	23,67	0,69	0,29	0,07	1,60	0,02	0,10	0,09	0,22	1,02	0,01	0,12	72,08	0,00	100,00
Spectrum 323	24,60	0,20	0,56	0,07	2,94	0,00	0,03	0,04	0,30	1,82	0,07	0,01	68,99	0,35	100,00
Spectrum 324	24,84	0,67	0,45	0,03	3,34	0,03	0,04	0,03	0,39	1,82	0,00	0,00	68,36	0,00	100,00
Spectrum 325	25,16	0,72	1,21	0,00	3,31	0,06	0,21	0,00	0,41	1,13	0,00	0,01	67,78	0,00	100,00
Spectrum 326	23,24	0,32	0,12	0,03	1,15	0,04	0,07	0,02	0,23	0,75	0,00	0,02	74,01	0,01	100,00
Spectrum 330	40,05	6,01	0,77	6,19	21,23	0,00	0,05	0,00	0,57	3,07	0,02	0,12	21,85	0,06	100,00
Slice 2, Site 10, Zone 3	Cement paste														
Spectrum 327	36,53	1,01	0,80	4,01	13,28	0,12	0,04	0,05	3,49	38,44	0,14	0,03	1,97	0,10	100,00
Spectrum 328	29,80	1,07	0,66	0,40	2,32	0,05	0,00	0,12	0,43	63,48	0,07	0,00	1,61	0,00	100,00
Spectrum 329	37,67	0,44	0,74	0,39	18,07	0,21	0,05	0,04	0,83	32,61	0,04	0,00	8,86	0,05	100,00
Spectrum 333	31,77	0,28	0,29	1,07	5,99	0,06	0,03	0,04	1,84	56,92	0,00	0,00	1,71	0,01	100,00
Spectrum 334	35,57	0,67	0,67	0,19	12,80	0,17	0,10	0,08	0,26	49,15	0,00	0,00	0,35	0,00	100,00
Spectrum 335	36,65	1,67	1,04	1,94	14,04	0,17	0,02	0,07	1,08	42,42	0,00	0,00	0,90	0,00	100,00

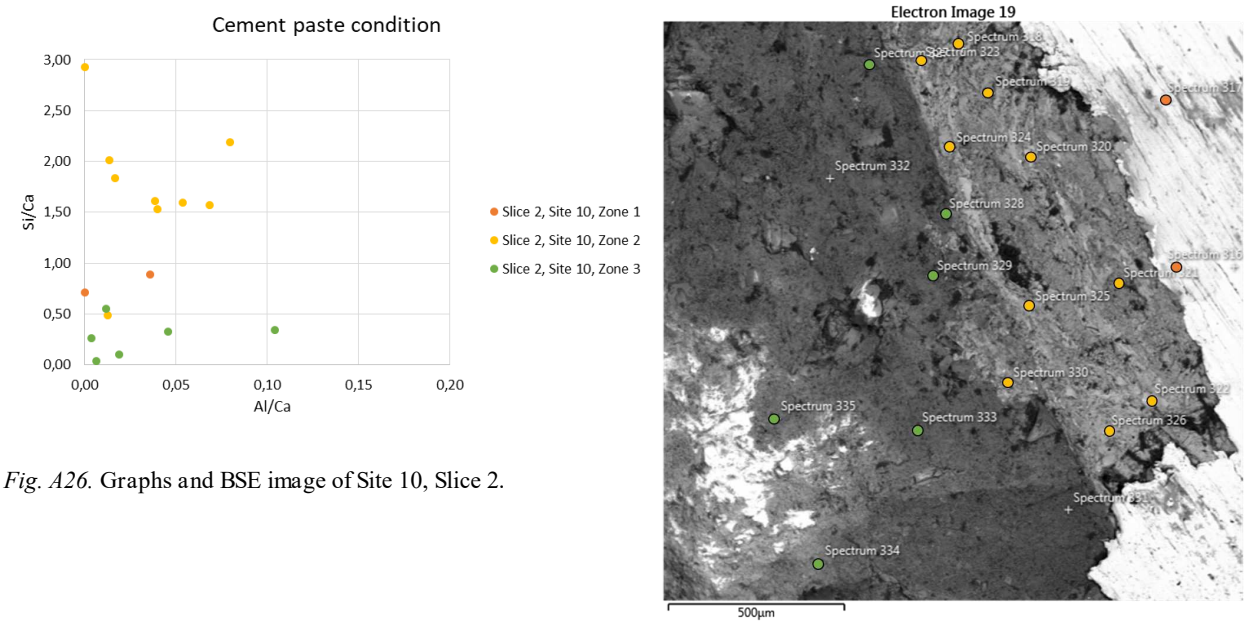

Fig. A26. Graphs and BSE image of Site 10, Slice 2.

Table A21. EDS analysis of Site 2, Slice 3.

Spectrum Label	O	Na	Mg	Al	Si	P	S	Cl	K	Ca	Ti	Cr	Fe	Zn	Total
Slice 3, Site 2, Zone 1		Cementpaste													
Spectrum 18	40,89	0,09	1,96	2,42	21,00	0,00	0,21	0,06	0,06	31,61	0,29	0,03	1,38	0,00	100,00
Spectrum 19	40,27	0,04	2,99	2,88	19,16	0,07	0,16	0,08	0,13	32,68	0,25	0,00	1,29	0,00	100,00
Spectrum 20	35,90	0,00	3,68	5,99	9,04	0,24	0,54	0,16	0,00	33,58	0,69	0,00	9,93	0,26	100,00
Spectrum 21	34,81	0,01	2,61	5,80	7,48	0,03	1,03	0,11	0,03	32,55	1,08	0,00	14,46	0,00	100,00
Spectrum 23	39,23	0,02	0,90	2,38	17,94	0,11	0,30	0,11	0,09	37,71	0,15	0,12	0,90	0,05	100,00
Spectrum 24	40,00	0,00	3,22	3,31	18,56	0,03	0,09	0,31	0,04	32,61	0,24	0,03	1,46	0,10	100,00
Spectrum 31	36,55	0,13	1,14	3,24	12,71	0,02	0,21	0,05	0,13	42,65	0,32	0,03	2,82	0,00	100,00
Slice 3, Site 2, Zone 2		White in cement paste			Ferrite?										
Spectrum 22	34,85	0,05	4,12	10,59	5,09	0,02	0,19	0,05	0,02	30,69	0,60	0,02	13,62	0,09	100,00
Spectrum 25	35,39	0,02	8,38	9,86	4,83	0,00	0,29	0,05	0,03	29,26	0,28	0,00	11,58	0,02	100,00
Spectrum 27	34,35	0,16	2,85	13,15	2,86	0,00	0,03	0,01	0,07	34,27	0,77	0,00	11,44	0,03	100,00
Spectrum 28	34,28	0,12	3,98	12,26	3,21	0,00	0,00	0,01	0,25	32,99	0,45	0,01	12,19	0,24	100,00

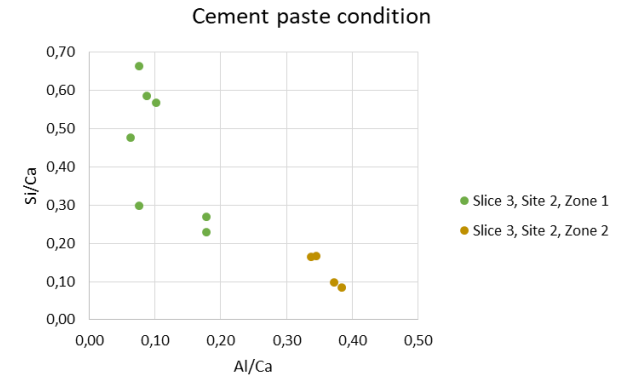

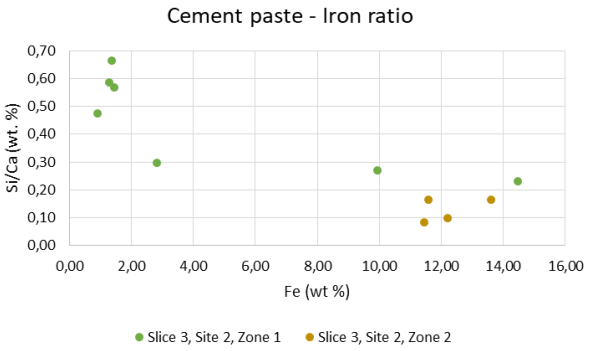

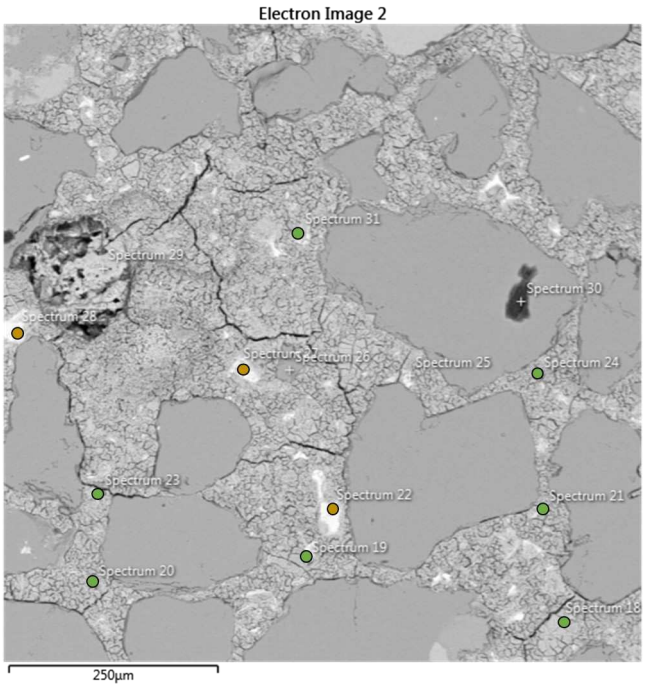

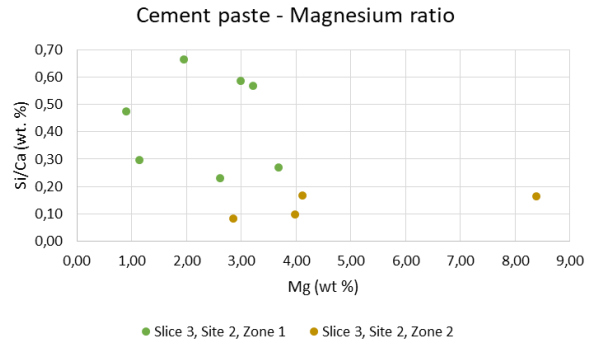

Fig. A27. Graphs and BSE image of Site 2 (the cement paste mending), Slice 3.

Table A22. EDS analysis of Site 3, Slice 3.

Spectrum Label	O	Na	Mg	Al	Si	P	S	Cl	K	Ca	Ti	Cr	Fe	Zn	Total
Slice 3, Site 3, Zone 1		Cement paste													
Spectrum 32	40,55	0,03	2,24	1,77	20,92	0,05	0,18	0,77	0,03	32,07	0,22	0,05	1,13	0,00	100,00
Spectrum 33	34,78	0,00	0,40	2,75	10,58	0,00	0,43	0,17	0,03	43,03	0,00	0,00	7,31	0,52	100,00
Spectrum 34	36,13	0,05	0,79	2,72	11,89	0,05	0,54	0,22	0,07	45,52	0,00	0,13	1,84	0,04	100,00
Spectrum 37	36,40	0,00	2,31	2,42	11,55	0,11	0,86	0,33	0,00	43,80	0,15	0,00	1,92	0,15	100,00
Spectrum 38	35,10	0,00	1,21	4,50	9,26	0,03	0,94	0,15	0,07	37,62	0,24	0,10	10,75	0,03	100,00
Slice 3, Site 3, Zone 2		Light grey in BSE-image													
Spectrum 39	31,63	0,00	0,35	0,89	9,81	0,00	0,58	0,12	0,00	20,90	0,07	0,16	35,08	0,40	100,00
Spectrum 42	29,04	0,03	0,17	0,58	7,09	0,03	0,51	0,24	0,12	14,33	0,09	0,09	47,54	0,14	100,00
Spectrum 46	31,36	0,00	0,98	1,40	10,04	0,03	0,42	0,85	0,00	14,25	0,13	0,03	40,27	0,24	100,00
Spectrum 44	24,41	0,00	0,19	0,20	2,67	0,07	0,15	1,71	0,07	4,94	0,00	0,12	65,48	0,00	100,00
Spectrum 56	23,38	0,09	0,13	0,07	0,62	0,07	0,15	1,71	0,07	4,94	0,00	0,12	65,48	0,00	100,00
Spectrum 47	24,72	0,10	0,00	0,36	3,70	0,04	0,13	0,13	0,07	7,15	0,00	0,35	67,85	0,00	100,00
Spectrum 51	28,52	0,00	0,00	0,37	8,89	0,07	0,17	1,95	0,02	0,85	0,00	0,07	68,00	0,00	100,00
Spectrum 48	22,67	0,00	0,02	0,11	0,27	0,00	0,00	0,37	0,00	2,96	0,00	0,00	58,52	0,37	100,00
Spectrum 50	24,27	0,18	0,07	0,34	2,09	0,09	0,16	0,40	0,00	0,44	0,04	0,05	75,46	0,27	100,00
Spectrum 53	23,00	0,12	0,04	0,12	0,92	0,09	0,37	0,39	0,00	1,10	0,00	0,20	70,79	0,11	100,00
Slice 3, Site 3, Zone 3		White in BSE-image													
Spectrum 40	26,05	0,10	0,14	0,41	4,96	0,02	0,16	0,35	0,14	2,32	0,03	0,17	65,15	0,00	100,00
Spectrum 45	24,96	0,00	0,14	0,38	3,54	0,02	0,16	0,35	0,14	2,32	0,03	0,17	65,15	0,00	100,00
Spectrum 52	23,51	0,24	0,05	0,03	1,40	0,03	0,22	0,83	0,11	1,25	0,00	0,10	68,29	0,14	100,00
Spectrum 54	22,84	0,04	0,00	0,07	0,53	0,14	0,03	0,07	0,03	2,74	0,00	0,42	71,33	0,00	100,00
Spectrum 55	22,96	0,03	0,02	0,08	0,54	0,14	0,11	0,11	0,05	0,39	0,00	0,25	75,47	0,02	100,00

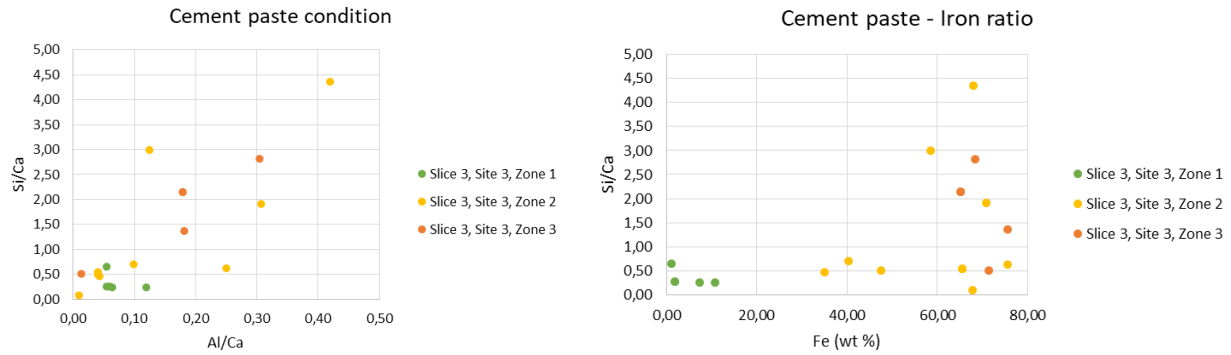

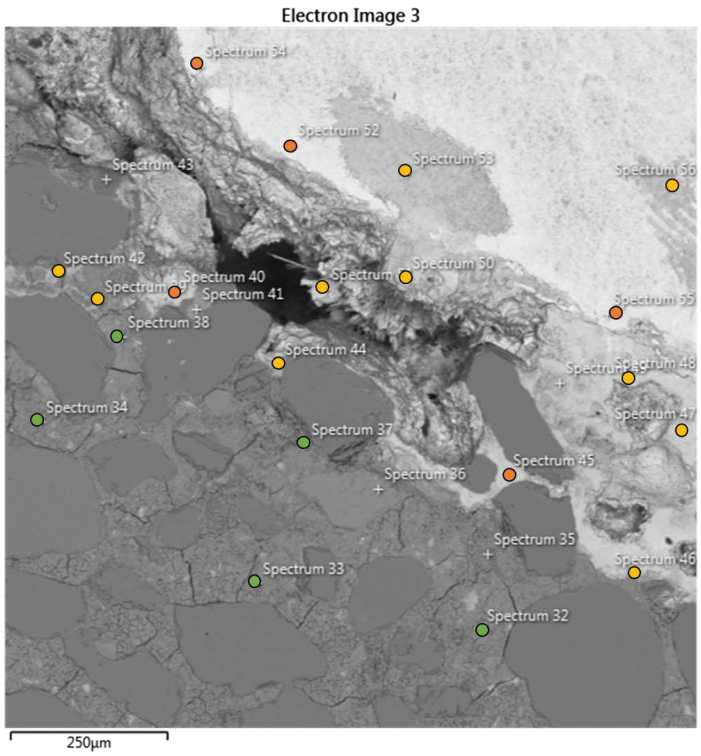

Fig. A28. Graphs and BSE image of Site 3, Slice 3.

Table A23. EDS analysis of Site 6, Slice 3.

Spectrum Label	O	Na	Mg	Al	Si	P	S	Cl	K	Ca	Ti	Cr	Fe	Zn	Total
Slice 3, Site 6, Zone 1	**Rings (light grey in BSE-image)**														
Spectrum 103	22,44	0,00	0,08	0,00	0,45	0,02	0,09	1,12	0,00	0,19	0,00	0,22	75,27	0,14	100,00
Spectrum 106	22,98	0,02	0,02	0,07	0,72	0,14	0,12	0,28	0,07	0,28	0,00	0,65	74,66	0,00	100,00
Spectrum 108	22,81	0,08	0,10	0,06	0,58	0,08	0,15	0,38	0,04	0,60	0,00	0,33	74,81	0,00	100,00
Spectrum 109	22,86	0,00	0,13	0,08	0,53	0,11	0,25	0,19	0,00	0,71	0,00	0,52	74,62	0,00	100,00
Spectrum 112	22,89	0,17	0,11	0,09	0,53	0,19	0,13	0,28	0,00	0,47	0,00	0,41	74,74	0,00	100,00
Spectrum 113	22,95	0,00	0,17	0,04	0,82	0,13	0,04	0,27	0,04	0,54	0,00	0,31	74,69	0,00	100,00
Spectrum 114	23,02	0,02	0,06	0,08	0,88	0,11	0,15	0,34	0,02	0,57	0,00	0,42	74,33	0,00	100,00
Spectrum 116	22,76	0,06	0,00	0,02	0,80	0,00	0,10	0,38	0,00	0,48	0,00	0,57	74,83	0,00	100,00
Spectrum 118	23,05	0,10	0,00	0,10	0,96	0,10	0,18	0,39	0,00	0,31	0,00	0,78	74,01	0,00	100,00
Spectrum 107	22,64	0,06	0,04	0,08	0,32	0,04	0,14	0,38	0,00	0,44	0,04	0,36	75,47	0,00	100,00
Slice 3, Site 6, Zone 2	**Rings (white in BSE-image)**														
Spectrum 101	22,70	0,04	0,02	0,04	0,47	0,05	0,07	0,14	0,05	0,64	0,00	0,32	75,46	0,00	100,00
Spectrum 102	22,59	0,29	0,00	0,00	0,37	0,02	0,11	0,14	0,06	0,94	0,00	0,28	75,19	0,00	100,00
Spectrum 105	22,82	0,00	0,06	0,02	0,43	0,09	0,30	0,35	0,02	0,09	0,06	0,30	75,47	0,00	100,00
Spectrum 111	23,17	0,18	0,00	0,02	0,63	0,13	0,71	0,22	0,00	0,38	0,05	0,40	74,12	0,00	100,00
Spectrum 115	22,66	0,00	0,15	0,00	0,40	0,09	0,09	0,17	0,00	0,19	0,00	0,28	75,91	0,06	100,00
Spectrum 119	22,93	0,00	0,09	0,00	0,74	0,13	0,09	0,13	0,02	0,26	0,00	0,28	75,32	0,00	100,00
Slice 3, Site 6, Zone 3	**Rings mixed**														
Spectrum 104	23,08	0,02	0,06	0,03	0,95	0,08	0,09	0,29	0,02	0,40	0,03	0,44	74,52	0,00	100,00
Spectrum 117	23,65	0,08	0,06	0,11	1,71	0,13	0,10	0,24	0,02	0,37	0,02	0,22	73,31	0,00	100,00
Spectrum 110	22,65	0,12	0,04	0,02	0,53	0,05	0,04	0,16	0,02	0,48	0,00	0,43	75,46	0,00	100,00
Spectrum 120	22,97	0,18	0,00	0,10	0,80	0,05	0,18	0,36	0,00	0,44	0,00	0,31	74,61	0,00	100,00
Slice 3, Site 6, Zone 4	**Altered cement paste**														
Spectrum 122	28,23	0,08	0,03	0,03	9,22	0,48	0,46	4,70	0,00	0,56	0,03	0,99	55,19	0,00	100,00
Spectrum 123	33,49	0,24	0,00	0,03	16,79	0,62	0,24	3,36	0,05	0,59	0,00	0,91	43,66	0,00	100,00
Spectrum 124	36,07	0,09	0,06	0,03	20,85	0,17	0,26	2,70	0,12	0,81	0,00	1,32	37,53	0,00	100,00
Spectrum 125	37,30	0,15	0,02	0,00	22,42	0,22	0,17	2,11	0,00	1,02	0,05	1,71	34,83	0,00	100,00
Spectrum 126	36,38	0,13	0,10	0,00	21,17	0,26	0,39	2,95	0,13	0,90	0,00	1,76	35,83	0,00	100,00
Spectrum 128	26,08	0,28	0,00	0,14	6,67	0,84	0,93	9,94	0,33	0,47	0,05	1,91	52,36	0,00	100,00
Spectrum 129	28,55	0,00	0,17	0,00	11,26	0,62	0,84	11,49	0,11	0,45	0,06	1,80	44,65	0,00	100,00
Spectrum 130	30,18	0,00	0,06	0,06	12,18	0,54	0,33	5,33	0,06	0,57	0,15	1,70	48,85	0,00	100,00
Spectrum 121	26,98	0,12	0,00	0,00	6,91	0,22	0,24	1,53	0,00	0,73	0,02	0,73	62,53	0,00	100,00

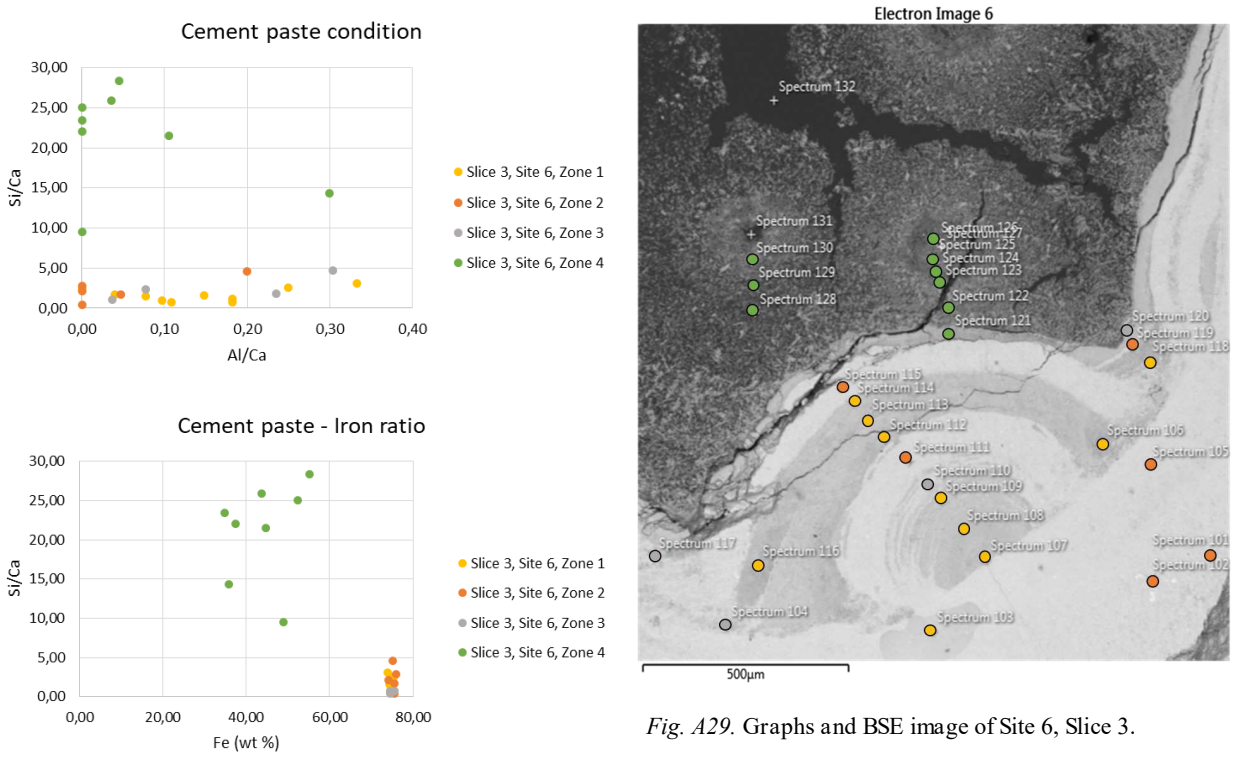

Fig. A29. Graphs and BSE image of Site 6, Slice 3.

Table A24. EDS analysis of Site 8, Slice 3.

Spectrum Label	O	Na	Mg	Al	Si	P	S	Cl	K	Ca	Ti	Cr	Fe	Zn	Total
Slice 3, Site 8, Zone 1	**White in BSE-image**														
Spectrum 136	23,53	0,00	0,09	0,09	1,36	0,36	0,04	0,22	0,09	0,09	0,02	0,23	73,88	0,00	100,00
Spectrum 142	22,55	0,13	0,08	0,04	0,25	0,00	0,09	0,08	0,04	0,08	0,02	0,13	76,29	0,23	100,00
Spectrum 148	22,57	0,04	0,00	0,08	0,30	0,00	0,13	0,08	0,00	0,08	0,02	0,06	76,62	0,00	100,00
Spectrum 154	22,70	0,10	0,00	0,00	0,36	0,10	0,16	0,10	0,00	0,16	0,00	0,10	76,19	0,03	100,00
Spectrum 157	22,72	0,00	0,00	0,06	0,43	0,09	0,11	0,06	0,06	0,09	0,03	0,00	76,24	0,11	100,00
Slice 3, Site 8, Zone 2	**Lightgrey in BSE-image**														
Spectrum 137	23,73	0,07	0,04	0,04	1,71	0,33	0,36	1,38	0,04	0,22	0,00	0,18	71,90	0,00	100,00
Spectrum 138	23,00	0,00	0,15	0,10	0,66	0,22	0,12	0,34	0,00	0,15	0,00	0,12	75,09	0,05	100,00
Spectrum 140	23,11	0,00	0,02	0,00	1,19	0,51	0,34	3,06	0,02	0,19	0,00	0,19	71,36	0,00	100,00
Spectrum 141	22,84	0,03	0,08	0,05	0,67	0,36	0,03	0,85	0,00	0,05	0,00	0,08	74,75	0,23	100,00
Spectrum 143	22,55	0,00	0,07	0,07	0,27	0,05	0,15	0,69	0,05	0,07	0,07	0,05	75,66	0,22	100,00
Spectrum 145	22,26	0,07	0,00	0,10	0,21	0,00	0,14	1,16	0,00	0,17	0,00	0,00	75,79	0,10	100,00
Spectrum 146	22,47	0,15	0,10	0,10	0,27	0,02	0,12	0,89	0,05	0,10	0,00	0,10	75,60	0,02	100,00
Spectrum 147	22,48	0,00	0,14	0,08	0,22	0,00	0,16	0,71	0,11	0,11	0,14	0,11	75,56	0,19	100,00
Spectrum 149	23,08	0,00	0,00	0,13	0,99	0,05	0,10	0,26	0,03	0,13	0,03	0,16	74,93	0,10	100,00
Spectrum 150	22,64	0,09	0,00	0,13	0,33	0,09	0,04	0,13	0,07	0,09	0,00	0,15	76,21	0,02	100,00
Spectrum 151	24,65	0,14	0,00	1,74	2,08	0,22	0,06	0,36	0,03	0,17	0,06	0,19	70,31	0,00	100,00
Spectrum 152	24,13	0,24	0,00	0,74	1,83	0,29	0,05	0,29	0,00	1,09	0,00	0,11	71,15	0,08	100,00
Spectrum 153	22,53	0,00	0,23	0,09	0,23	0,03	0,20	1,02	0,00	0,23	0,00	0,17	75,24	0,03	100,00
Spectrum 155	24,15	0,17	0,09	0,40	2,32	0,03	0,06	0,20	0,03	0,66	0,06	0,23	71,33	0,29	100,00
Spectrum 168	22,66	0,00	0,00	0,05	0,26	0,11	0,26	0,71	0,05	0,03	0,00	0,18	75,58	0,11	100,00
Slice 3, Site 8, Zone 3	**Cement paste**														
Spectrum 133	23,71	0,06	0,04	0,08	2,52	0,16	0,34	3,69	0,00	0,04	0,02	0,89	68,44	0,00	100,00
Spectrum 134	25,24	0,02	0,02	0,00	4,83	0,18	0,29	3,16	0,00	0,13	0,00	0,53	65,60	0,00	100,00
Spectrum 135	35,65	0,13	0,00	0,04	19,61	0,44	0,36	1,62	0,06	0,27	0,15	0,86	40,80	0,00	100,00
Spectrum 139	37,24	0,13	0,04	0,06	22,68	0,11	0,11	1,25	0,25	0,11	0,02	0,06	37,93	0,00	100,00
Slice 3, Site 8, Zone 4	**Cement paste - white in BSE-image**														
Spectrum 161	24,11	0,26	0,00	0,59	2,36	0,03	0,00	0,09	0,09	0,56	0,00	0,15	71,77	0,00	100,00
Spectrum 163	23,70	0,19	0,00	0,25	1,75	0,09	0,03	0,03	0,09	0,44	0,00	0,16	73,26	0,00	100,00
Spectrum 160	24,32	0,00	0,03	0,67	2,45	0,10	0,00	0,03	0,22	0,61	0,00	0,19	71,12	0,26	100,00
Slice 3, Site 8, Zone 5	**Cement paste - lighter grey in BSE-image**														
Spectrum 158	27,15	0,23	0,15	2,05	5,57	0,00	0,12	0,59	0,21	2,81	0,00	0,03	61,10	0,00	100,00
Spectrum 159	27,46	0,12	0,03	1,37	6,72	0,06	0,03	0,12	0,21	0,79	0,00	0,12	62,68	0,27	100,00
Spectrum 162	27,17	0,00	0,16	2,81	4,59	0,06	0,09	0,19	0,16	1,78	0,81	0,19	61,88	0,12	100,00
Spectrum 164	32,42	0,12	0,60	2,62	12,55	0,00	0,00	0,12	0,64	4,61	0,20	0,16	45,77	0,20	100,00
Spectrum 165	33,66	0,22	0,70	2,94	13,69	0,09	0,18	0,35	0,26	5,84	0,09	0,13	41,55	0,31	100,00
Slice 3, Site 8, Zone 6	**Cement paste - darkgrey in BSE-image**														
Spectrum 166	33,41	0,00	1,19	1,42	8,78	0,18	0,30	0,36	0,12	44,93	0,18	0,18	8,84	0,12	100,00
Spectrum 167	33,61	0,11	1,35	2,02	9,71	0,00	0,28	0,22	0,11	37,65	0,11	0,28	14,42	0,11	100,00

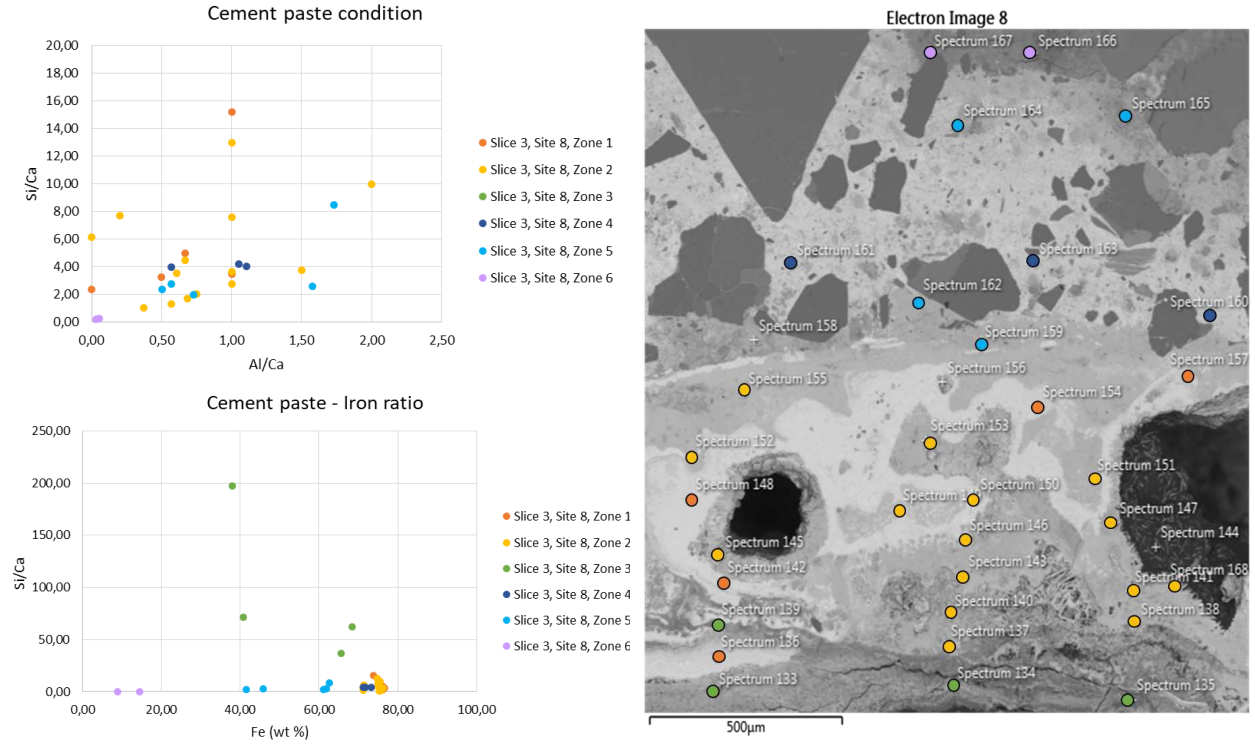

Fig. A30. Graphs and BSE image of Site 8, Slice 3.

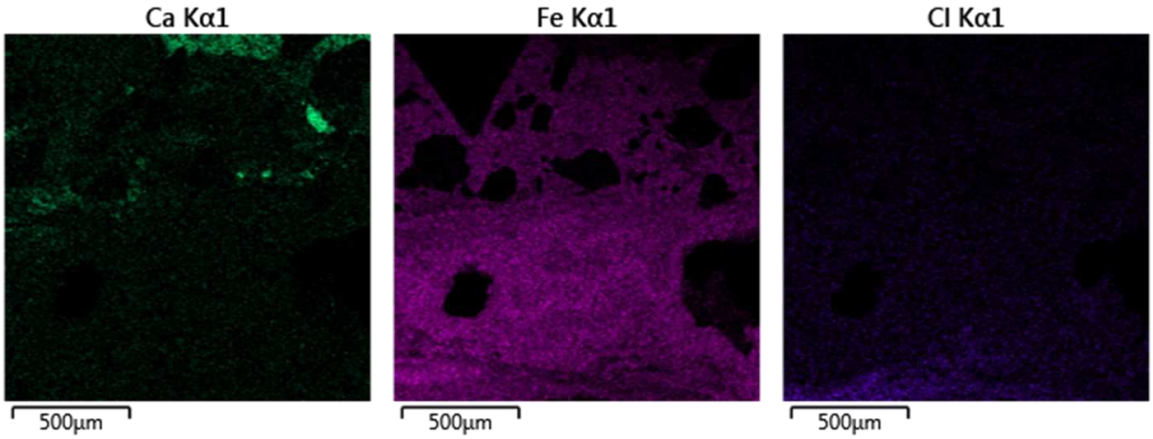

Fig. A31. Element maps of Site 8, Slice 3.

Table A25. EDS analysis of Site 12, Slice 3.

Spectrum Label	O	Na	Mg	Al	Si	P	S	Cl	K	Ca	Ti	Cr	Fe	Zn	Total
Slice 3, Site 12, Cement paste															
Spectrum 201	35,96	0,11	1,50	2,64	11,48	0,00	0,37	0,11	0,06	46,45	0,01	0,00	1,20	0,10	100,00
Spectrum 203	39,04	0,00	0,43	3,70	16,44	0,14	0,59	0,05	0,10	38,77	0,00	0,00	0,63	0,10	100,00
Spectrum 204	39,39	0,12	3,14	2,95	17,30	0,05	0,19	0,04	0,00	34,82	0,25	0,13	1,39	0,22	100,00
Spectrum 206	36,63	0,09	1,03	1,88	13,41	0,07	0,30	0,07	0,04	45,41	0,12	0,00	0,95	0,00	100,00
Spectrum 207	36,52	0,06	0,67	2,76	12,06	0,09	0,80	0,04	0,25	44,73	0,13	0,12	1,66	0,13	100,00
Spectrum 208	36,45	0,03	1,97	3,94	11,20	0,10	0,56	0,41	0,03	44,12	0,12	0,00	1,03	0,03	100,00
Spectrum 209	36,30	0,09	1,83	2,76	11,58	0,05	0,59	0,00	0,29	44,94	0,17	0,00	1,27	0,14	100,00
Spectrum 211	38,16	0,12	1,11	2,98	15,47	0,00	0,54	0,16	0,62	39,01	0,17	0,09	1,49	0,07	100,00
Spectrum 214	33,87	0,08	0,20	1,04	8,70	0,00	0,51	0,03	0,00	54,92	0,07	0,02	0,58	0,00	100,00
Spectrum 215	36,98	0,15	1,43	4,53	12,52	0,07	0,56	0,17	0,19	37,20	0,52	0,00	5,70	0,00	100,00
Spectrum 216	37,00	0,27	0,46	1,64	14,38	0,08	0,34	0,02	0,25	44,26	0,10	0,02	1,03	0,15	100,00
Spectrum 217	36,04	0,12	2,63	4,60	9,99	0,05	0,41	0,05	0,05	42,74	0,21	0,12	2,96	0,03	100,00
Spectrum 218	33,10	0,36	0,29	0,79	8,04	0,00	0,09	0,00	0,32	56,47	0,00	0,16	0,32	0,07	100,00
Spectrum 222	37,85	0,19	0,27	1,99	15,65	0,02	0,51	0,06	0,11	42,45	0,04	0,06	0,80	0,00	100,00
Spectrum 223	35,39	0,10	0,41	1,47	9,63	0,06	1,49	0,00	0,10	50,60	0,08	0,06	0,50	0,10	100,00
Spectrum 224	35,09	0,08	0,68	1,41	10,92	0,10	0,26	0,08	0,08	50,59	0,10	0,00	0,60	0,00	100,00
Spectrum 226	37,04	0,11	3,58	5,26	11,30	0,02	0,47	0,51	0,04	38,40	0,27	0,00	3,00	0,00	100,00
Spectrum 227	36,06	0,07	0,21	1,50	12,77	0,00	0,42	0,02	0,07	47,99	0,12	0,00	0,78	0,00	100,00

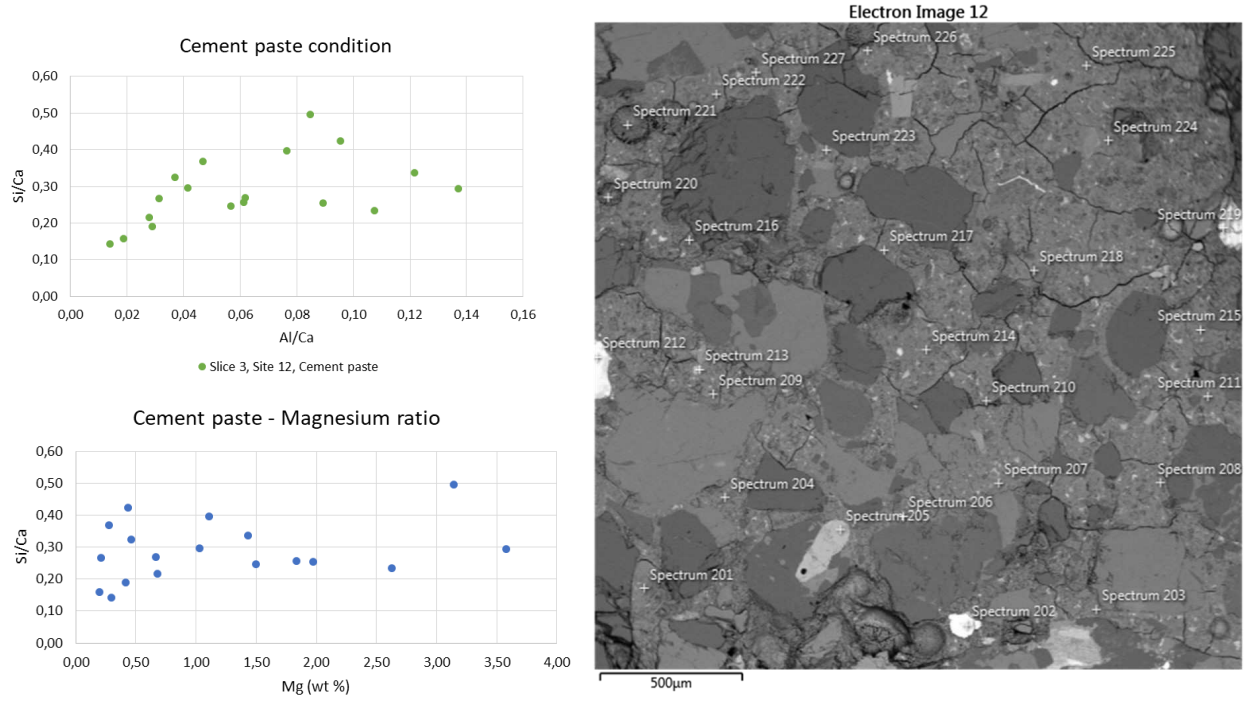

Fig. A32. Graphs and BSE image of Site 12, Slice 3.

Table A26. EDS analysis of Site 13, Slice 3.

Spectrum Label	O	Na	Mg	Al	Si	P	S	Cl	K	Ca	Ti	Cr	Fe	Zn	Total
Slice 3, Site 13, Zone 1	Cementpaste														
Spectrum 244	45,66	0,06	14,62	4,84	24,63	0,18	0,06	0,38	0,32	4,69	0,20	0,15	4,21	0,00	100,00
Spectrum 245	47,15	0,13	19,50	5,50	25,06	0,00	0,00	0,04	0,39	1,13	0,25	0,00	0,75	0,08	100,00
Spectrum 240	47,08	0,07	17,77	5,09	25,74	0,03	0,01	0,16	0,41	2,48	0,11	0,03	1,00	0,01	100,00
Spectrum 247	41,71	0,15	14,58	4,25	17,04	0,01	0,12	0,16	0,20	20,48	0,16	0,11	0,81	0,21	100,00
Spectrum 248	39,89	0,00	9,49	4,20	15,62	0,16	0,24	0,52	0,18	26,08	0,19	0,08	3,07	0,27	100,00
Spectrum 249	38,52	0,00	10,50	3,45	12,96	0,30	0,00	0,32	0,12	32,17	0,27	0,00	0,97	0,44	100,00
Spectrum 250	45,01	0,05	15,63	6,24	22,16	0,15	0,07	0,94	0,17	7,36	0,22	0,00	1,64	0,36	100,00
Spectrum 251	37,05	0,00	5,99	5,05	10,56	0,12	0,69	0,57	0,26	34,82	0,29	0,00	4,39	0,21	100,00
Spectrum 252	41,28	0,12	10,53	5,64	18,77	0,04	0,33	4,28	0,33	15,06	0,58	0,04	2,51	0,49	100,00
Spectrum 246	44,20	0,14	14,03	4,68	21,70	0,15	0,20	0,15	0,25	11,08	0,23	0,00	3,11	0,09	100,00
Slice 3, Site 13, Zone 2	Light grey in BSE-image														
Spectrum 228	30,67	0,04	5,23	2,24	8,11	0,06	0,19	0,06	0,20	1,19	0,49	0,10	51,28	0,16	100,00
Spectrum 230	35,31	0,20	7,00	2,50	14,09	0,17	0,21	0,04	0,26	2,12	0,03	0,05	38,02	0,00	100,00
Spectrum 231	27,77	0,07	1,86	0,83	6,10	0,06	0,11	0,05	0,23	1,92	0,77	0,08	60,10	0,05	100,00
Spectrum 232	31,17	0,00	5,23	1,70	9,66	0,04	0,12	0,05	0,14	0,99	0,00	0,09	50,77	0,05	100,00
Spectrum 233	27,78	0,07	2,36	1,29	6,03	0,07	0,12	0,04	0,13	0,70	0,09	0,01	61,31	0,00	100,00
Spectrum 236	30,51	0,00	4,98	1,58	8,79	0,09	0,08	0,02	0,07	0,93	0,07	0,06	52,81	0,00	100,00
Spectrum 239	34,39	0,01	6,52	1,82	13,83	0,01	0,01	0,14	0,12	2,22	0,12	0,07	40,73	0,01	100,00
Spectrum 241	34,67	0,16	7,41	2,04	13,68	0,03	0,04	0,09	0,09	2,50	0,00	0,08	39,20	0,00	100,00
Spectrum 242	32,35	0,05	3,19	2,94	8,10	0,06	0,32	0,01	0,19	22,18	0,38	0,15	30,08	0,00	100,00
Spectrum 243	35,26	0,04	4,60	3,07	12,85	0,12	0,11	0,05	0,41	17,05	0,14	0,15	26,02	0,15	100,00
Slice 3, Site 13, Zone 3	White in BSE-image														
Spectrum 234	25,28	0,08	1,00	0,72	3,29	0,03	0,09	0,02	0,00	0,54	0,18	0,06	68,67	0,05	100,00
Spectrum 235	25,29	0,06	1,08	0,77	3,24	0,02	0,05	0,00	0,05	0,68	0,26	0,02	68,47	0,01	100,00
Spectrum 238	25,02	0,00	0,66	1,29	2,69	0,00	0,14	0,00	0,05	0,52	0,23	0,00	69,37	0,03	100,00

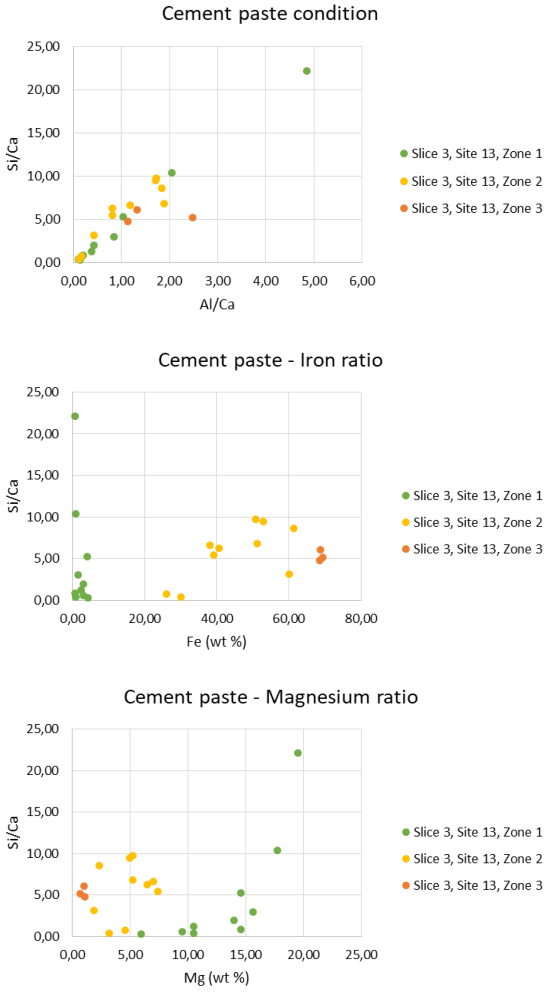

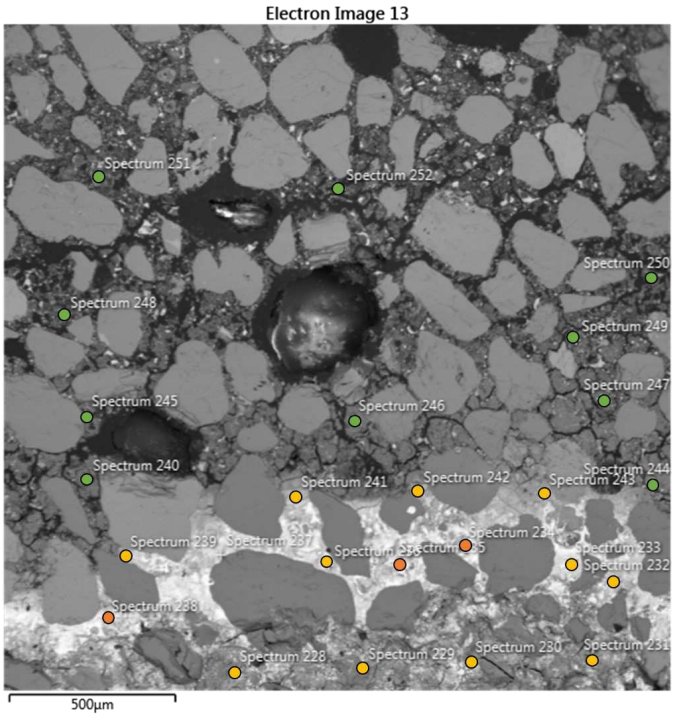

Fig. A33. Graphs and BSE image of Site 13, Slice 3.

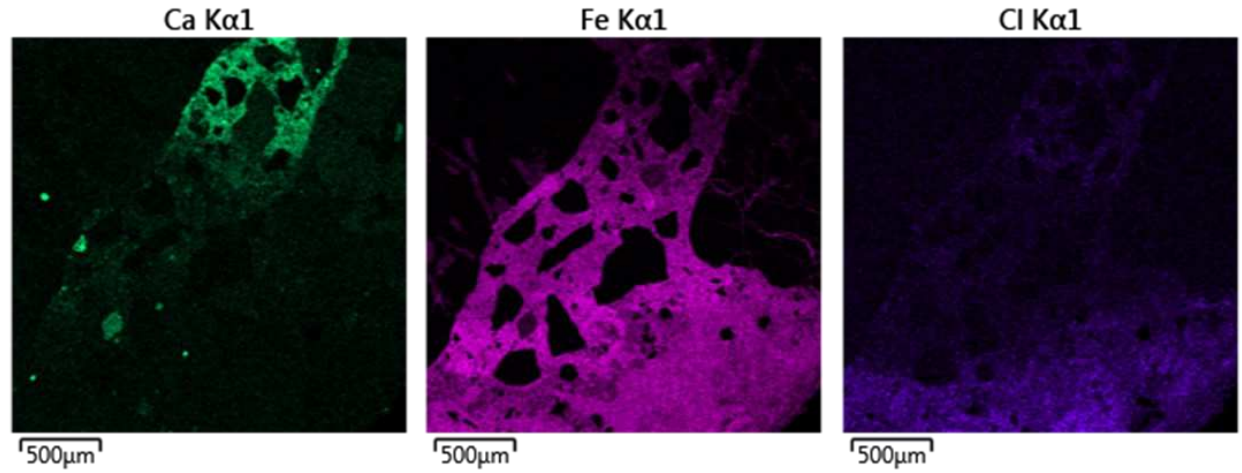

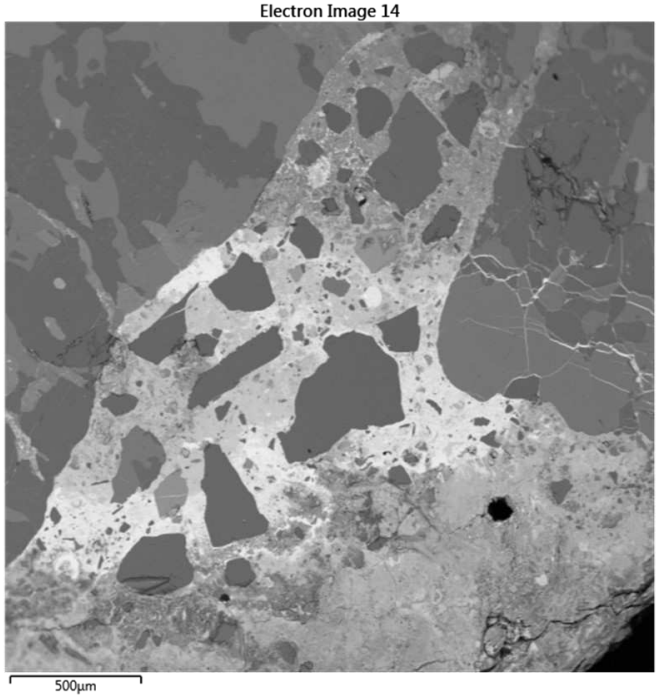

Fig. A34. Element maps and BSE image of Site 14, Slice 3.

Table A27. EDS analysis of Site 16, Slice 3.

Spectrum Label	O	Na	Mg	Al	Si	P	S	Cl	K	Ca	Ti	Cr	Fe	Zn	Total
Slice 3, Site 16, Zone 1	Medium grey cementpaste														
Spectrum 264	42,07	0,02	0,80	3,22	22,88	0,15	0,29	0,27	0,00	29,52	0,01	0,00	0,44	0,33	100,00
Spectrum 263	40,87	0,17	1,14	3,38	19,77	0,08	0,76	0,27	0,08	32,52	0,12	0,02	0,82	0,00	100,00
Spectrum 254	42,12	0,13	3,31	3,79	21,90	0,11	0,25	0,16	0,15	26,64	0,12	0,00	1,23	0,10	100,00
Spectrum 255	40,08	0,05	0,55	3,33	18,38	0,01	0,91	0,09	0,12	35,00	0,02	0,05	1,42	0,00	100,00
Spectrum 256	38,13	0,03	0,87	2,58	14,75	0,09	1,01	0,17	0,04	41,49	0,03	0,00	0,75	0,07	100,00
Spectrum 258	41,42	0,03	5,46	3,79	19,84	0,11	0,32	0,11	0,09	26,11	0,07	0,00	2,54	0,11	100,00
Spectrum 259	41,90	0,29	0,48	4,55	21,36	0,09	0,83	0,17	0,42	26,93	0,13	0,06	2,78	0,00	100,00
Slice 3, Site 16, Zone 2	Light grey in BSE-image														
Spectrum 253	28,72	0,05	0,14	0,07	0,02	0,00	0,16	0,01	0,12	70,48	0,13	0,05	0,02	0,03	100,00
Spectrum 257	28,67	0,20	0,14	0,00	0,08	0,01	0,20	0,02	0,00	70,55	0,00	0,00	0,15	0,00	100,00
Spectrum 262	28,70	0,18	0,19	0,07	0,05	0,09	0,15	0,00	0,00	70,53	0,00	0,00	0,02	0,00	100,00
Spectrum 269	28,65	0,04	0,69	0,08	0,11	0,00	0,07	0,00	0,08	69,93	0,00	0,04	0,21	0,10	100,00
Spectrum 270	28,82	0,10	0,18	0,07	0,14	0,03	0,21	0,08	0,00	70,06	0,06	0,09	0,15	0,00	100,00
Spectrum 271	28,67	0,00	0,18	0,05	0,06	0,00	0,24	0,00	0,01	70,61	0,00	0,00	0,00	0,19	100,00
Spectrum 279	28,75	0,06	0,12	0,12	0,36	0,07	0,14	0,14	0,02	69,09	0,00	0,00	1,14	0,00	100,00
Slice 3, Site 16, Zone 3	Light grey cement paste														
Spectrum 261	33,95	0,08	0,68	1,35	8,74	0,00	0,47	0,07	0,06	54,05	0,00	0,00	0,55	0,00	100,00
Spectrum 265	33,85	0,00	2,98	11,83	2,84	0,00	0,05	0,00	0,06	32,84	1,28	0,05	13,99	0,24	100,00
Spectrum 272	30,74	0,14	0,63	0,87	3,20	0,00	0,27	0,09	0,07	63,39	0,00	0,07	0,51	0,01	100,00
Spectrum 273	36,54	0,14	1,01	2,33	12,37	0,05	0,78	0,03	0,19	44,30	0,08	0,13	1,97	0,08	100,00
Spectrum 274	37,19	0,04	1,46	2,79	12,91	0,07	0,80	0,00	0,12	42,40	0,44	0,01	1,76	0,00	100,00
Spectrum 275	36,57	0,18	1,42	3,06	11,92	0,06	0,78	0,07	0,60	43,35	0,06	0,10	1,78	0,05	100,00
Spectrum 280	34,43	0,22	0,81	2,27	8,37	0,00	0,84	0,02	0,22	51,97	0,00	0,00	0,82	0,02	100,00

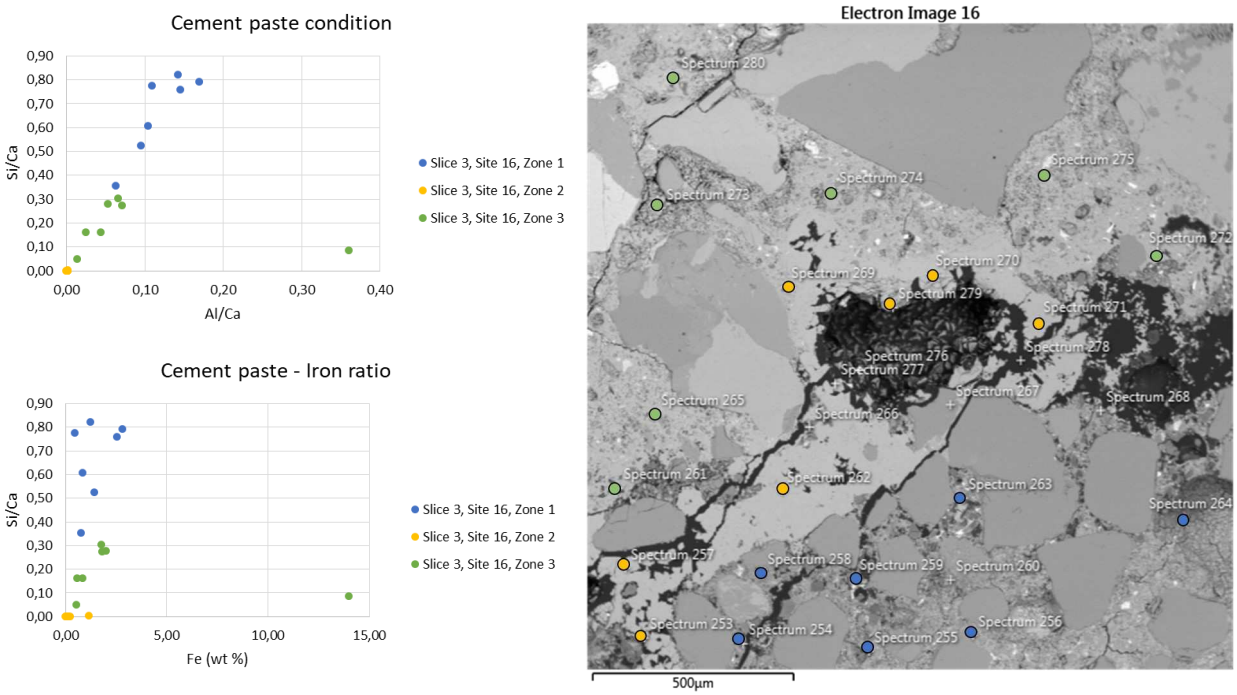

Fig. A35. Graphs and BSE image of Site 16, Slice 3.

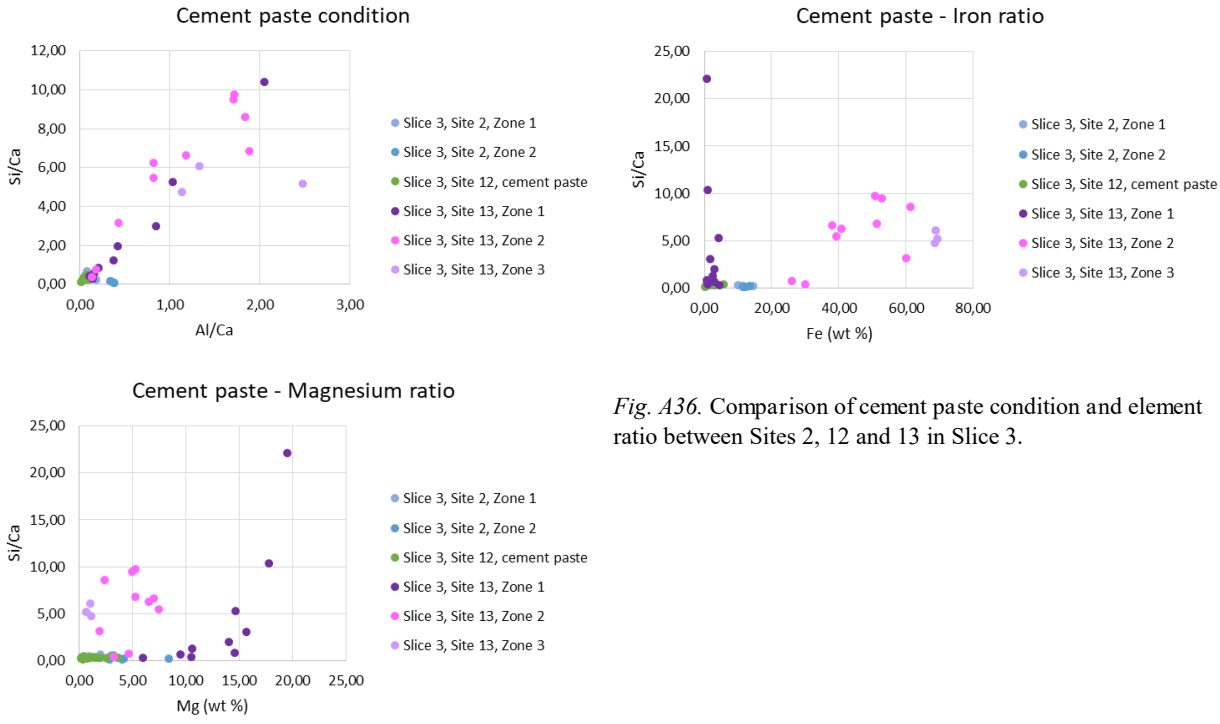

Fig. A36. Comparison of cement paste condition and element ratio between Sites 2, 12 and 13 in Slice 3.

Tidigare skrifter i serien ”Examensarbeten i Geologi vid Lunds universitet”:

498. Bergcrantz, Jacob, 2017: Ett fönster till Kattegatts förflutna genom analys av bottenlevande foraminiferer. (15 hp)
499. O'Hare, Paschal, 2017: Multiradionuclide evidence for an extreme solar proton event around 2610 BP. (45 hp)
500. Goodship, Alastair, 2017: Dynamics of a retreating ice sheet: A LiDAR study in Värmland, SW Sweden. (45 hp)
501. Lindvall, Alma, 2017: Hur snabbt påverkas och nollställs luminiscenssignaler under naturliga ljusförhållanden? (15 hp)
502. Sköld, Carl, 2017: Analys av stabila isotoper med beräkning av blandningsförhållande i ett grundvattenmagasin i Älvkarleby-Skutskär. (15 hp)
503. Sällström, Oskar, 2017: Tolkning av geofysiska mätningar i hammarborrhål på södra Gotland. (15 hp)
504. Ahrenstedt, Viktor, 2017: Depositional history of the Neoproterozoic Visingsö Group, south-central Sweden. (15 hp)
505. Schou, Dagmar Juul, 2017: Geometry and faulting history of the Long Spur fault zone, Castle Hill Basin, New Zealand. (15 hp)
506. Andersson, Setina, 2017: Skalbärande marina organismer och petrografi av tidigcampanska sediment i Kristianstadsbassängen – implikationer på paleomiljö. (15 hp)
507. Kempengren, Henrik, 2017: Föroreningsspridning från kustnära deponi: Applicering av Landsim 2.5 för modellering av lakvattentransport till Östersjön. (15 hp)
508. Ekborg, Charlotte, 2017: En studie på samband mellan jordmekaniska egenskaper och hydrodynamiska processer när erosion påverkar släntstabiliteten vid ökad nederbörd. (15 hp)
509. Silvén, Björn, 2017: LiDARstudie av glaciala landformer sydväst om Söderåsen, Skåne, Sverige. (15 hp)
510. Rönning, Lydia, 2017: Ceratopsida dinosauriers migrationsmönster under krittiden baserat på paleobiogeografi och fylogeni. (15 hp)
511. Engleson, Kristina, 2017: Miljökonsekvensbeskrivning Revinge brunnsfält. (15 hp)
512. Ingered, Mimmi, 2017: U-Pb datering av zirkon från migmatitisk gnejs i Delsjöområdet, Idefjordenterrängen. (15 hp)
513. Kervall, Hanna, 2017: EGS - framtidens geotermiska system. (15 hp)
514. Walheim, Karin, 2017: Kvartsmineralogins betydelse för en lyckad luminiscensdatering. (15 hp)
515. Aldenius, Erik, 2017: Lunds Geotermisystem, en utvärdering av 30 års drift. (15 hp)
516. Aulin, Linda, 2017: Constraining the duration of eruptions of the Rangitoto volcano, New Zealand, using paleomagnetism. (15 hp)
517. Hydén, Christina Engberg, 2017: Drumlinerna i Löberöd - Spår efter flera isrörelseriktningar i mellersta Skåne. (15 hp)
518. Svantesson, Fredrik, 2017: Metodik för kartläggning och klassificering av erosion och släntstabilitet i vattendrag. (45 hp)
519. Stjern, Rebecka, 2017: Hur påverkas luminiscenssignaler från kvarts under laboratorieförhållanden? (15 hp)
520. Karlstedt, Filippa, 2017: P-T estimation of the metamorphism of gabbro to garnet amphibolite at Herrestad, Eastern Segment of the Sveconorwegian orogen. (45 hp)
521. Önnervik, Oscar, 2017: Ooider som naturliga arkiv för förändringar i havens geokemi och jordens klimat. (15 hp)
522. Nilsson, Hanna, 2017: Kartläggning av sand och naturgrus med hjälp av resistivitetsmätning på Själland, Danmark. (15 hp)
523. Christensson, Lisa, 2017: Geofysisk undersökning av grundvattenskydd för planerad reservvattentäkt i Mjölkalånga, Hässleholms kommun. (15 hp)
524. Stamsnijder, Joaen, 2017: New geochronological constraints on the Klipriviersberg Group: defining a new Neoarchean large igneous province on the Kaapvaal Craton, South Africa. (45 hp)
525. Becker Jensen, Amanda, 2017: Den eocena Furformationen i Danmark: exceptionella bevaringstillstånd har bidragit till att djurs mjukdelar fossiliserats.(15 hp)
526. Radomski, Jan, 2018: Carbonate sedimentology and carbon isotope stratigraphy of the Tallbacken-1 core, early Wenlock Slite Group, Gotland, Sweden. (45 hp)
527. Pettersson, Johan, 2018: Ultrastructure and biomolecular composition of sea turtle epidermal remains from the Campanian (Upper Cretaceous) North Sulphur River of Texas. (45 hp)
528. Jansson, Robin, 2018: Multidisciplinary perspective on a natural attenuation zone in a PCE contaminated aquifer. (45 hp)
529. Larsson, Alfred, 2018: Rb-Sr sphalerite data and implications for the source and timing of Pb-Zn deposits at the Caledonian margin in Sweden. (45 hp)
530. Balija, Fisnik, 2018: Stratigraphy and pyrite geochemistry of the Lower–Upper Ordovician in the Lerhamn and Fågelsång

-3 drill cores, Scania, Sweden. (45 hp)

531. Höglund, Nikolas, 2018: Groundwater chemistry evaluation and a GIS-based approach for determining groundwater potential in Mörbylånga, Sweden. (45 hp)
532. Haag, Vendela, 2018: Studie av mikrostrukturer i karbonatslagkäglor från nedslagsstrukturen Charlevoix, Kanada. (15 hp)
533. Hebrard, Benoit, 2018: Antropocen – vad, när och hur? (15 hp)
534. Jancsak, Nathalie, 2018: Åtgärder mot kusterosion i Skåne, samt en fallstudie av erosionsskydden i Löderup, Ystad kommun. (15 hp)
535. Zachén, Gabriel, 2018: Mesosideriter – redogörelse av bildningsprocesser samt SEM-analys av Vaca Muertameteoriten. (15 hp)
536. Fägersten, Andreas, 2018: Lateral variability in the quantification of calcareous nannofossils in the Upper Triassic, Austria. (15 hp)
537. Hjertman, Anna, 2018: Förutsättningar för djupinfiltration av ytvatten från Ivösjön till Kristianstadbassängen. (15 hp)
538. Lagerstam, Clarence, 2018: Varför svalde svanödlor (Reptilia, Plesiosauria) stenar? (15 hp)
539. Pilser, Hannes, 2018: Mg/Ca i bottenlevande foraminiferer, särskilt med avseende på temperaturer nära 0°C. (15 hp)
540. Christiansen, Emma, 2018: Mikroplast på och i havsbotten - Utbredningen av mikroplaster i marina bottensediment och dess påverkan på marina miljöer. (15 hp)
541. Staahlnacke, Simon, 2018: En sammanställning av norra Skånes prekambriska berggrund. (15 hp)
542. Martell, Josefin, 2018: Shock metamorphic features in zircon grains from the Mien impact structure - clues to conditions during impact. (45 hp)
543. Chitindingu, Tawonga, 2018: Petrological characterization of the Cambrian sandstone reservoirs in the Baltic Basin, Sweden. (45 hp)
544. Chonewicz, Julia, 2018: Dimensionerande vattenförbrukning av grundvatten samt alternativa vattenkvaliteter. (15 hp)
545. Adeen, Lina, 2018: Hur lämpliga är de geofysiska metoderna resistivitet och IP för kartläggning av PFOS? (15 hp)
546. Nilsson Brunlid, Anette, 2018: Impact of southern Baltic sea-level changes on landscape development in the Verkeån River valley at Haväng, southern Sweden, during the early and mid Holocene. (45 hp)
547. Perälä, Jesper, 2018: Dynamic Recrystallization in the Sveconorwegian Frontal Wedge, Småland, southern Sweden. (45 hp)
548. Artursson, Christopher, 2018: Stratigraphy, sedimentology and geophysical assessment of the early Silurian Halla and Klinteberg formations, Altajme core, Gotland, Sweden. (45 hp)
549. Kempengren, Henrik, 2018: Att välja den mest hållbara efterbehandlingsmetoden vid sanering: Applicering av beslutsstödsverktyget SAMLA. (45 hp)
550. Andreasson, Dagnija, 2018: Assessment of using liquidity index for the approximation of undrained shear strength of clay tills in Scania. (45 hp)
551. Ahrenstedt, Viktor, 2018: The Neoproterozoic Visingsö Group of southern Sweden: Lithology, sequence stratigraphy and provenance of the Middle Formation. (45 hp)
552. Berglund, Marie, 2018: Basaltkuppen - ett spel om mineralogi och petrologi. (15 hp)
553. Hernnäs, Tove, 2018: Garnet amphibolite in the internal Eastern Segment, Sveconorwegian Province: monitors of metamorphic recrystallization at high temperature and pressure during Sveconorwegian orogeny. (45 hp)
554. Halling, Jenny, 2019: Characterization of black rust in reinforced concrete structures: analyses of field samples from southern Sweden. (45 hp)

LUNDS UNIVERSITET

Geologiska institutionen
Lunds universitet
Sölvegatan 12, 223 62 Lund